

A Scalable Thermal Reservoir Simulator for Giant Models on Parallel Computers

Hui Liu*, Zhangxin Chen

Dept. of Chemical and Petroleum Engineering, University of Calgary
2500 University Drive NW, Calgary, AB, Canada

Abstract

This paper introduces the model, numerical methods, algorithms and parallel implementation of a thermal reservoir simulator that designed for numerical simulations of thermal reservoir with multiple components in three dimensional domain using distributed-memory parallel computers. Its full mathematical model is introduced with correlations for important properties and well modeling. Various well constraints, such as fixed bottom hole pressure, fixed oil, water, gas and liquid rates, constant heat transfer model, convective heat transfer model, heater model (temperature control, rate control, dual rate/temperature control), and subcool (steam trap), are introduced in details, including their mathematical models and methods. Efficient numerical methods and parallel computing technologies are presented. The simulator is designed for giant models with billions or even trillions of grid blocks using hundreds of thousands of CPUs. Numerical experiments show that our results match commercial simulators, which confirms the correctness of our methods and implementations. SAGD simulation with 15106 well pairs is also presented to study the effectiveness of our numerical methods. Scalability testings demonstrate that our simulator can handle giant models with over 200 billion grid blocks using 98,000 CPU cores and the simulator has good scalability.

1 Introduction

Reservoir simulations play critical roles in reservoir management, since it provides one way to examine production plan and to predict future oil and gas production[57]. Simulators have been developed and applied for decades, such as CMG STARS. They have widely used in reservoir management. When multiple chemicals are considered in a model or the geological model is complicated, it may take too long for one simulation, which reduces the productivity of reservoir engineers. Acceleration of simulations is important to oil and gas industry.

Reservoir simulations have been studied for decades, and various models and methods have been proposed. Crookston et al.[11] proposed a simple two-dimensional model to deal with three phases flow and to handle vaporization-condensation effects. Grabowski [18] developed a sequential implicit method for thermal reservoir model. A general four-phase multi-component in-situ combustion model was proposed by Coats [8], which was improved by Rubin [26] that a fully coupled implicit wellbore model was considered. Variable substitution [8] methods and pseudo-equilibrium ratio (PER) methods [11] were designed to discretize the thermal models, while Miffin et al[24] suggested to use global variables, pressure, moles and energy as unknowns. Barua [5] proposed algorithms to solve the nonlinear equations in parallel and combined the iterative solutions to linear systems and Quasi-Newton method. Effective linear solver and preconditioner methods have been proposed to accelerate the solution of linear systems from reservoir simulations, such as constrained pressure residual (CPR) methods [28, 6], multi-stage methods [3], multiple level preconditioners [29] and FASP (fast auxiliary space preconditioners) [19, 16]. Chen et al. designed a family of CPR-type preconditioners, such as CPR-FP, CPR-FPF and CPR-FFPF methods [21], which have been applied to different simulations [32, 22, 33].

Parallel computers have more memory and higher performance, which provide excellent approaches to accelerate reservoir simulations [12, 10, 36, 15]. In the early stage, vectorization techniques in shared-memory machines was widely applied though it didn't scale very well [9, 12]. Meijerink [23] developed a black oil simulator using the IMPES method and implemented on a local-memory MIMD computer. Chien [7] applied domain decomposition and MPI on an IBM SP-2 parallel computer. Wang

*Authors to whom correspondence may be addressed. Email: hui.sc.liu@gmail.com

[35, 25] implemented a fully implicit equation-of-state compositional simulator for distributed-memory parallel computers, and large-scale reservoir models were simulated [34]. Reservoir models with millions of grid blocks on parallel computers were reported [27]. Killough [20] reviewed the parallel reservoir models and parallel computing technologies. Saudi Aramco developed new-generation massively-parallel reservoir simulator [4, 13, 14, 17], and reservoir models with millions of grid blocks were studied. Zhang et al. developed a scalable general-purpose platform, which has been applied to reservoir simulations [37, 38, 30].

This paper introduces our work on developing a parallel thermal simulator, including mathematical model, numerical methods and implementation. The model is introduced in details, and explanations are provided, which compared with CMG STARS, such as modeling method and its default behaviors. Here are the features of our methods and simulator:

1. An automatic configure script has been developed to detect operating system and compiler options. With its help, the simulator can be compiled under any Unix-like systems, Linux systems and Mac OS, and any MPI implementations, such as IBM Spectrum MPI, Intel MPI, MPICH, OpenMPI, and MVAPICH. The codes are written by C language from scratch, and at this moment, around 60,000 lines of C code have been written.
2. The simulator is designed to work with arbitrary CPU cores (MPI processes), such 1,000,000 cores.
3. All data types are customized. The integer can be configured as integer (`int`), long integer (`long int`) and long long integer (`long long int`). The floating point number could be double precision (`double`) and long double (`long double`). MPI support is required to handle long double.
4. The simulator can handle arbitrary grid size, arbitrary oil components (heavy oil and light oil), arbitrary gas components (non-condensable gas) and arbitrary wells (injector, producer, and heating wells). Only parallel computing resource and MPI compilers can limit the capacity of the simulator. The simulator has tested models with hundreds of billions of grid blocks, hundreds of oil and gas components, and tens of thousands of wells.
5. A flexible keyword parsing model has been developed to handle user input. All properties, such as rock, water, oil and gas, heat and well, are handled by the keyword parsing module. Arbitrary oil and gas components, wells and schedules can be read and parsed.
6. The K-value method is applied. The gas phase can be treated as ideal gas or non-ideal gas, which is controlled by keyword file. If it is non-ideal gas, the RK EOS is employed to handle it.
7. Effective discretization schemes, multi-stage CPR-type preconditioners, decoupling methods and Newton methods have been developed.
8. Techniques for accelerating Newton methods, such as damping, Appleyard method, modified Appleyard method and weighted upstream [65], have been developed in the simulator.
9. Various well controls have been implemented, such as fixed bottom hole pressure, fixed water rate, fixed oil rate, fixed gas rate, fixed liquid rate, constant heat transfer model, convective heat transfer model, heating well (`HTWELL` in CMG STARS), subcool (steamtrap, rate control, temperature control, dual rate/temperature control), and combinations of these controls. Their mathematical details are provided.
10. The well index has several models, which are the same as CMG STARS, including user input and a few analytical models. Different well weights, such as unweighted, explicit weight and implicit weight for injector, explicit weight and implicit weight for producer, have been developed.
11. Isenthalpic flash calculations and surface flash calculations are implemented to model injection, production and performance report.
12. Various enthalpy calculation formula have been studied, including gas enthalpy, liquid enthalpy, and vaporization enthalpy.
13. Analytical formulas and table-based input for relative permeability and viscosity. For table input data, we have linear interpolation and cubic monotone interpolation.
14. Various mixing rules have been developed for conduct (simple and complex), viscosity, and density. Different rock modeling, such as bulk constant and rock constant, are implemented as CMG STARS.

The structure of the paper is as follows. In §2, the thermal reservoir model is introduced and the equations for various properties are presented. In §3, numerical methods and parallel computing approaches are proposed. In §4, numerical experiments are carried out to validate our results against commercial simulator, CMG STARS, and to show the scalability of the parallel thermal simulator.

2 Mathematical Model

Most simulators share the same theory framework [40, 66, 67]. For the sake of completeness, the mathematical model of the thermal simulator is introduced here, and the models are almost the same as reference [40, 66, 67]. The content of this section is borrowed from our previous manuscript [1] and CMG STARS [40]. In reference [1], the following assumptions were made: water component exists in water and gas phases, all oil components exist in oil and gas phases, non-condensable gas components exist in gas phase only, and all three phases co-exist during the entire simulation. In this paper, different assumptions are made: the water component exists in water and gas phases, heavy oil components exist in oil phase only, light oil components exist in both oil and gas phases, non-condensable gas components exist in gas phase. Phase appearance and dis-appearance are allowed. Depending on the input, arbitrary oil components and non-condensable gas components are allowed. Necessary changes have been made to address the difference between the in-situ combustion model [1] and the thermal model applied here.

2.1 Darcys Law

Darcy's law is applied to model the velocity of a fluid phase, which describes the relation among permeability, viscosity, saturation and pressure difference. In our thermal model, the water phase (w), the oil phase (o) and the gas phase (g) co-exist ([39]),

$$\begin{aligned}\vec{u}_w &= -\frac{k_{rw}}{\mu_w} \vec{k} (\nabla p_w - \gamma_w \nabla z) \\ \vec{u}_o &= -\frac{k_{ro}}{\mu_o} \vec{k} (\nabla p_o - \gamma_o \nabla z) \\ \vec{u}_g &= -\frac{k_{rg}}{\mu_g} \vec{k} (\nabla p_g - \gamma_g \nabla z).\end{aligned}\tag{1}$$

2.2 Mass Conservation Equations

For a multi-phase, multi-component system, $x_{c,\alpha}$ denotes the mole fraction of a component in the α -phase. The molar number of a component in a phase and the total molar number of the phase are denoted as $n_{c,\alpha}$ and n_α , respectively. Thus the molar fractions are

$$x_{c,\alpha} = \frac{n_{c,\alpha}}{n_\alpha}.\tag{2}$$

In the simplest thermal model, water phase has water component only, so $n_w = 1$. If the gas phase exists, it may contains water, light oil and non-condensable gas components. Since each component may exist in several phases, total molar number of component c is written as below ([39]):

$$\frac{\partial}{\partial t} (\phi \sum_\alpha^{N_\alpha} \rho_\alpha S_\alpha x_{c,\alpha}) = -\nabla \cdot (\sum_\alpha^{N_\alpha} \rho_\alpha S_\alpha \vec{u}_\alpha) + \sum_\alpha^{N_\alpha} q_{\alpha,well} x_{c,\alpha}.\tag{3}$$

In this equation, it is noticeable that different from other models, the mass conserved here is only the molar number rather than the mass. Also, ρ_α and q_α are the molar density and molar production/injection of phase α .

2.3 Energy Conservation Equation

The energy conservation equation for a thermal process ([39]) is described as:

$$\begin{aligned} & \frac{\partial}{\partial t} (\phi(\rho_w S_w U_w + \rho_o S_o U_o + \rho_g S_g U_g) + (1 - \phi)U_r) \\ = & \nabla \cdot (K_T \nabla T) - \nabla \cdot (\rho_w H_w \vec{u}_w + \rho_o H_o \vec{u}_o + \rho_g H_g \vec{u}_g) \\ & + (q_{w,well} H_w + q_{o,well} H_o + q_{g,well} H_g) - Q_{loss}, \end{aligned} \quad (4)$$

where U denotes the volumetric internal energy. On the right-hand side, the first term represents the conduction term. This is caused by a difference in temperature, where the rate of conduction is constraint by K_T , the bulk thermal conductivity. The thermal conductivity here is a combination of liquid, and rock, where a linear mixing rule is applied ([40]),

$$K_T = \phi [S_w K_w + S_o K_o + S_g K_g] + (1 - \phi)K_r. \quad (5)$$

In the equation, K_w, K_o, K_g, K_r denote thermal conductivities for water phase, oil phase, gas phase, and rock separately. This rule is also called simple mixing rule in CMG STARS. The complex mixing rule is also implemented in the simulator, whose details can be read from CMG STARS manual. We should mention that there are different ways to model rock internal energy: $(1 - \phi)U_r$. In above equation, the porosity, ϕ , is a function of pressure and temperature, and U_r is a function of temperature, so the rock internal energy is a function of pressure and temperature. This method assumes the volume of a grid block does not change. Another way is to assume the rock volume does not change, which uses $(1 - \phi_i)U_r$ to model rock internal energy. ϕ_i does not change during the simulation, and this method preserves the rock energy. The second method is applied as the default method in CMG STARS and our simulator.

A heat loss term to underburden and overburden is also considered, and the semi-analytical method developed by Vinsome et al. [59] is applied.

2.4 Capillary Pressure

A capillary pressure P_c is the pressure difference across the interface between two immiscible fluids arising from capillary forces, which are usually functions of saturation, relationship ([39]):

$$p_w = p_o - p_{cow}(S_w), \quad p_g = p_o + p_{cog}(S_g). \quad (6)$$

2.5 Phase Saturation Constraint

The solid phase is not considered. The water, oil and gas saturations have the following constraint,

$$S_w + S_o + S_g = 1. \quad (7)$$

The gas phase can appear and disappear. The PER (Pseudo-Equilibrium Ratios) method is applied to calculate K-values of water component and light oil components such that water phase and oil phase do not disappear. However, the water saturation and oil saturation should be handled carefully when they are too small and the gas phase exists. The partial derivatives of K-values to saturations must be included when the saturations are small.

2.6 Phase Composition Constraints

A constraint implies that the sum of all the components' mole fractions in a phase adds up to one, which is usually encountered for in compositional flow ([39]):

$$\sum_{\alpha}^{N_{\alpha}} x_{c,\alpha} = 1, \quad \alpha = w, o, g. \quad (8)$$

It comes from the total mole number of a given phase that

$$\sum_{\alpha}^{N_{\alpha}} n_{c,\alpha} = n_{\alpha}, \quad \alpha = w, o, g. \quad (9)$$

2.7 Phase Equilibrium Constraints

In a multi-component system, a K value (or an equilibrium ratio) is defined as the ratio of the mole fractions of a component in its distributed two phases:

$$K_{c,\alpha_1,\alpha_2} = \frac{x_{c,\alpha_1}}{x_{c,\alpha_2}}. \quad (10)$$

In our model, a K value is a function of pressure and temperature, which is calculated from an analytic equation as:

$$K = \left(\frac{kv_1}{p} + kv_2p + kv_3 \right) \exp \left(\frac{kv_4}{T - kv_5} \right). \quad (11)$$

When gas phase exists, calculations of K-values for water, light oil and heavy oil are as follows ([39]; [40]):

$$\begin{aligned} K_W &= K_W(p, T) \\ &= \left(\frac{kv_{1W}}{p} + kv_{2W} \cdot p + kv_{3W} \right) \exp \left(\frac{kv_{4W}}{T - kv_{5W}} \right), \\ K_{O,i} &= K_O[i](p, T) \\ &= \left(\frac{kv_{1O,i}}{p} + kv_{2O,i} \cdot p + kv_{3O,i} \right) \exp \left(\frac{kv_{4O,i}}{T - kv_{5O,i}} \right). \\ K_{O,i} &= K_O[i](p, T) = 0. \end{aligned} \quad (12)$$

In our thermal model, the calculations of K-values are modified, where the PER (Pseudo-Equilibrium Ratios) method([51, 50]) is applied for water and light oil,

$$K^*_{W} = K^*_W(p, T) = \left(\frac{S_w}{S_w + n_{cg}} \right) K_W(p, T), \quad (13)$$

$$K^*_{O,i} = K^*_{O,i}(p, T) = \left(\frac{S_o}{S_o + \epsilon} \right) K_O[i](p, T). \quad (14)$$

In calculations of pseudo K-values, ϵ is a small number of the order of $1e - 4$. The water phase and oil phase exist through the entrie simulation. However, the gas phase is allowed to disappear. The gas phase molar fraction for the oil components and water component are functions of p, T, S_w, S_g . The molar fraction in the gas phase for gas components are the basic unknowns:

$$y = y(p, T, S_w, S_g). \quad (15)$$

2.8 Compressibility Factor of Real Gas

In the thermal model, the Redlich-Kwong EOS ([48]) is used to calculate the Z factor.

$$A = A(p, T) = 0.427480 \left(\frac{p}{p_{crit}} \right) \left(\frac{T_{crit}}{T} \right)^{2.5}, \quad (16)$$

$$B = B(p, T) = 0.086640 \left(\frac{p}{p_{crit}} \right) \left(\frac{T_{crit}}{T} \right). \quad (17)$$

IN addition, the following mixing method is applied:

$$a = \sum_i y_i T_{crit,i} \sqrt{\frac{T_{crit,i}}{p_{crit,i}}}, \quad (18)$$

$$b = \sum_i y_i \frac{T_{crit,i}}{p_{crit,i}}, \quad (19)$$

$$T_{crit} = \left(\frac{a^2}{b}\right)^{\frac{2}{3}}, \quad (20)$$

$$p_{crit} = \frac{T_{crit}}{b}. \quad (21)$$

Then, after we have the coefficients A and B, the compressibility factor of real gas satisfies the equation

$$Z^3 - Z^2 + (A - B - B^2)Z - AB = 0. \quad (22)$$

This equation is cubic. Therefore, there are three roots for the equation. Also, a root might be virtual. In this case, we choose the biggest real root. With the calculation of all the coefficients, the Z factor is a function of p , T , x_i and y_i :

$$Z = Z(p, T, x_i, y_i). \quad (23)$$

2.9 Density

For real gas mixture, the density of the gas phase can be calculated as:

$$\rho_g = \rho_g(p, T, x_i, y_i) = \frac{p}{Z(p, T, x_i, y_i) \cdot R \cdot T}$$

The water phase only contains one water component in this model, so the calculation of the water density is simple:

$$\rho_w = \rho_w(p, T) = \rho_{w,ref} \exp(cp_w(p - p_{ref}) - ct1_w(T - T_{ref})) \quad (24)$$

$$- \frac{ct2_w}{2}(T - T_{ref})^2 + cpt_w(p - p_{ref})(T - T_{ref})) \quad (25)$$

where $\rho_{w,ref}$ is the reference density of the water phase at the reference temperature and pressure.

For oil component $O[i]$ is in the oil phase, the density can be calculated the same:

$$\rho_{O[i]} = \rho_{O[i]}(p, T) = \rho_{O[i],ref} \exp(cp_{O[i]}(p - p_{ref}) - ct1_{O[i]}(T - T_{ref})) \quad (26)$$

$$- \frac{ct2_{O[i]}}{2}(T - T_{ref})^2 + cpt_{O[i]}(p - p_{ref})(T - T_{ref})) \quad (27)$$

The density of oil phase, ρ_o , which is mixture of multiple oil components, is calculated as:

$$\frac{1}{\rho_o} = \sum_i^{n_{co}} \frac{x_i}{\rho_{O[i]}}. \quad (28)$$

2.10 Viscosity

The viscosity of heavy oil is very high, and we assume the viscosity of an oil component is a function of temperature,

$$\mu_{O[i]} = avisc_{O[i]} \exp\left(\frac{bvisc_{O[i]}}{T}\right). \quad (29)$$

The oil phase viscosity is calculated by a logarithmic mixing rule:

$$\ln(\mu_o) = \sum_i^{n_{co}} x[i] \ln(\mu_{O[i]}(T)), \quad (30)$$

which is equivalent to,

$$\mu_o = \mu_o(T, x_i) = \exp\left(\sum_i^{n_{co}} x[i] \ln(\mu_{O[i]}(T))\right) = \sum_i^{n_{co}} (\mu_{O[i]}(T))^{x_i}. \quad (31)$$

The water phase has only one component, and its viscosity is calculated as:

$$\mu_w = \mu_w(T) = avisc_w \exp\left(\frac{bvisc_w}{T}\right). \quad (32)$$

The gas component viscosity is calculated as,

$$\mu_{g,i} = \mu_{g,i}(T) = avg_i \cdot T^{bvg_i}. \quad (33)$$

According to a mixing rule, the molar mass of a component is included:

$$\mu_g = \mu_g(p, T, S_w, S_g, x_i, y_i) = \frac{\sum_i \mu_{g,i} \cdot y_i \sqrt{M_i}}{\sum_i y_i \sqrt{M_i}}. \quad (34)$$

2.11 Porosity

Porosity is the ratio of the pore volume to the bulk volume in a porous medium, describing the volume containing fluids. When pressure is high, due to the effort of fluids, pores are also enlarged. For a non-isothermal model, the porosity is also influenced by temperature. We define a coefficient as a total compressibility of porosity ([39]):

$$\phi_c = \phi_c(p, T) = cpor(p - p_{ref}) - ctpor(T - T_{ref}) + cptpor(p - p_{ref})(T - T_{ref}). \quad (35)$$

This factor is a function of pressure and temperature. For the calculation of porosity, we have two approaches with this factor:

Linear:

$$\phi = \phi(p, T) = \phi_{ref} \cdot (1 + \phi_c(p, T)). \quad (36)$$

Nonlinear:

$$\phi = \phi(p, T) = \phi_{ref} \cdot e^{\phi_c(p, T)}. \quad (37)$$

For both two approaches, porosity is a function of pressure and temperature.

2.12 Relative Permeabilities

There are two ways for calculating relative permeabilities. The first one is to use analytical correlations, and the second one is to use input tables. The water phase relative permeability, k_{rw} , can be obtained with interpolation from oil-water relative permeability table, which is a function of S_w (and temperature):

$$k_{rw} = k_{rw}(S_w). \quad (38)$$

The gas phase relative permeability, k_{rg} , can be calculated the same from a gas-oil relative permeability table or gas-liquid relative permeability table, which is a function of S_g (and temperature):

$$k_{rg} = k_{rg}(S_g). \quad (39)$$

As for the relative permeability of oil k_{ro} , there are several models available ([45]; [44], 1961; [43]; [42]). In our model, the Stones model II method ([41]) is applied:

$$k_{ro} = k_{ro}(S_w, S_g) \quad (40)$$

$$= k_{rocw} \left[\left(\frac{k_{row}(S_w)}{k_{rocw}} + k_{rw}(S_w) \right) \left(\frac{k_{rog}(S_g)}{k_{rocw}} + k_{rg}(S_g) \right) - k_{rw}(S_w) - k_{rg}(S_g) \right], \quad (41)$$

where k_{rocw} is the oil-water two-phase relative permeability to oil at connate water saturation, k_{rog} is the oil-gas two-phase relative permeability to oil, and k_{row} is the oil-water two-phase relative permeability to oil.

$$k_{rocw} = k_{row}(S_w = S_{wc}) = k_{rog}(S_g = 0). \quad (42)$$

k_{row} and k_{rog} are interpolated from input tables.

2.13 Energy

Enthalpy is a measurement of energy in a thermodynamic system, which is equal to the internal energy of the system plus the product of pressure and volume. The enthalpy of a gas component is calculated as follows ([40]):

$$H_{g,i} = H_{g,i}(T) = \int_{T_{ref}}^T (cpg1_i + cpg2_i \cdot t + cpg3_i \cdot t^2 + cpg4_i \cdot t^3) dt, \quad (43)$$

$cpg1_i$, $cpg2_i$, $cpg3_i$, and $cpg4_i$, are constants for component i . The gas phase enthalpy can be calculated by a weighted mean with gas molar fractions y_i :

$$H_g = H_g(p, T, S_w, S_g, x_i, y_i) = \sum_i^{N_c} y_i H_{g,i}. \quad (44)$$

For the oil and water phases, the heat of vaporization should be considered, which can be calculated by:

$$H_{v,i} = H_{v,i}(T) = hvr_i \cdot (T_{crit,i} - T)^{ev_i}. \quad (45)$$

The enthalpy of a liquid component can be calculated as:

$$H_i = H_i(T) = H_{g,i} - H_{v,i}. \quad (46)$$

where $H_{g,i}$ is the enthalpy of component i in the gas phase. As a result, for the water phase which only includes one component, the enthalpy is:

$$H_w = H_w(T) = H_{g,W} - H_{v,W}. \quad (47)$$

For the oil phase, as a mixture, the enthalpy is:

$$H_o = H_o(p, T, x_i) = \sum_i^{n_{co}} x_i (H_{g,O[i]} - H_{v,O[i]}). \quad (48)$$

The internal energy for oil, gas, and water phases ([40]) are calculated as:

$$U_w = U_w(T) = H_w - p/\rho_w, \quad (49)$$

$$U_o = U_o(p, T, x_i) = H_o - p/\rho_o, \quad (50)$$

$$U_g = U_g(p, T, S_w, S_g, x_i, y_i) = H_g - p/\rho_g. \quad (51)$$

For rock, a similar formula is used:

$$U_r = U_r(T) = cp1_r(T - T_{ref}) + \frac{cp2_r}{2}(T^2 - T_{ref}^2). \quad (52)$$

One thing to notice is that the internal energy for rock has a unit of energy per unit volume, while others have energy per unit amount of material. As mentioned above, there are two ways to calculate the volume of rock. The first one assumes the volume of rock (non-null) doesn't change, which is noted as constant rock in CMG STARS. The second one assumes the volume of the grid block doesn't change, which is noted as constant bulk in CMG STARS.

2.14 Well Modeling

A Peaceman's model is adopted for well modeling in this paper. A well may have many perforations, and each perforation at a grid cell, its well rate for phase α , $Q_\alpha = Vq_\alpha$, is calculated by the following formula ([2]):

$$Q_{\alpha,well} = WI \frac{\rho_\alpha k_{r\alpha}}{\mu_\alpha} (p_b - p_\alpha - \gamma_\alpha g(z_{bh} - z)), \quad (53)$$

where WI is the well index. In CMG STARS, well rate can be calculated using unweighted method,

$$Q_{\alpha,well} = WI (p_b - p_\alpha - \gamma_\alpha g(z_{bh} - z)), \quad (54)$$

where WI is user input value. A well index defines the relationship among a well bottom hole pressure, a flow rate and a grid block pressure. p_b is the bottom hole pressure defined at the reference depth z , z_{bh} is the depth of the perforation in grid cell, and p_α is the phase pressure in grid block m . Well index can be read from modelling file and it can also be calculated using analytical method. For a vertical well, it can be defined as:

$$WI = \frac{2\pi h_3 \sqrt{k_{11} k_{22}}}{\ln(\frac{r_e}{r_w}) + s}, \quad (55)$$

where r_e is equivalent radius. The calculation of well index can be controlled by several parameters, such as `geo`, `geoa`, `kh`, `kha` and `geofac`, whose details can be read from CMG STARS manual. Horizontal can be defined similarly. We should mention that well modeling is the most complicated part in reservoir simulations and various operation constraints can be defined, such as fixed bottom hole pressure, fix liquid and gas rate constraints and thermal constraints.

The bottom hole pressure update is handled differently in CMG STARS and in our simulator. In CMG STARS, the bottom hole pressure is updated by change or in the beginning of each time step. For the change option, CMG STARS updates bottom hole pressure if the change is large enough. In our simulator, the bottom hole pressure is updated in each Newton iteration.

2.14.1 Flash Calculation

In equation (53), ρ_α , $k_{r\alpha}$ and μ_α need to be calculated. For production wells, they are from the grid block that contains the perforation, which are straightforward. However, for injection wells, the mobility is the total mobility,

$$\frac{k_r}{\mu} = \frac{k_{ro}}{\mu_o} + \frac{k_{rw}}{\mu_w} + \frac{k_{rg}}{\mu_g}. \quad (56)$$

In CMG STARS, injection wells have two options, implicit mobility and explicit mobility. The implicit mobility is updated in each Newton iteration and the explicit mobility is updated at the beginning of each time step. Production wells also have two options, implicit mobility and explicit mobility. Iso-enthalpy flash calculation is required in each perforation to determine the status of injected fluids, such as pressure, temperature, distributions in three phases, and density. For example, the injected water (steam) can stay in liquid (pure water), steam (pure gas) and mixture of water and steam states depending on the wellbore pressure and temperature of a perforation.

The choice of mobility models affects the calculations of well rates, Jacobian matrix, and numerical treatment of each well. An injection well has three options: unweighted mobility (including well index), implicit mobility and explicit mobility. When unweighted mobility is applied, user input value is required for this well. The calculations for explicit mobility is easier than implicit mobility, and many partial derivatives are ignored when assembling Jacobian matrix. The explicit mobility is less accurate than implicit mobility, but it can be faster and more stable. When the implicit mobility is applied, many properties have to be updated in each Newton iteration. A production well has two options: implicit mobility and explicit mobility. In our simulator, each well can be assigned to any allowed mobility models. For example, well 1 is an injection well and it applies unweighted mobility, well 2 is also an injection well and it applies explicit mobility, and well 3 is a production well and it applies implicit mobility.

2.14.2 Fixed Bottom Hole Pressure

When the fixed bottom hole pressure condition is applied to a well, the well equation is written as,

$$p_b = c, \quad (57)$$

where c is pressure and s is a constant.

2.14.3 Fixed Rate

Fixed rate constraints are commonly used, including fixed oil rate, fixed water rate, fixed gas rate, and fixed liquid rate (oil and water). The rate can be reservoir rate or surface rate. The volume of a fluid in reservoir condition can be obtained easily.

However, the volume of a fluid in surface condition requires flash calculation to determine the distribution in oil, water and gas phases. There are two ways to separate phase: segregated method and PT-flash method. The segregated method is easy but the PT-flash is tricky. In CMG STARS, the segregated method is the default. For phase α , its fixed rate constraint is described by the following equation:

$$\sum_m (Q_{\alpha,well})_m = c, \quad (58)$$

where c is a constant rate and known. The fixed liquid rate is written as,

$$\sum_m (Q_{w,well})_m + \sum_m (Q_{o,well})_m = c, \quad (59)$$

2.14.4 Constant Heat Transfer Model

CMG STARS is the most popular thermal simulator, and it has many heater models, such as constant heat transfer model (**heatr** in CMG STARS), convective heat transfer model and heat well, which are applied to model heating stage. The first two types can be defined in any grid block. However, the heat well (**HTWELL** in CMG STARS) can only be defined in a real well, such as injection well and production well. The constant heat transfer model means in some grid blocks, there exist heat transfer at certain rate, such as 1,000 Btu/day. The energy exchange can occur in any grid block. The heat transfer can be turned on or off using schedule.

2.14.5 Convective Heat Transfer Model

Constant heat transfer model simulates constant heat exchange while convective heat transfer model defines dynamic heat transfer, which is controlled by two parameters: **uhtr** (proportional heat transfer coefficient, Btu/day-F) and **tmpset** (temperature setpoint, F) (**UHTR** and **TEMSET** in CMG STARS). If **uhtr** is positive, it means to gain heat from source, the heat rate in a grid block is calculated as,

$$q = \begin{cases} \text{uhtr} * (\text{tmpset} - T), & \text{if } \text{tmpset} > T; \\ 0, & \text{if } \text{tmpset} \leq T; \end{cases} \quad (60)$$

If **uhtr** is negative, it means the reservoir loses heat, the heat rate in a grid block is calculated as,

$$q = \begin{cases} \text{uhtr} * (T - \text{tmpset}), & \text{if } \text{tmpset} < T; \\ 0, & \text{if } \text{tmpset} \geq T; \end{cases} \quad (61)$$

where T is the reservoir temperature.

2.14.6 Heater Well

As mentioned above, the constant and convective heat transfer models can be defined in any grid block. Another heat model is also developed in CMG STARS and our simulator, which is noted as **HTWELL** as in CMG STARS. This type of heater is defined in a production or injection well, which has the same perforations as the well contains the heater well. This heater well is more complicated than constant and convective heater transfer models, which has more controls, such as heat rate model (**HTWRATE** or **HTWRATEPL** in CMG STARS), temperature model (**HTWTEMP** in CMG STARS), heat index model (**HTWI** in CMG STARS), and dual rate/temperature model. The dual rate/temperature model has two direction controls: uni-directed (**UNIDIRECT** in CMG STARS) and bi-directed (**BIDIRECT** in CMG STARS).

For heat rate control (model), the heat rate in a perforation m is calculated as,

$$q = q_{hspec} = Q_{hspec} L_m / L_w, \quad (62)$$

where q is the heat rate, Q_{hspec} is total heat rate defined by **HTWRATE**, L_m is the length of the layer well completion, and L_w is the total well length (sum of L_m).

For temperature model, the heat rate in a perforation is calculated as,

$$q = q_{wspec} = I_m * (T_{wspec} - T_m), \quad (63)$$

where I_m is the heat conduct index (or heat index), T_{wspec} is specify wellbore temperature, T_m is grid block temperature. We should mention that there are two method for calculating heat conduct index: 1) use thermal conductivity formula introduced in mathematical model section; 2) use heat index introduced here (by turning HTWI on in CMG STARS). For heat index model, the user input well index or internal index can be converted to heat index.

When dual rate/temperature model is enabled, the rate model and temperature model are switched automatically. For heating ($Q_{hspec} > 0$), the heat rate in a layer is defined as,

$$q = \min\{I_m * \Delta T_m, q_{hspec}\}, \quad (64)$$

where ΔT_m is defined as,

$$\Delta T_m = \begin{cases} \max\{T_{wspec} - T_k, 0\}, & \text{for UNIDIRECT} \\ T_{wspec} - T_k, & \text{for BIDIRECT,} \end{cases} \quad (65)$$

The T_k is reservoir temperature in a grid block. The UNIDIRECT option shuts down heater when temperature difference is zero; while BIDIRECT allows heating and cooling (heat loss).

For cooling ($Q_{hspec} < 0$), the heat rate in a layer is defined as,

$$q = \max\{I_m * \Delta T_m, q_{hspec}\}, \quad (66)$$

where ΔT_m is defined as,

$$\Delta T_m = \begin{cases} \min\{T_{wspec} - T_k, 0\}, & \text{for UNIDIRECT} \\ T_{wspec} - T_k, & \text{for BIDIRECT,} \end{cases} \quad (67)$$

The UNIDIRECT option shuts down cooling well, and the BIDIRECT option allows bidirectional heat transfer. In both cases, the BIDIRECT can simulate autoheater and autocooler. Their meanings are shown by Figure 1 [40].

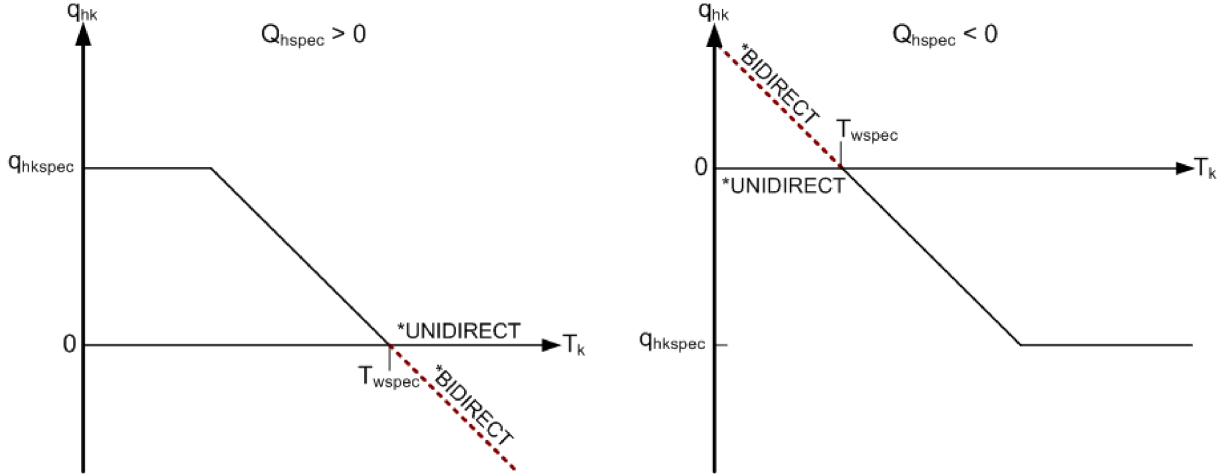


Figure 1: HTWELL: dual rate/temperature model [40]

2.14.7 Subcool Control

Subcool control is also known as steamtrap, which is used to prevent the production of live steam. It does this by keeping the well's flowing bottomhole pressure (and hence the pressure in the grid block containing the well) high enough that live steam does not appear in the well block [40].

The well constraint equation solved is written as,

$$T_{sat}(p_{wb}) - T_k = c, \quad (68)$$

where c is a pre-defined temperature difference, T_{sat} is the steam saturation temperature corresponding to wellbore pressure p_{wb} defined in the perforation, and T_k is the temperature defined in the grid block that contains the perforation.

3 Numerical Methods

In our previous previous work, a few reservoir simulators and their numerical methods have been reported [21, 31, 33, 32, 61]. The simulators share similar methods, such as time discretization scheme, spatial discretization scheme, decoupling method, linear solver and preconditioners [21]. For the sake of completeness, the numerical methods are introduced in this section.

3.1 Time Discretization

Let u be a vector function, u^n be the solution of u at a given time step n , and F be non-linear mathematical system of thermal reservoir model. The backward Euler method is applied to discretize a time derivative,

$$\left(\frac{\partial u}{\partial t}\right)^{n+1} = \frac{u^{n+1} - u^n}{\Delta t} = F(u^{n+1}, t^{n+1}), \quad (69)$$

where Δt is a time step. An implicit non-linear system is obtained, which is solved at each time step using Newton method.

3.2 Spatial Discretization

The natural variables are applied as knowns, which are also called Type A variables, including pressure, temperature, saturations, and molar fractions (oil components in oil phase and non-condensable gas in gas phase). The variables do not change during the simulation. However, depending on the gas phase status, one constrained equation is switched. If gas phase exist, the following equation is applied,

$$\sum_i y_i = 1. \quad (70)$$

If gas phase does not exist, the following equation is switched,

$$S_g = 0. \quad (71)$$

The status of gas phase has to be checked block by block in each Newton iteration.

When fluids move in a reservoir, there may be fluid exchange in two neighboring grid blocks, which is described by transmissibility. Assuming d ($d = x, y, z$) is a space direction and A be the area of a face in the d direction, the transmissibility $K_{\alpha,d}$ for phase α ($\alpha = o, w, g$) is defined as

$$T_{\alpha,d} = \frac{KA}{\Delta d} \times \frac{K_{r\alpha}}{\mu_\alpha} \rho_\alpha, \quad (72)$$

where Δd is the grid block length in the d direction, K is the absolute permeability, $K_{r\alpha}$ is the relative permeability of phase α , μ_α is the viscosity of phase α and ρ_α is the molar density of phase α . The transmissibility is defined on each face of a grid block. If a face is internal face shared by two grid blocks, its value is the same for these two blocks. If the face is a boundary face, the transmissibility is zero, as the no-flow boundary condition is applied. Different weighting schemes must be applied to average different properties at an interface. The left part, $\frac{KA}{\Delta d}$, is geometric properties, and the harmonic averaging method is applied. The right part, $\frac{K_{r\alpha}}{\mu_\alpha} \rho_\alpha$, relies on fluid properties, and the upstream averaging method is applied [64]. The upstream finite difference method is employed to discretize the model.

3.3 Linear Solver

The Jacobian matrix from Newton method is highly ill-conditioned, and the Krylov subspace solvers are applied to solve the linear system $Ax = b$. The key to an effective solution method is to choose a proper preconditioner M , which should be easy to setup and effective. In our previous work, a family of scalable CPR-type methods [21] have been developed for reservoir simulations, which have been applied to black oil model, compositional, in-situ combustion and the general thermal model in this paper. The unknowns are numbered grid block by grid block and the resulted matrix in each iteration is block-wise,

$$A = \begin{pmatrix} A_{11} & \cdots & \cdots & A_{1n} \\ A_{21} & A_{22} & \cdots & A_{2n} \\ \cdots & \cdots & \cdots & \cdots \\ A_{n1} & A_{n2} & \cdots & A_{nn} \end{pmatrix}, \quad (73)$$

where each sub-matrix A_{ij} is a square matrix.

3.4 Decoupling Methods

A proper decoupling method is critical to the success of the CPR-type preconditioners. In general, the decoupling method is applied before applying the CPR-type preconditioners, which converts the original linear system to an equivalent linear system,

$$(D^{-1}A)x = D^{-1}b. \quad (74)$$

Several decoupling methods have been proposed, such as Quasi-IMPES, True-IMPES [60], Alternate Block Factorization (ABF) [62], full row sum (FRS) and dynamic row sum (DRS) [63] methods. The idea of ABF method is simple, which is defined as,

$$D_{abf} = \text{diag}(A_{11}, A_{22}, \dots, A_{nn}). \quad (75)$$

It converts the block diagonal part to identity matrix. This method requires to calculate the inverse of each diagonal part, and the matrix-matrix multiplications are performed for each sub-matrix. The FRS decoupling method is described as,

$$D_{frs}^{-1} = \text{diag}(D_1, D_2, \dots, D_n), \quad (76)$$

where,

$$D_i = \begin{pmatrix} 1 & 1 & \dots & 1 \\ 0 & 1 & \dots & 0 \\ \dots & \dots & \dots & \dots \\ 0 & \dots & 1 & 0 \\ 0 & 0 & 0 & 1 \end{pmatrix}. \quad (77)$$

The diagonal part and the first row are 1 and all other locations are 0, which means to add the all rows to the first row. The DFS decoupling method is a simplified version of the FRS method, and details can be read in [63].

The Gauss-Jordan elimination (Gauss elimination, GJE) method has been used to solve linear systems. Its idea is to convert $[D|A|b]$ to an equivalent linear system $[I|\tilde{A}|\tilde{b}]$ by Gauss-Jordan elimination method, and the \tilde{b} is final solution. In this paper, it is adopted as a decoupling method and is applied grid block by grid block to turn the diagonal matrices to identity matrix. Pivoting technique is used and only row reordering is involved. Since the decoupling is processed block by block, no communication is required, which is friendly to parallel computing. The GJE decoupling is more efficient than the ABF method.

When the CPR-type preconditioners are applied to reservoir simulations, it is important to keep the pressure matrix positive definite. FRS method helps to enhance this property, from which the CPR-type preconditioners can benefit. In the first stage, FRS or DRS methods are applied; then ABF or GJE methods are used as the second stage. In this case, two-stage decoupling methods are developed, which are noted as FRS+ABF, FRS+GJE, DRS+ABF and DRS+GJE.

3.5 Preconditioners

Several scalable CPR-type preconditioner have been proposed [21], such as CPR-FP, CPR-PF, CPR-FPF, and CPR-FFPF methods. According to our practices, the CPF-FPF method, which is a three-stage preconditioner, is effective for black oil model and thermal model. It is described by Algorithm 1, where the first step is to solve an approximate solution using restricted additive Schwarz (RAS) method, the third step is to solve the subproblem by algebraic multi-grid method (AMG), the fifth step is to get an approximate solution again using restricted additive Schwarz method, and the second step and the forth step are to calculate residual.

It is well-known that the RAS method is scalable for parallel computing. Parallel AMG method is also scalable. However, multiple layers are applied inside AMG and each layer gets coarser and coarser, which introduces complicated communication patters. Also, since the layers gets coarser and denser, more communication could be introduced and scalability will be reduced if AMG has too many layers (levels). Different coarsening algorithms and interpolation methods also affect the scalability and convergence of AMG solver. The CPR-FPF method is a combination of RAS method and AMG method, which is also scalable. Here we should also mention that the setup phase of the parallel AMG method is computationally intense. For small model or easy model, the RAS method should work well too. In-house solvers and preconditioners have been developed, and the only external library that the thermal simulator requires is the parallel AMG solver, Hypre. The sub-problem for each CPU from RAS method is solved by ILUT by default, which can also be solved by ILU(k) or block ILU(k) [21]. The default parameters of AMG are listed as following.

```

BMAMG_PARS amg_pars_default =
{
  /* maxit */           1,
  /* num_funcs */      -1,
  /* max_levels */     -1,
  /* strength */       0.5,
  /* max_row_sum */    0.9,
  /* trunc error */   1e-2,

  /* coarsen_type */   Falgout,
  /* cycle_type */     v-cycle,
  /* relax_type */     hybrid Gauss-Seidel-forward,
  /* coarsest_relax_type */ hybrid symmetric Gauss-Seidel,
  /* interp type */    cmi,
  /* itr relax */      2,
};

```

Figure 2: Default parameters of AMG method

Algorithm 1 The CPR-FPF Method

- 1: $y = RAS(A)^{-1}f$
 - 2: $y = y + \Pi_p AMG(A_{PP})^{-1} \Pi_r r$
 - 3: $y = RAS(A)^{-1}f$
-

The design and implementation details of the linear solver and preconditioners can be found in [53]. The thermal simulator and some other reservoir simulators base on the in-house platform, PRSI [54], which provides gridding, DOF (degrees of freedom), mapping, solver and preconditioner, well modeling, keyword parsing, option parsing, visualization, parallel input and output through MPI-IO, memory management, and communication management. The platform is implemented by C and utilizes MPI for communications. It is highly scalable and previous studies have shown that the platform and in-house simulators have ideal scalability[54].

4 Numerical Studies

Numerical experiments are presented here, which includes a few sections. The first section validates our results against CMG STARS, which is the most widely applied thermal simulator. The purpose is to prove the correctness of our numerical methods, models and implementation. The second section validates well control methods against CMG STARS. The third section studies numerical performance of our methods. The fourth section tests the scalability of our thermal simulator using some giant models.

We should mention that the models are randomly generated. The only purpose is to validate our results and CMG STARS. If the model is the same, the results from our simulator and CMG STARS should be very close. By comparing results from CMG STARS, the implementation and accuracy of various properties and well controls can be verified. In the numerical section, the injection wells and the production wells are placed to be close to each other such that the models are hard to solve.

4.1 Validation

This section covers a few commonly used models, pure heavy oil, heavy oil and light oil, oil and non-condensable gas (NCG).

4.1.1 Heavy Oil

Example 1 The grid dimension of the model is $9 \times 9 \times 4$, with sizes of 29.17 ft, 29.17 ft and 10 ft in x , y and z direction. Details of the model are presented in the following tables. Water component and one heavy oil component are simulated. As shown by Figure 3, the water-oil relative permeability and the liquid-gas relative permeability have sharp change. It has five vertical wells: one injection well in the center (5, 5), and four production wells in four corners, (1, 1), (1, 9), (9, 1) and (9, 9). The bottom hole pressure of the injection well, water rate and oil rate of each well are shown from Figure 4 to Figure 15. All results are compared with CMG STARS.

S_w	k_{rw}	k_{row}
0.45	0.0	0.4
0.47	0.000056	0.361
0.50	0.000552	0.30625
0.55	0.00312	0.225
0.60	0.00861	0.15625
0.65	0.01768	0.1
0.70	0.03088	0.05625
0.75	0.04871	0.025
0.77	0.05724	0.016
0.80	0.07162	0.00625
0.82	0.08229	0.00225
0.85	0.1	0.0

Table 1: Input data for Example 1 (cont'd).

S_l	k_{rg}	k_{rog}
0.45	0.2	0.0
0.55	0.14202	0.0
0.57	0.13123	0.00079
0.60	0.11560	0.00494
0.62	0.10555	0.00968
0.65	0.09106	0.01975
0.67	0.08181	0.02844
0.70	0.06856	0.04444
0.72	0.06017	0.05709
0.75	0.04829	0.07901
0.77	0.04087	0.09560
0.80	0.03054	0.12346
0.83	0.02127	0.15486
0.85	0.01574	0.17778
0.87	0.01080	0.20227
0.90	0.00467	0.24198
0.92	0.00165	0.27042
0.94	0.0	0.30044
1.	0.0	0.4

Table 2: Input data for Example 1 (cont'd).

Initial condition	
$k_{x,y,z}$ (md)	313, 424, 535
ϕ	0.3
ϕ_c	5e-4
p (psi)	75
T ($^{\circ}F$)	125
$S_{w,o,g}$	0.45, 0.55, 0.

Table 3: Input data for Example 1

Well conditions		
Injector	water (<i>bbl/day</i>)	100
	wi (<i>ft · md</i>)	1e4
	tinjw (<i>°F</i>)	450
	steam quality	0.4
Producer 1	bhp (<i>psi</i>)	17
	wi (<i>ft · md</i>)	1e4
	steamtrap (<i>°F</i>)	10
Producer 2	bhp (<i>psi</i>)	17
	wi (<i>ft · md</i>)	1e4
	steamtrap (<i>°F</i>)	20
Producer 3	bhp (<i>psi</i>)	17
	wi (<i>ft · md</i>)	1e4
	steamtrap (<i>°F</i>)	30
Producer 4	bhp (<i>psi</i>)	17
	wi (<i>ft · md</i>)	1e4
	steamtrap (<i>°F</i>)	40

Table 4: Input data for Example 1 (cont'd).

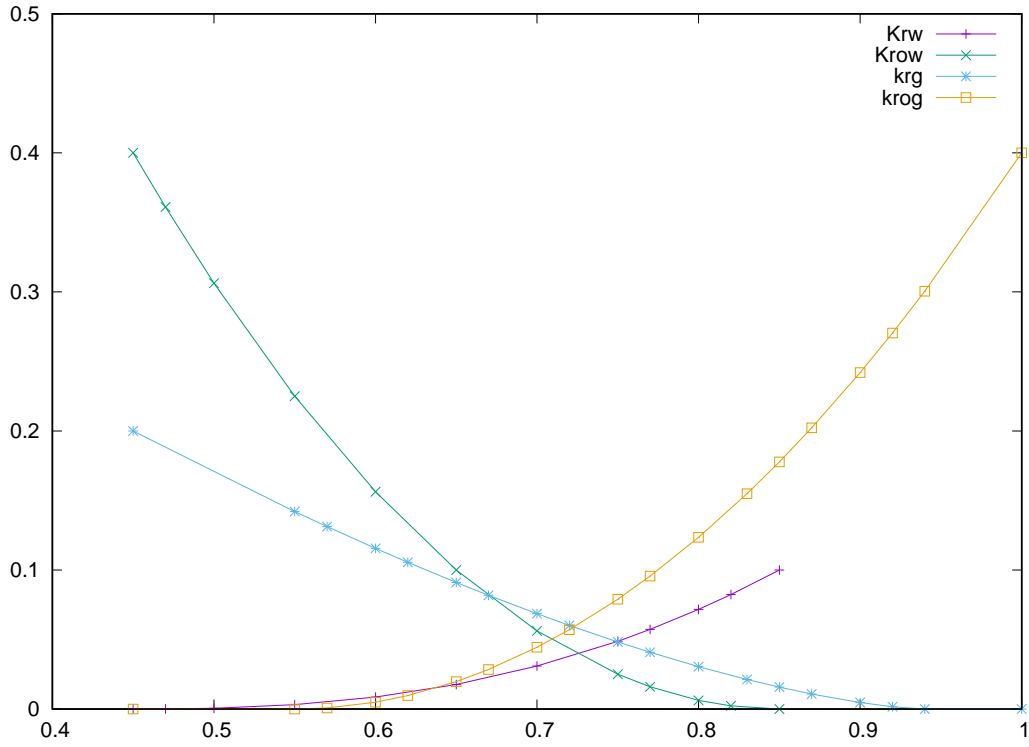


Figure 3: Example 1, heavy oil: relative permeability of the water-oil table and liquid-gas table

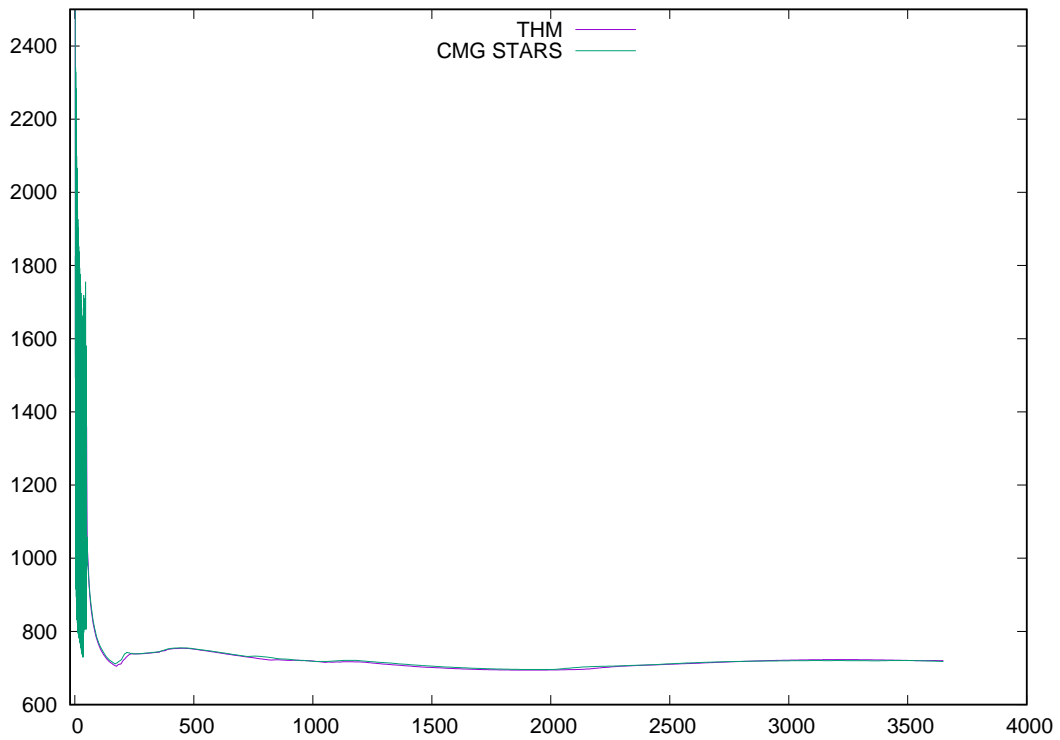


Figure 4: Example 1, heavy oil: injection well, bottom hole pressure (psi)

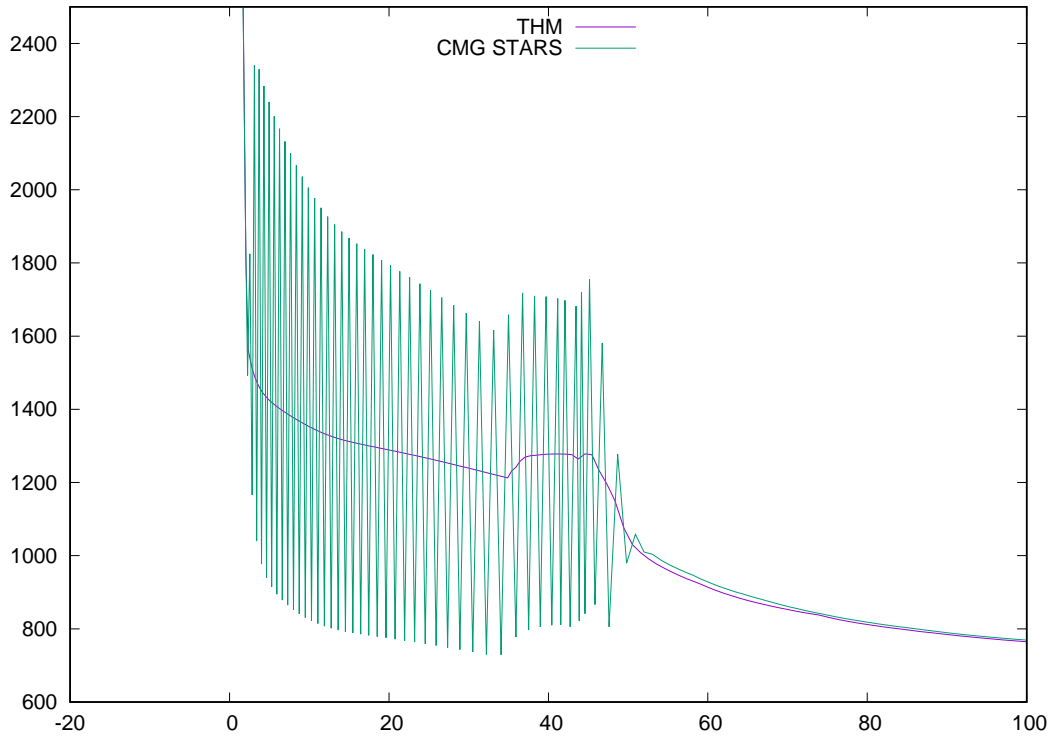


Figure 5: Example 1, heavy oil: injection well, bottom hole pressure (psi), first 100 days

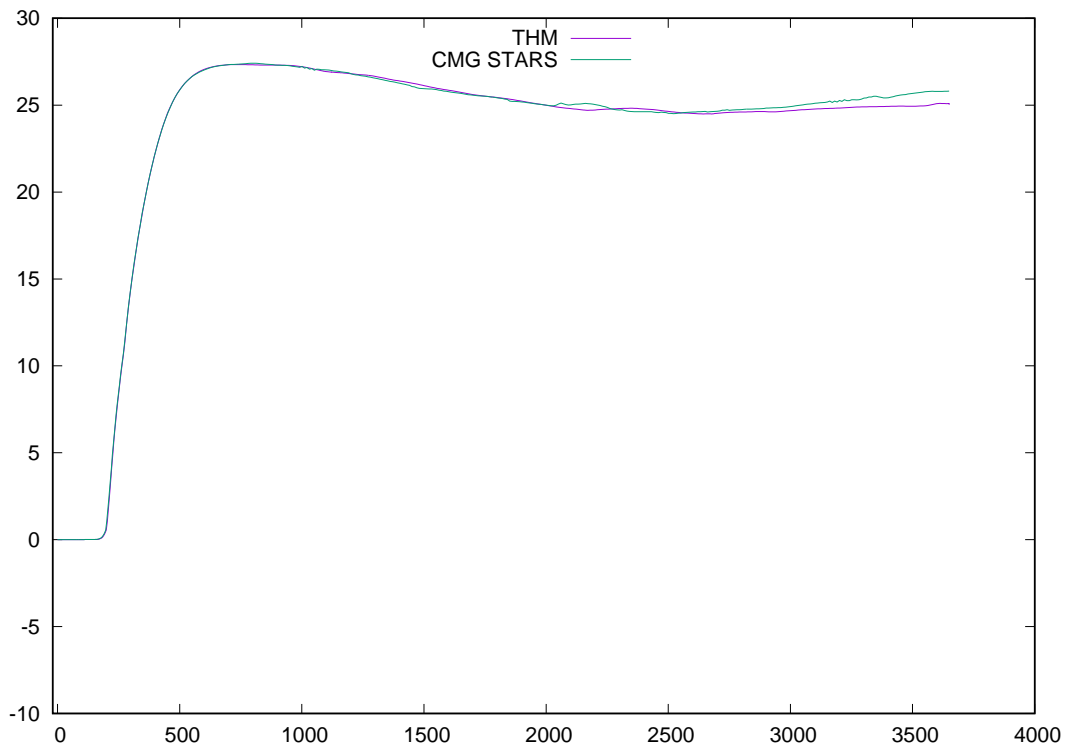


Figure 6: Example 1, heavy oil: water production rate (bbl/day), first production well

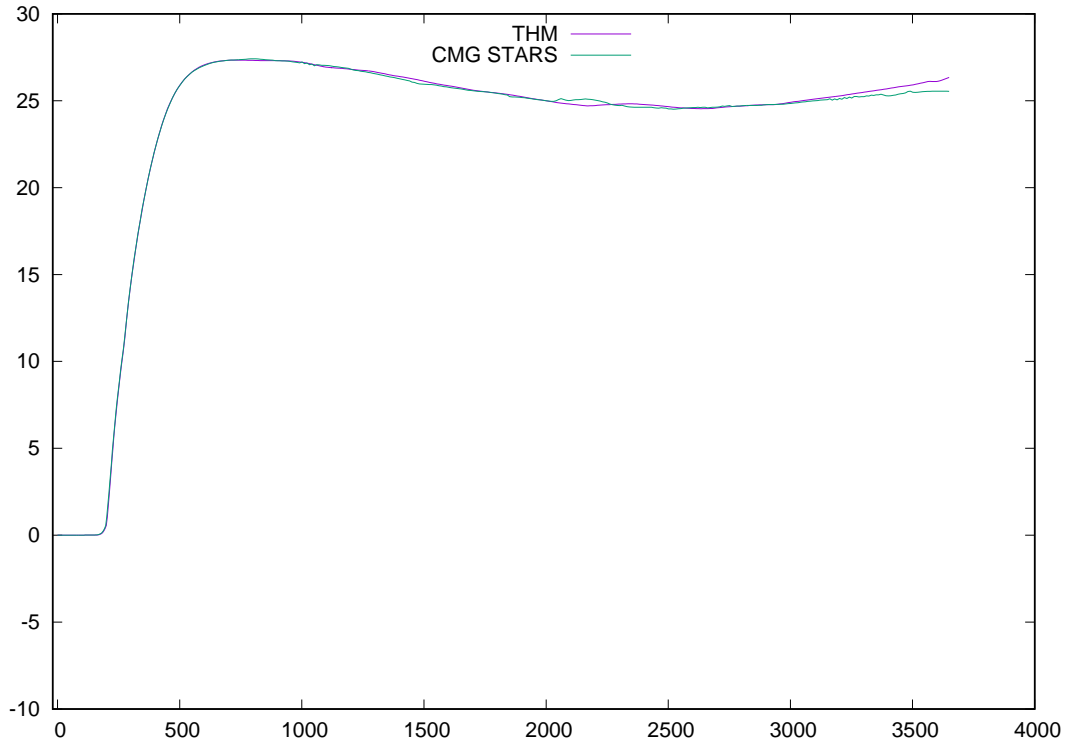


Figure 7: Example 1, heavy oil: water production rate (bbl/day), second production well

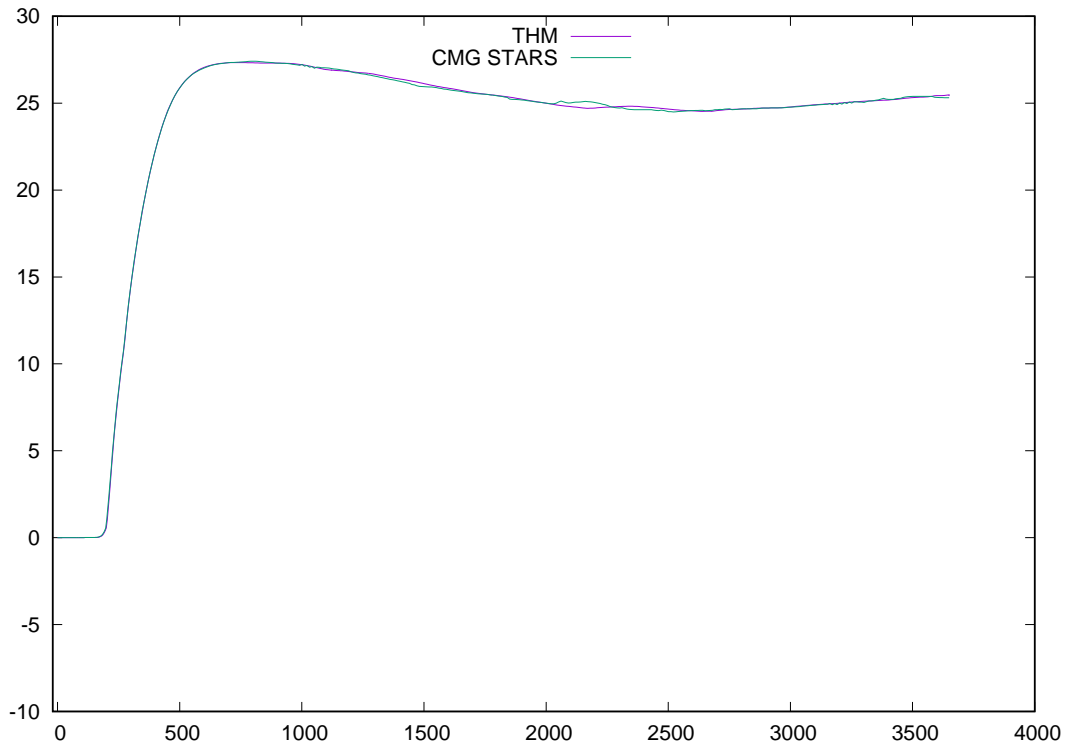


Figure 8: Example 1, heavy oil: water production rate (bbl/day), third production well

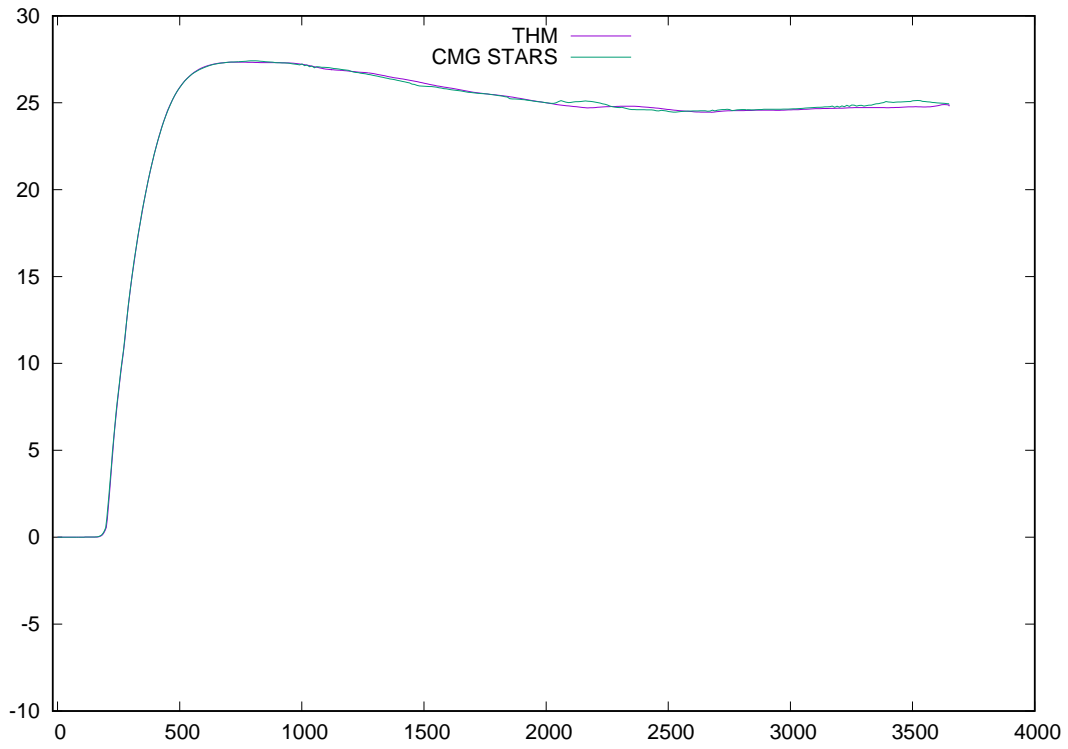


Figure 9: Example 1, heavy oil: water production rate (bbl/day), forth production well

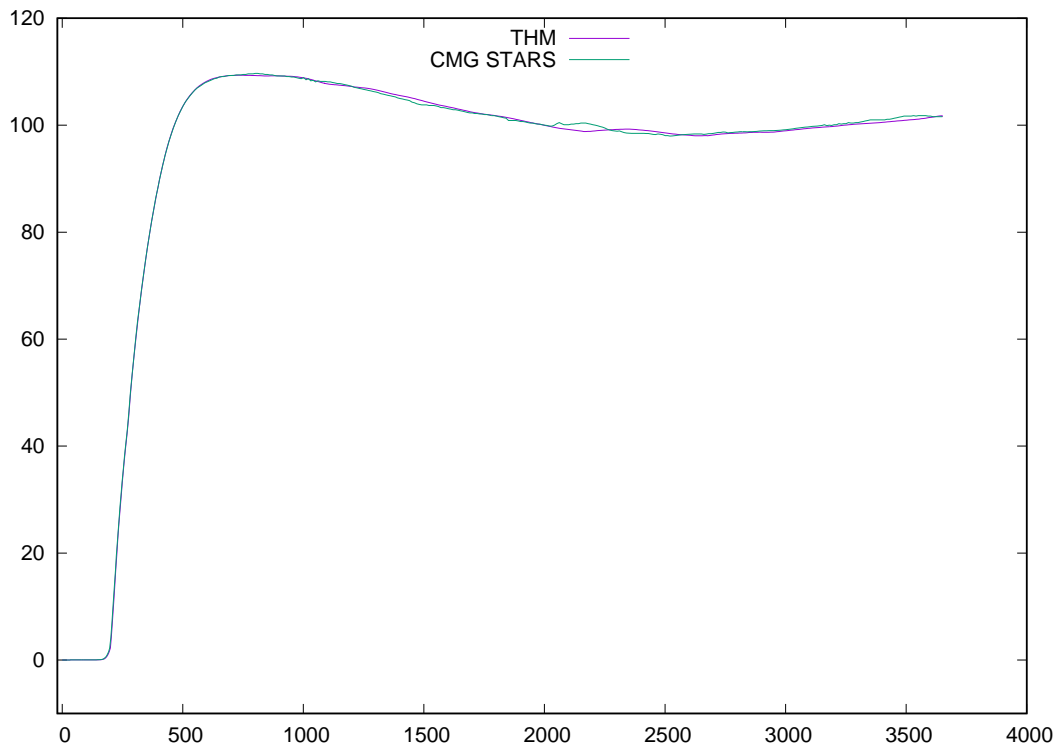


Figure 10: Example 1, heavy oil: total water production rate (bbl/day)

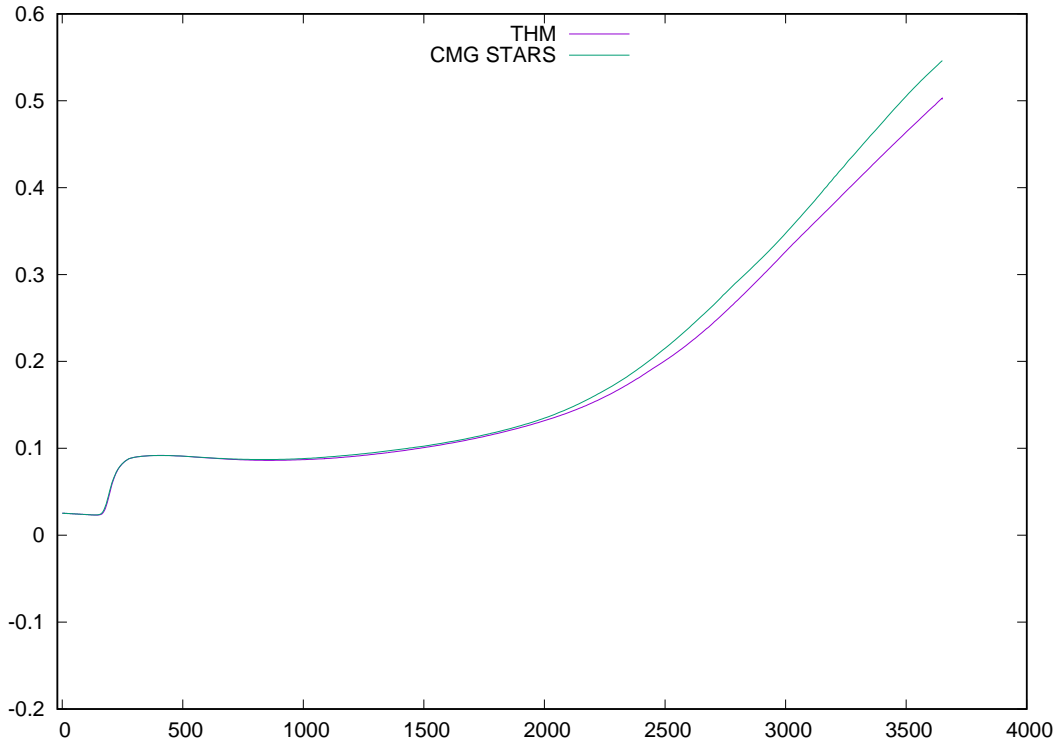


Figure 11: Example 1, heavy oil: oil production rate (bbl/day), first production well

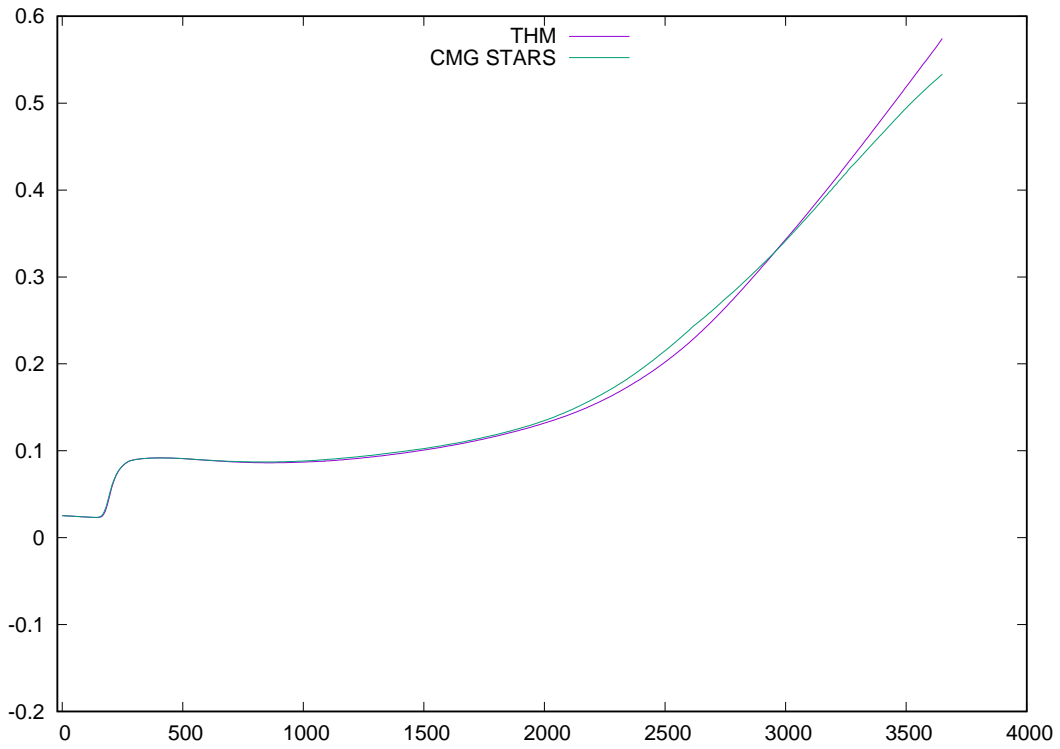


Figure 12: Example 1, heavy oil: oil production rate (bbl/day), second production well

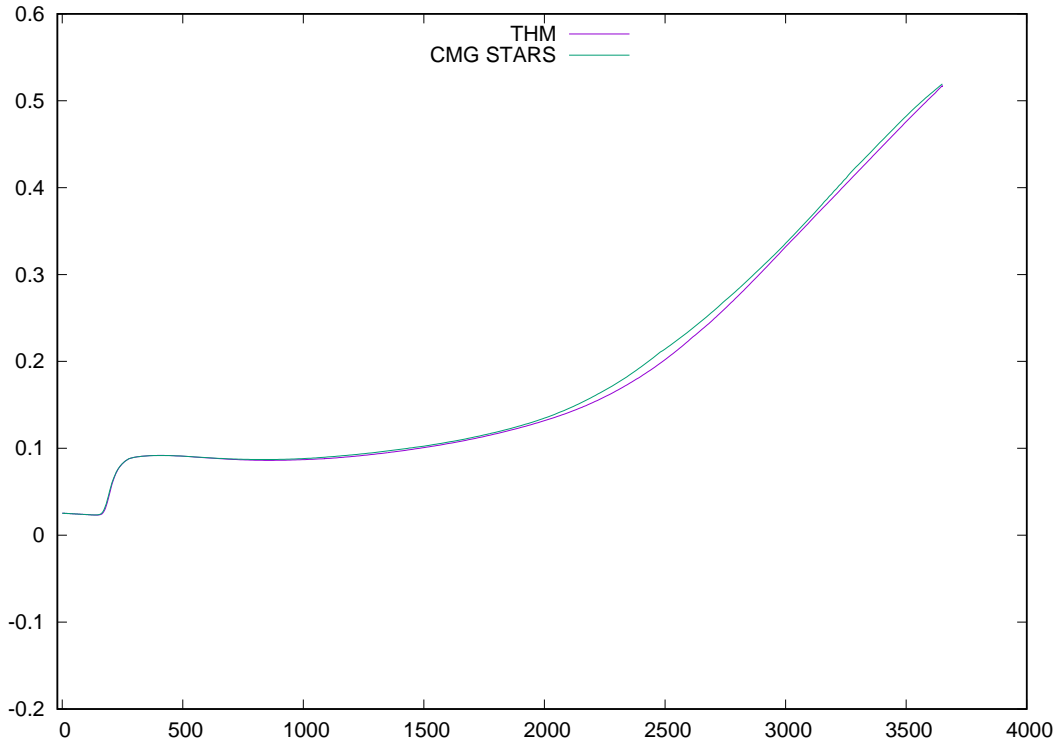


Figure 13: Example 1, heavy oil: oil production rate (bbl/day), third production well

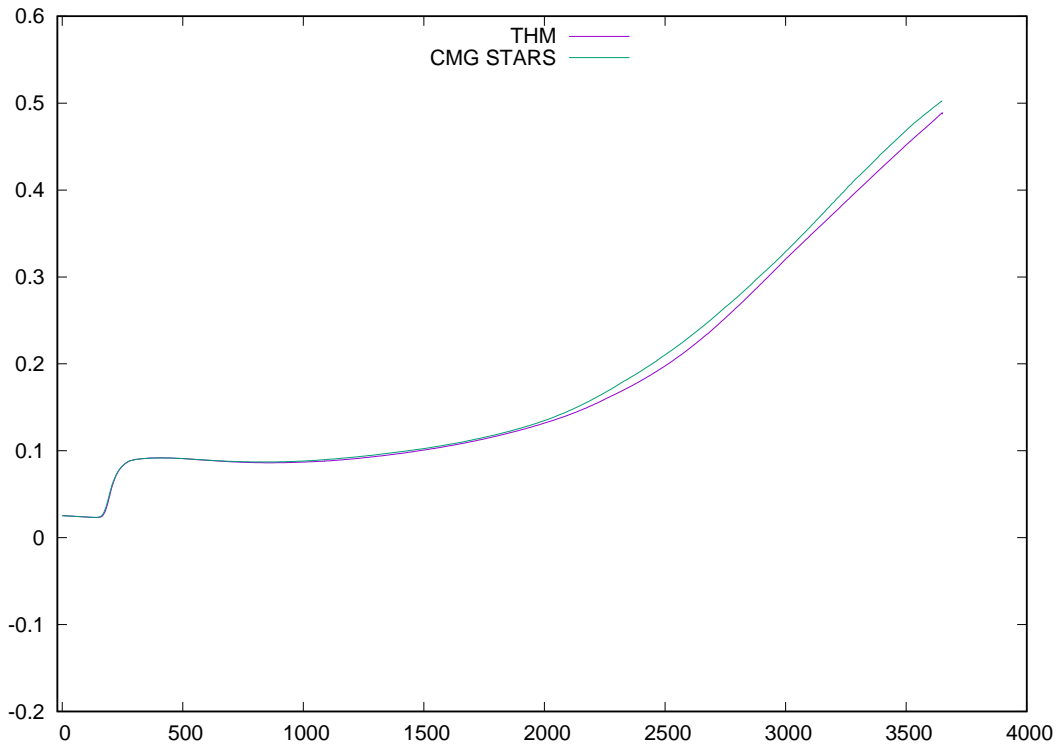


Figure 14: Example 1, heavy oil: oil production rate (bbl/day), fourth production well

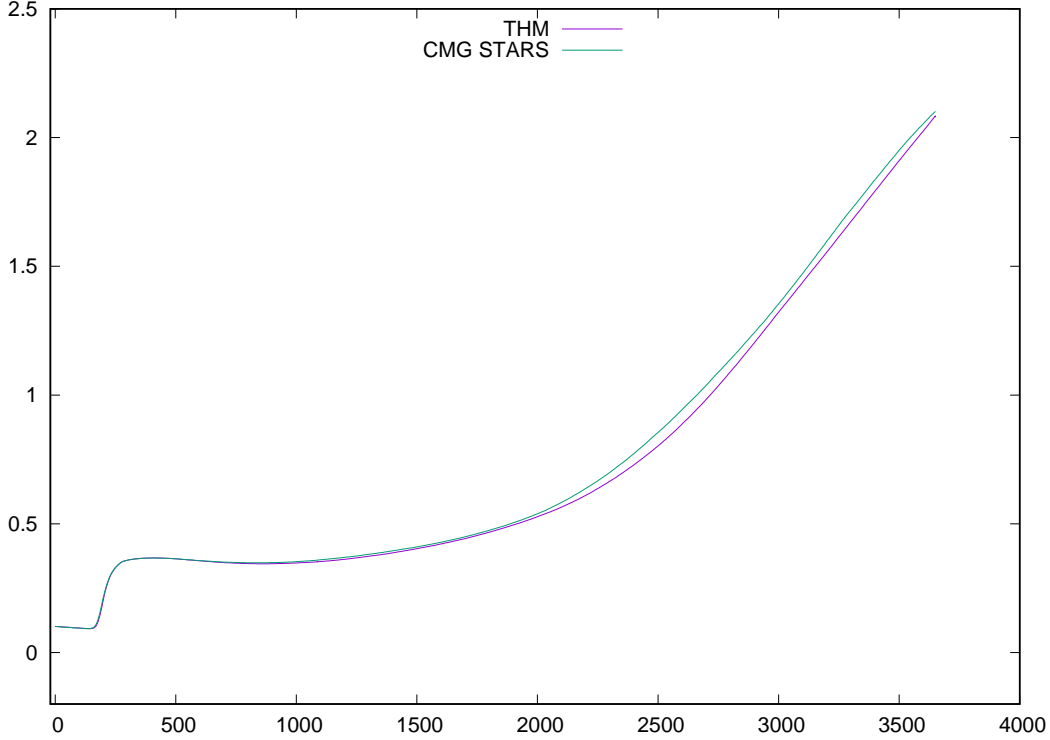


Figure 15: Example 1, heavy oil: total oil production rate (bbl/day)

Figure 4 is the bottom hole pressure of the injection well. Figure 6 is the water production rate of the first production well. Figure 7 is the water production rate of the second production well. Figure 8 is the water production rate of the third production well. Figure 9 is the water production rate of the fourth production well. Figure 10 is the total water production rate of all production wells. Figure 11 is the oil production rate of the first production well. Figure 12 is the oil production rate of the second production well. Figure 13 is the oil production rate of the third production well. Figure 14 is the oil production rate of the fourth production well. Figure 15 is the total oil production rate of all production wells. All figures show that our results match CMG STARS very well, which confirms our methods and implementation are correct.

4.1.2 Heavy Oil and Light Oil

Example 2 This model is similar as Example 1 except that a light oil component is added and the well operations are changed. It has five vertical wells: one injection well in the center (5, 5), and four production wells in four corners, (1, 1), (1, 9), (9, 1) and (9, 9). The bottom hole pressure of the injection well, water rate and oil rate of each well are shown from Figure 16 to Figure 32. All results are compared with CMG STARS.

Initial condition	
$k_{x,y,z}$ (md)	313, 424, 535
ϕ	0.3
ϕ_c	5e-4
p (psi)	4000
T ($^{\circ}F$)	125
$S_{w,o,g}$	0.45, 0.55, 0.
x	0.6, 0.4

Table 5: Input data for Example 2

Properties	LO
M (<i>lb/lbmole</i>)	250
p_{crit} (<i>psi</i>)	225
T_{crit} ($^{\circ}F$)	800
ρ_{ref} (<i>lbmole/ft³</i>)	0.2092
cp (<i>1/psi</i>)	5.e-6
$ct1$ (<i>1/°F</i>)	3.8e-4
$cpg1$ (<i>Btu/(°F · lbmol)</i>)	247.5
hvr (<i>Btu/(°F^{ev} · lbmol)</i>)	657
ev	0.38
avg (<i>cp/°F</i>)	5.e-5
bvg	0.9
$avisc$ (<i>cp</i>)	0.287352
$bvisc$ ($^{\circ}F$)	3728.2
$kv1$ (<i>psi</i>)	7.9114e4
$kv4$ ($^{\circ}F$)	-1583.71
$kv5$ ($^{\circ}F$)	-446.78

Table 6: Input data for Example 2

Well conditions		
Injector	water (<i>bbl/day</i>)	100
	wi (<i>ft · md</i>)	1e4
	tinjw ($^{\circ}F$)	450
	steam quality	0.3
Producer 1	bhp (<i>psi</i>)	17
	wi (<i>ft · md</i>)	2e4
Producer 2	bhp (<i>psi</i>)	17
	wi (<i>ft · md</i>)	3e4
Producer 3	bhp (<i>psi</i>)	17
	wi (<i>ft · md</i>)	4e4
Producer 4	bhp (<i>psi</i>)	17
	wi (<i>ft · md</i>)	5e4

Table 7: Input data for Example 2 (cont'd).

Figure 16 is the bottom hole pressure of the injection well. Figure 18 is the water production rate of the first production well. Figure 19 is the water production rate of the second production well. Figure 20 is the water production rate of the third production well. Figure 21 is the water production rate of the fourth production well. Figure 22 is the total water production rate of all production wells. Figure 23 is the gas production rate of the first production well. Figure 24 is the gas production rate of the second production well. Figure 25 is the gas production rate of the third production well. Figure 26 is the gas production rate of the fourth production well. Figure 27 is the total gas production rate of all production wells. Figure 28 is the oil production rate of the first production well. Figure 29 is the oil production rate of the second production well. Figure 30 is the oil production rate of the third production well. Figure 31 is the oil production rate of the fourth production well. Figure 32 is the total oil production rate of all production wells. All figures show that our results match CMG STARS very well, which confirms our methods and implementation are correct.

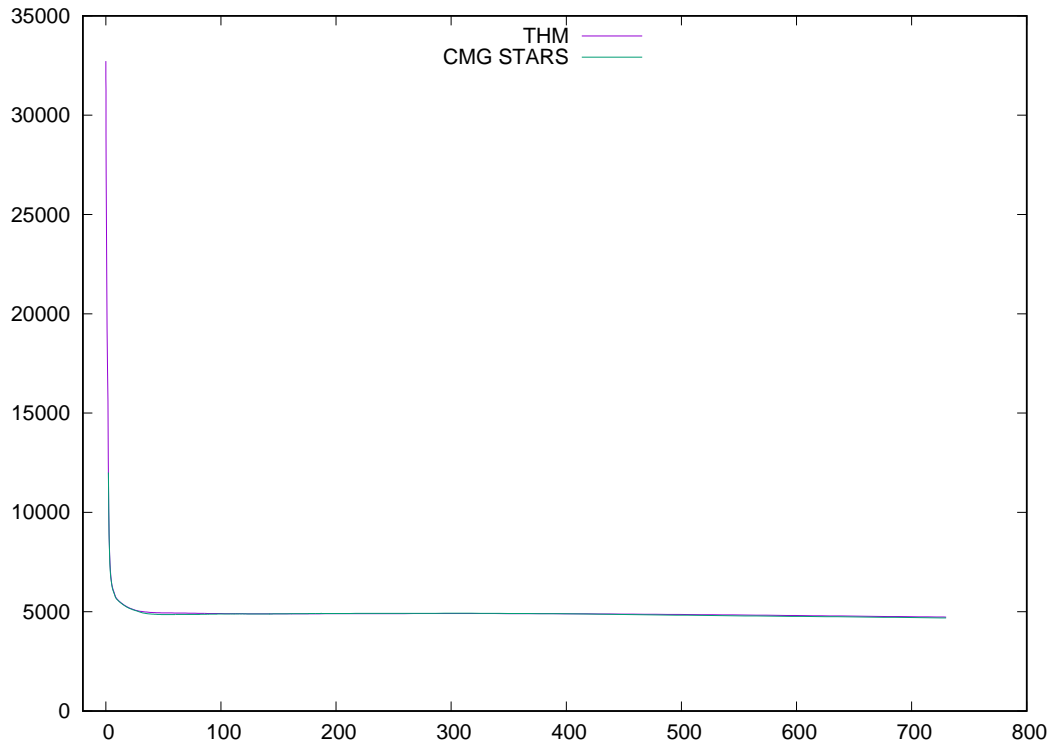


Figure 16: Example 2, light oil: injection well, bottom hole pressure (psi)

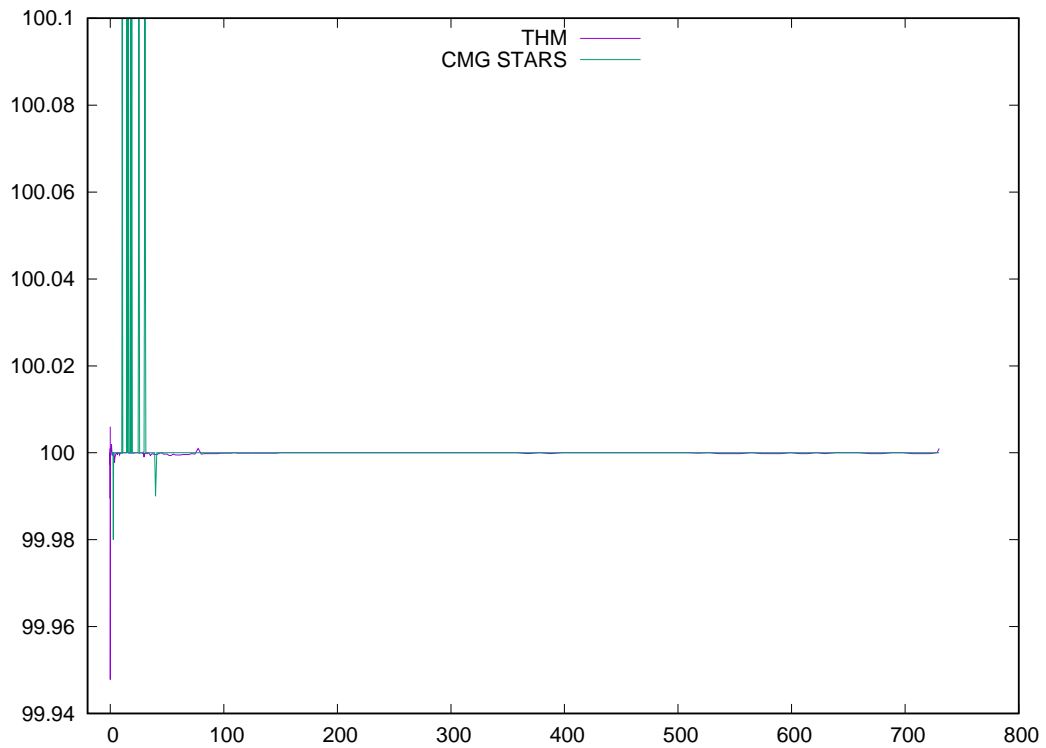


Figure 17: Example 2, light oil: injection well, water injection rate (bbl/day)

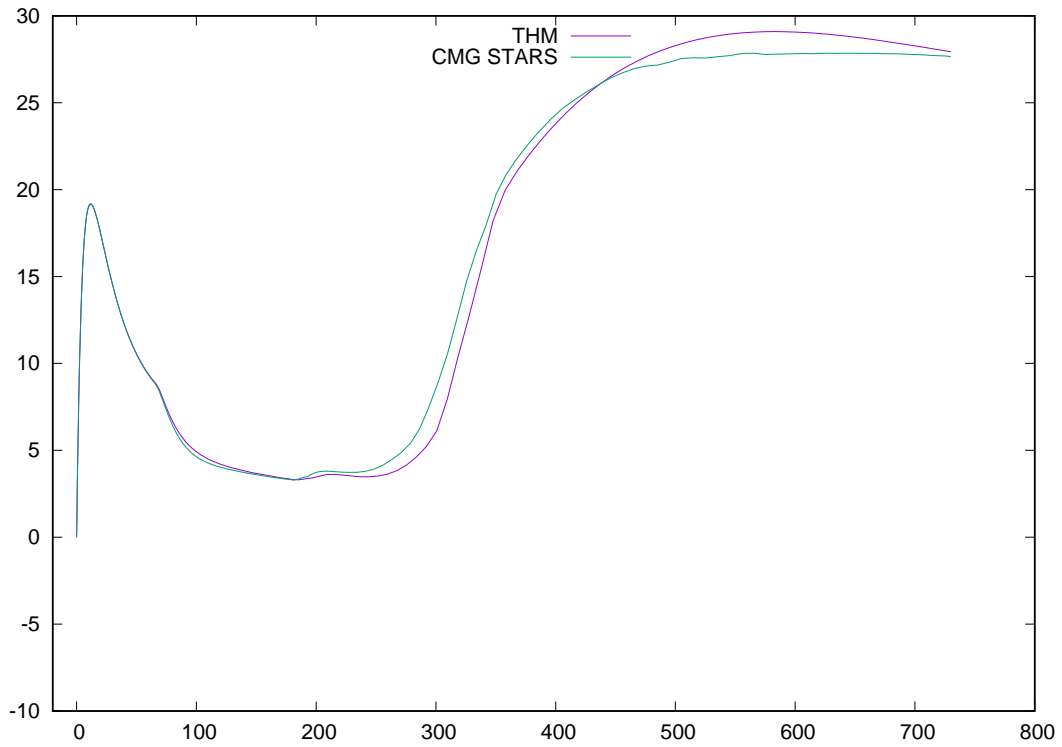


Figure 18: Example 2, light oil: water production rate (bbl/day), first production well

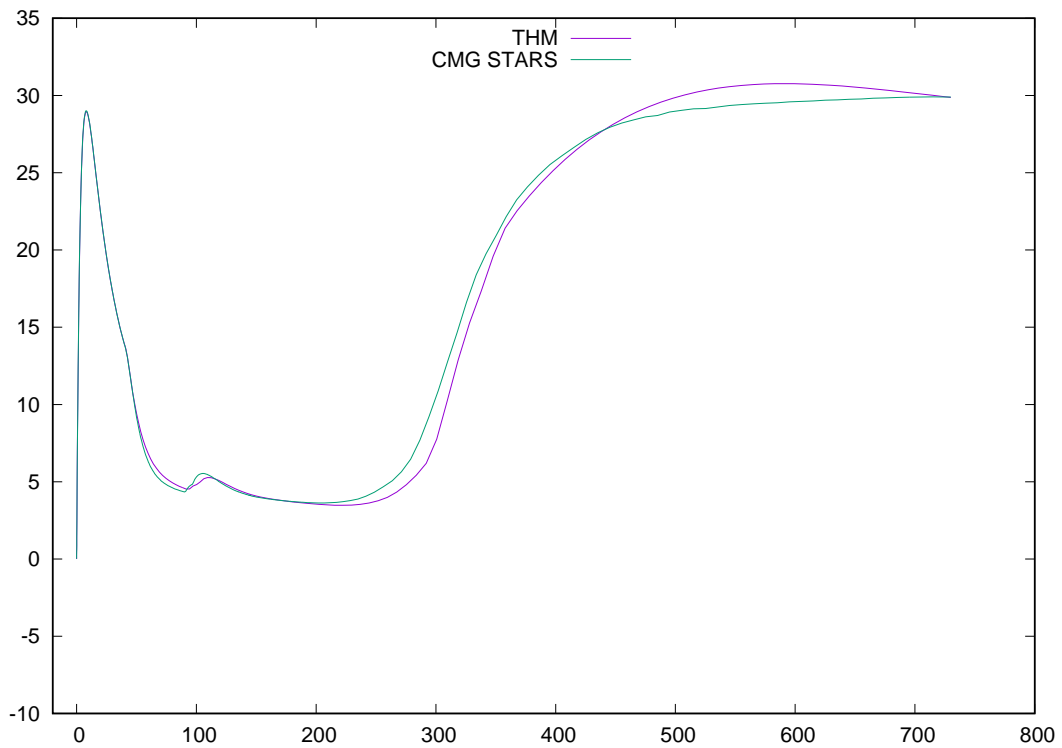


Figure 19: Example 2, light oil: water production rate (bbl/day), second production well

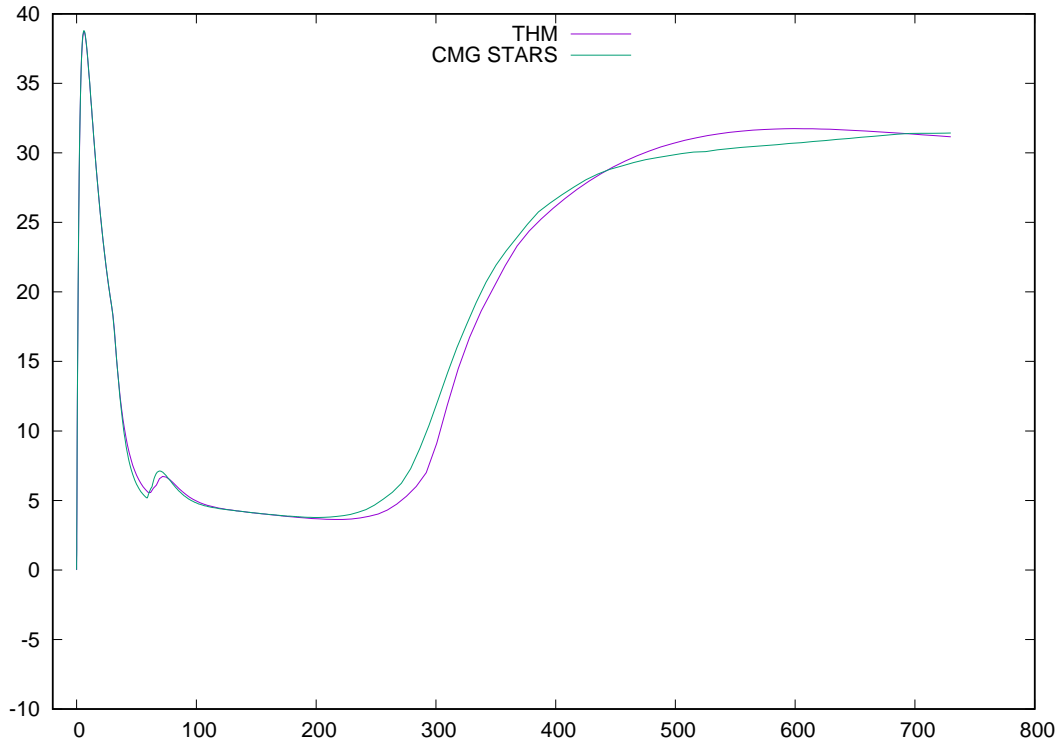


Figure 20: Example 2, light oil: water production rate (bbl/day), third production well

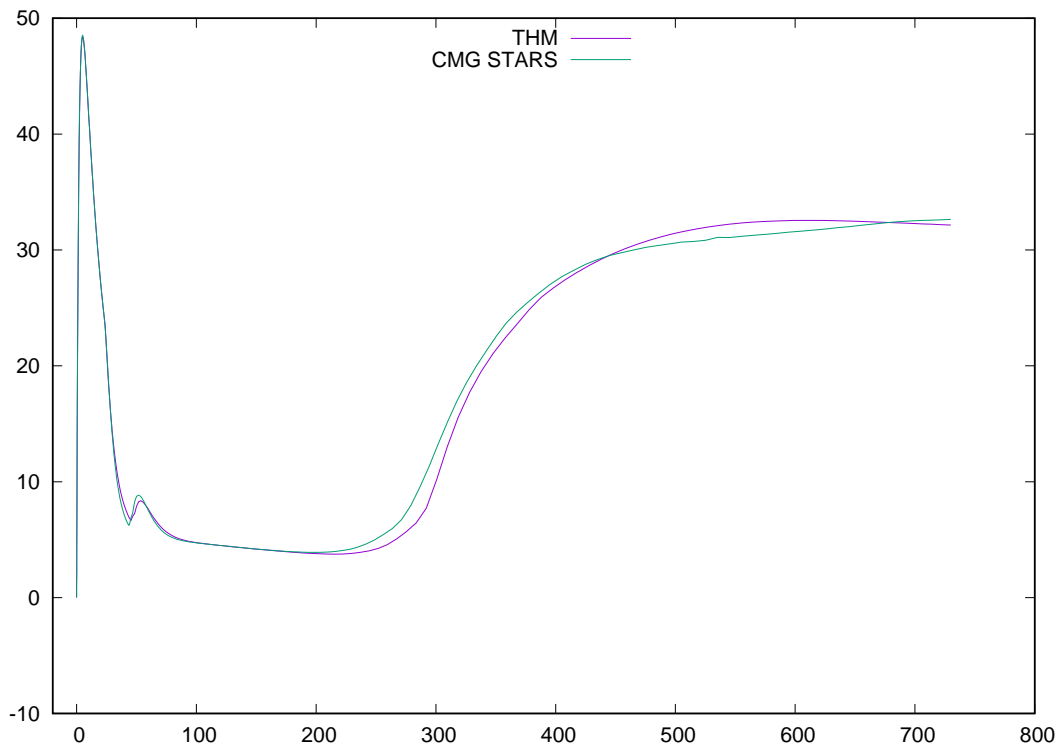


Figure 21: Example 2, light oil: water production rate (bbl/day), fourth production well

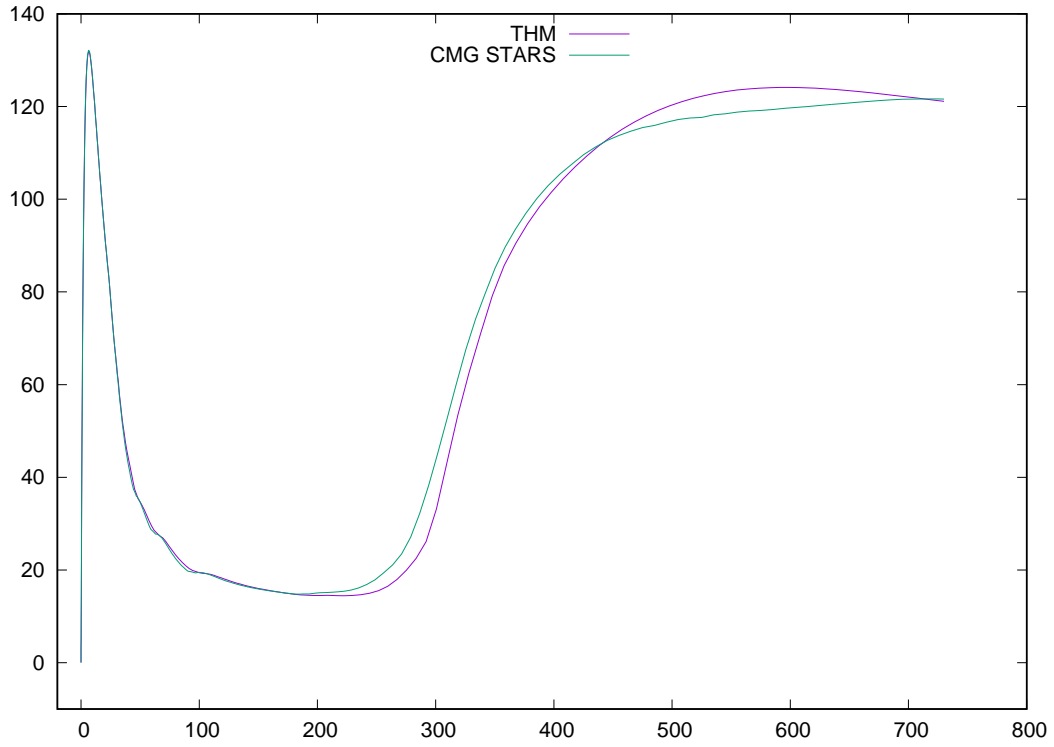


Figure 22: Example 2, light oil: total water production rate (bbl/day)

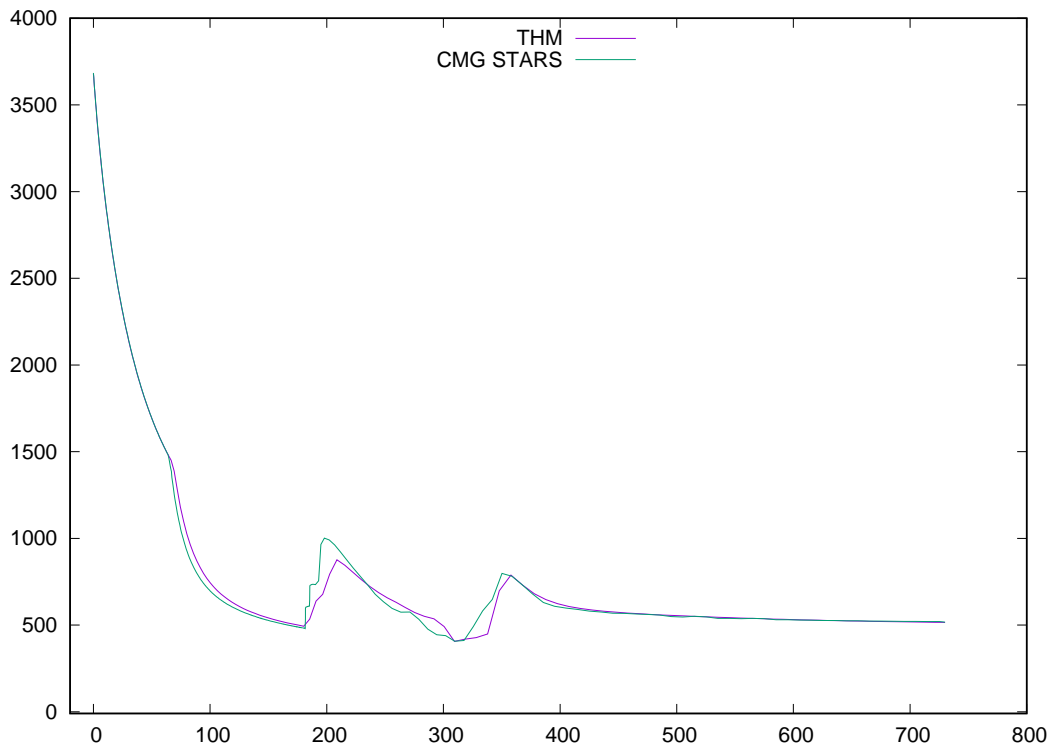


Figure 23: Example 2, light oil: gas production rate (ft^3/day), first production well

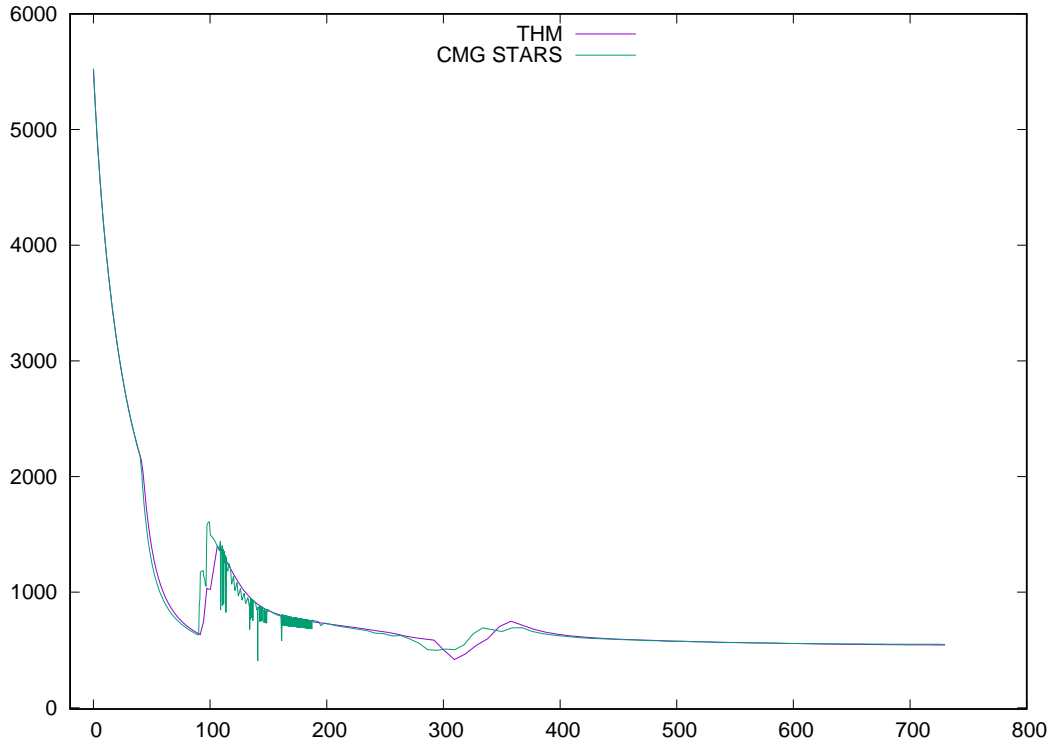


Figure 24: Example 2, light oil: gas production rate (ft^3/day), second production well

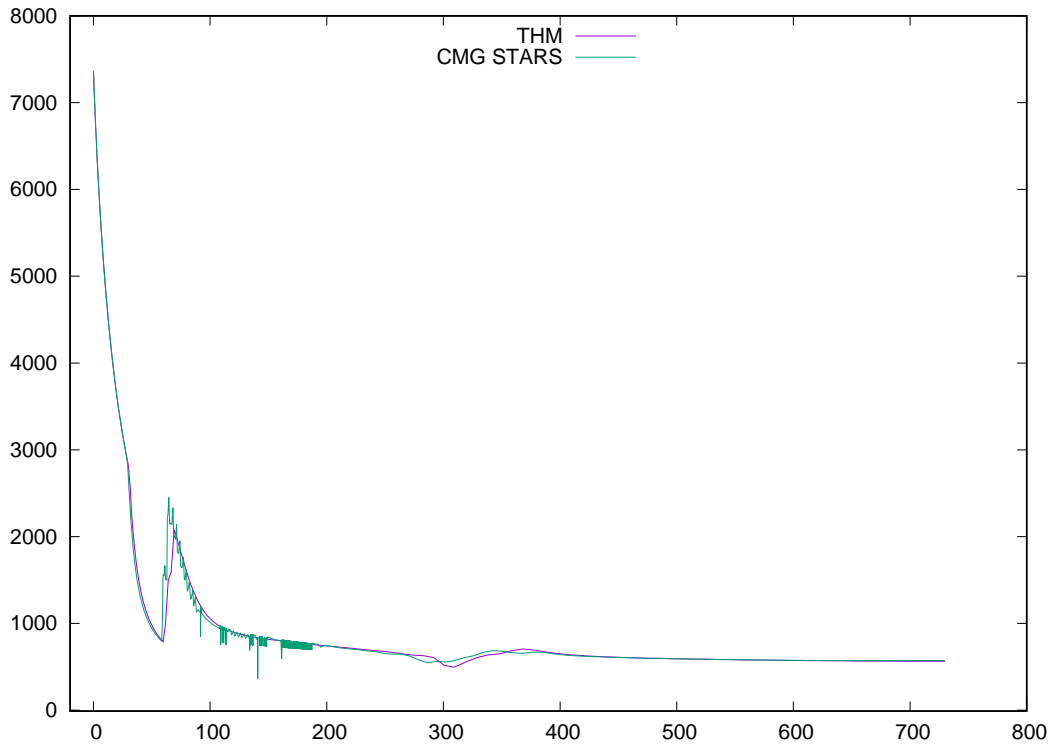


Figure 25: Example 2, light oil: gas production rate (ft^3/day), third production well

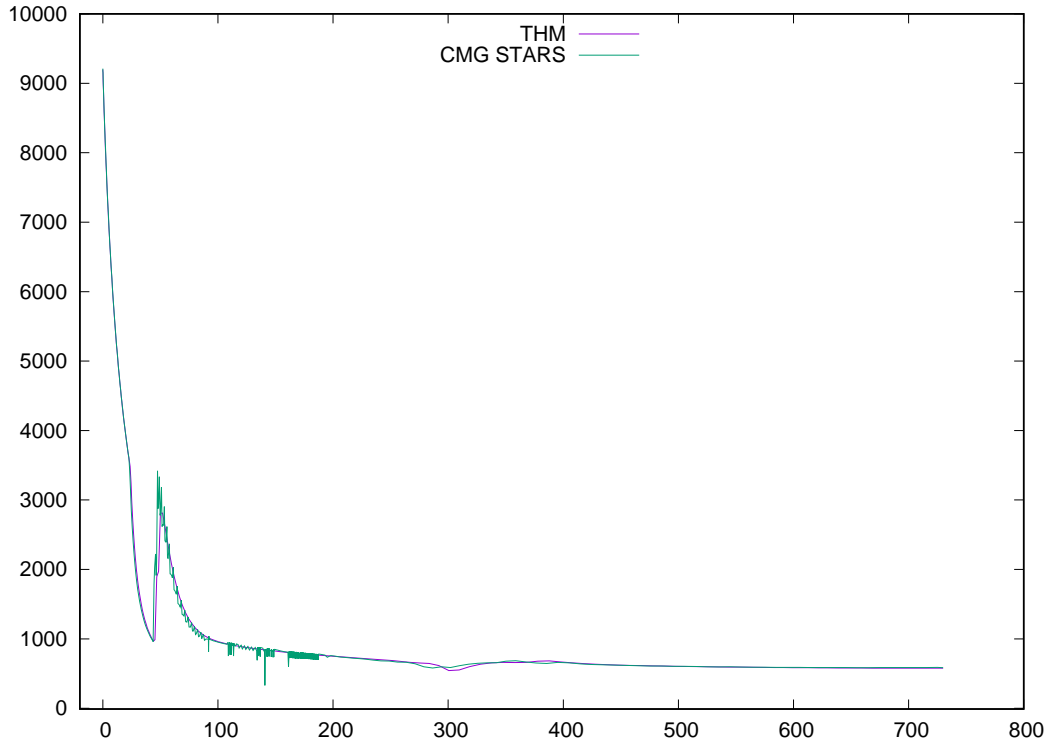


Figure 26: Example 2, light oil: gas production rate (ft^3/day), forth production well

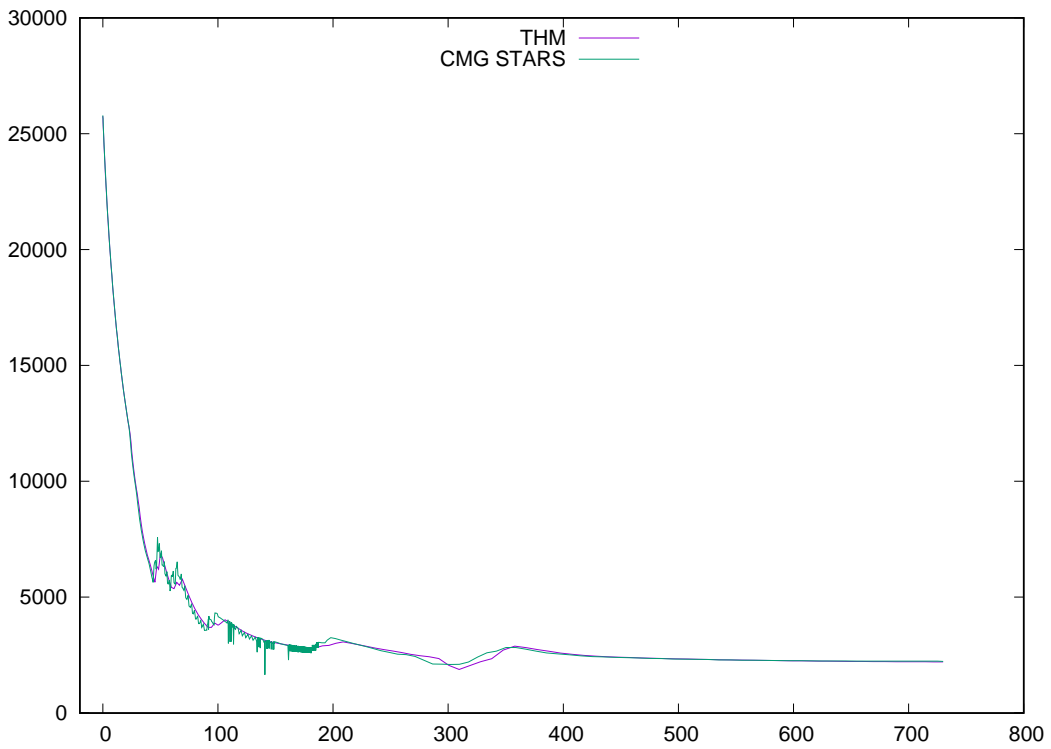


Figure 27: Example 2, light oil: total gas production rate (ft^3/day)

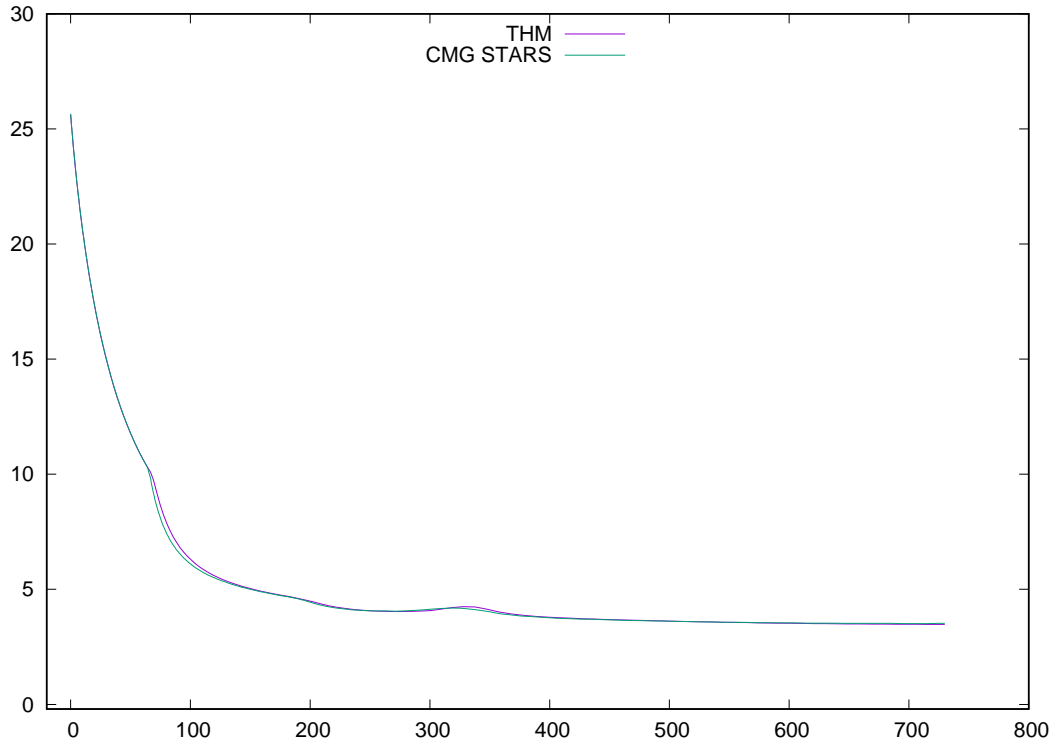


Figure 28: Example 2, light oil: oil production rate (bbl/day), first production well

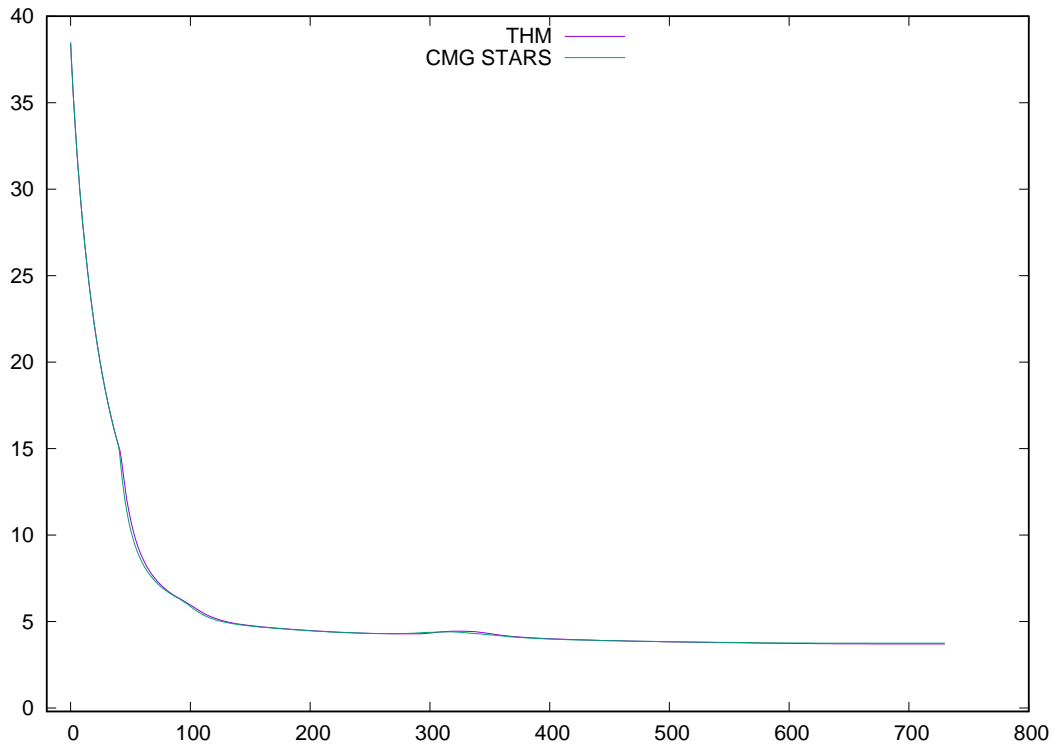


Figure 29: Example 2, light oil: oil production rate (bbl/day), second production well

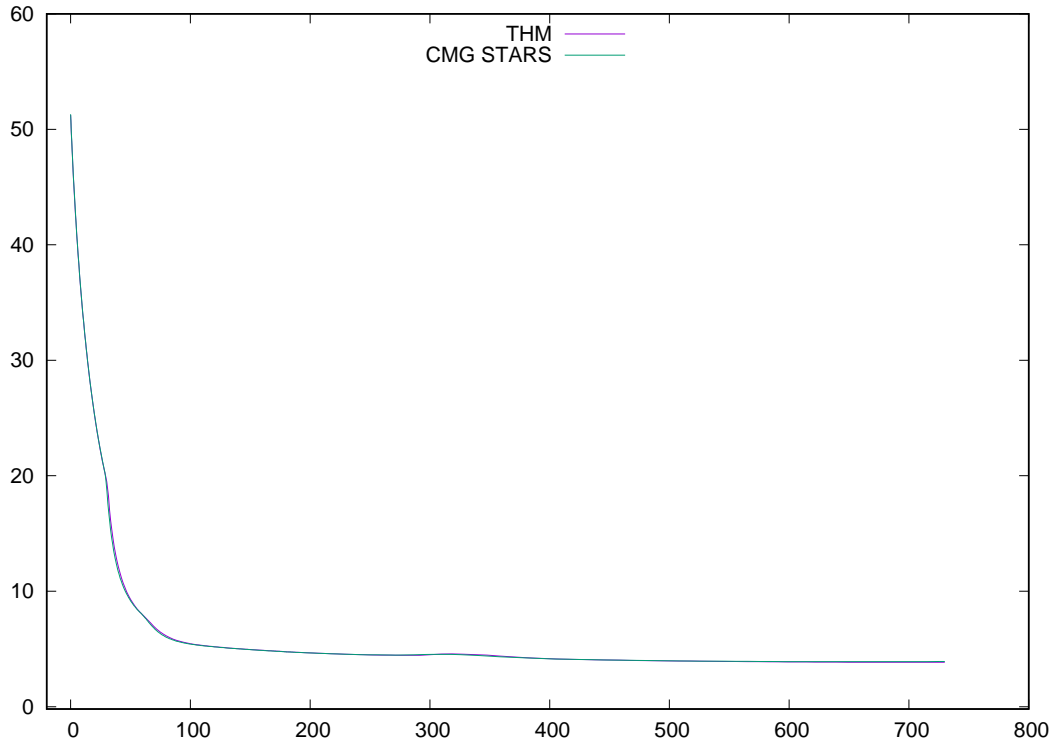


Figure 30: Example 2, light oil: oil production rate (bbl/day), third production well

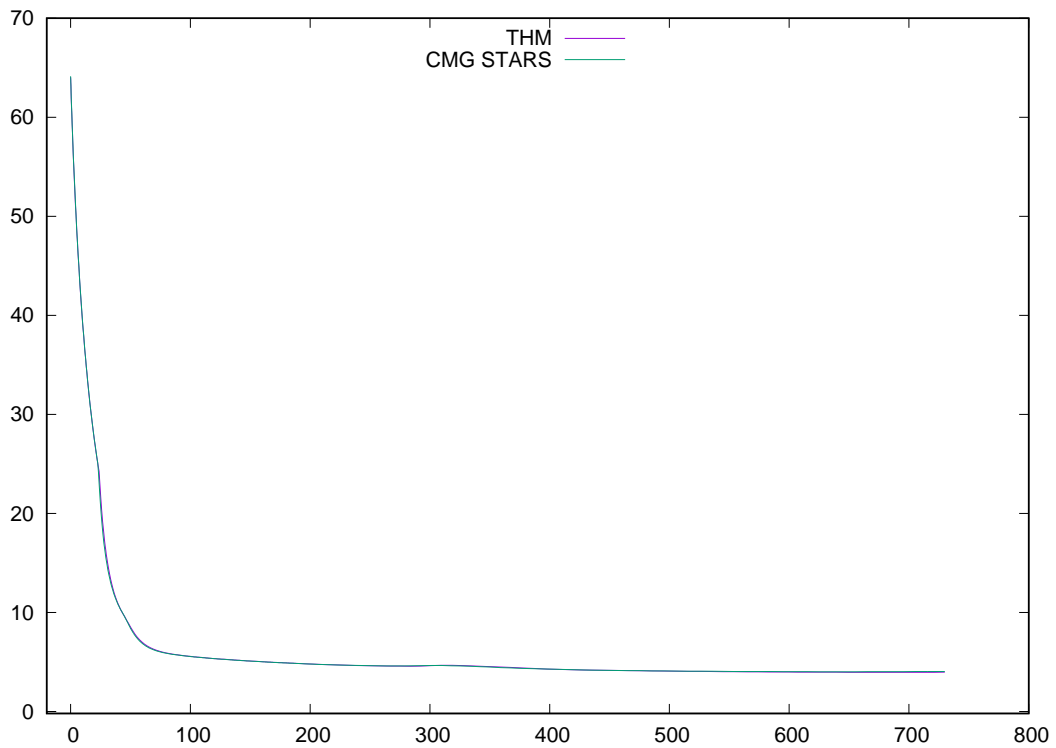


Figure 31: Example 2, light oil: oil production rate (bbl/day), fourth production well

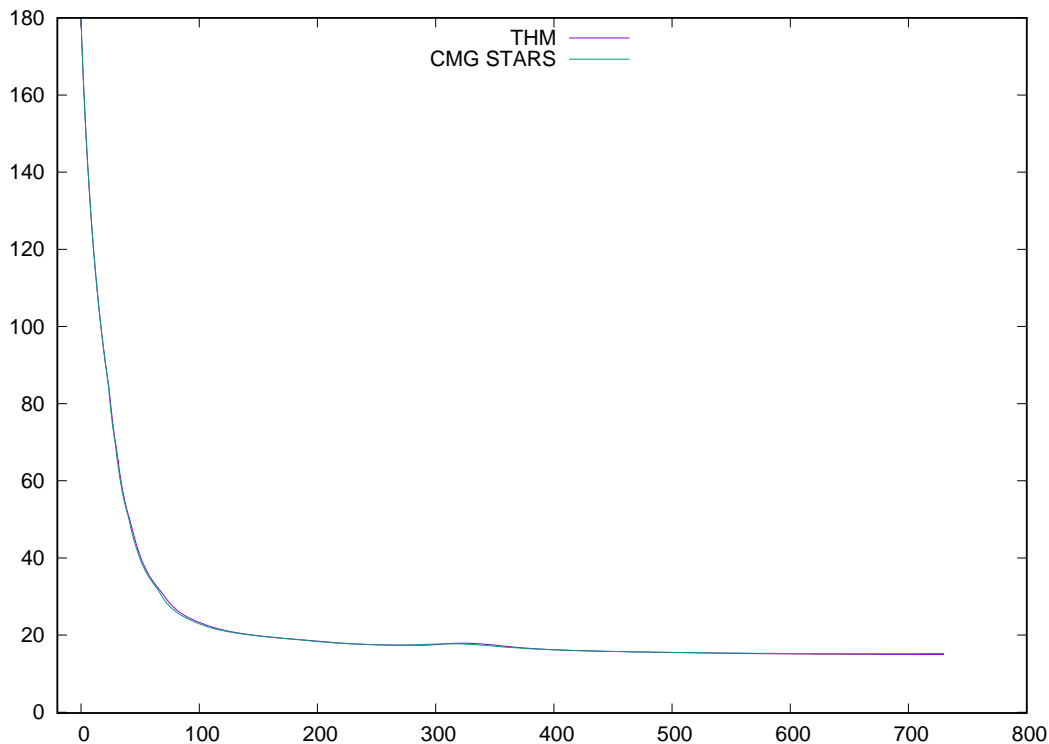


Figure 32: Example 2, light oil: total oil production rate (bbl/day)

4.1.3 Non-condensable Gas

Example 3 This model is similar as Example 2 except that two non-condensable gas (NCG) components are added. Data is provided in Table 8 and Table 8. It also has five vertical wells: one injection well in the center (5, 5), and four production wells in four corners, (1, 1), (1, 9), (9, 1) and (9, 9). The bottom hole pressure of the injection well, water rate and oil rate of each well are shown from Figure 33 to Figure 48. All results are compared with CMG STARS.

Initial condition	
$k_{x,y,z}$ (md)	313, 424, 535
ϕ	0.3
ϕ_c	5e-4
p (psi)	4000
T ($^{\circ}F$)	125
$S_{w,o,g}$	0.4, 0.5, 0.1
x	0.6, 0.4
y	4.73644e-4, 0, 0.486126, 0.2, 0.3134

Table 8: Input data for Example 3

Figure 33 is the bottom hole pressure of the injection well. Figure 34 is the water production rate of the first production well. Figure 35 is the water production rate of the second production well. Figure 36 is the water production rate of the third production well. Figure 37 is the water production rate of the fourth production well. Figure 38 is the total water production rate of all production wells. Figure 39 is the gas production rate of the first production well. Figure 40 is the gas production rate of the second production well. Figure 41 is the gas production rate of the third production well. Figure 42 is the gas production rate of the fourth production well. Figure 43 is the total gas production rate of all production wells. Figure 44 is the oil production rate of the first production well. Figure 45 is the oil production rate of the second production well. Figure 46 is the oil production rate of the third production well. Figure 47 is the oil production rate of the fourth production well.

Properties	N2	Isert
M (lb/lbmole)	28	40.8
p_{crit} (psi)	730	500
T_{crit} ($^{\circ}F$)	-181	-232
$cpg1$ (Btu/ $^{\circ}F \cdot lbmol$)	6.713	7.44
$cpg2$ (Btu/ $^{\circ}F \cdot lbmol$)	-4.883e-7	-0.0018
$cpg3$ (Btu/ $^{\circ}F \cdot lbmol$)	1.287e-6	1.975e-6
$cpg4$ (Btu/ $^{\circ}F \cdot lbmol$)	-4.36e-10	-4.78e-10
avg (cp/ $^{\circ}F$)	2.1960e-4	2.1267e-4
bvg	0.721	0.702

Table 9: Input data for Example 3

Figure 48 is the total oil production rate of all production wells. All figures show that our results match CMG STARS very well, which confirms our methods and implementation are correct.

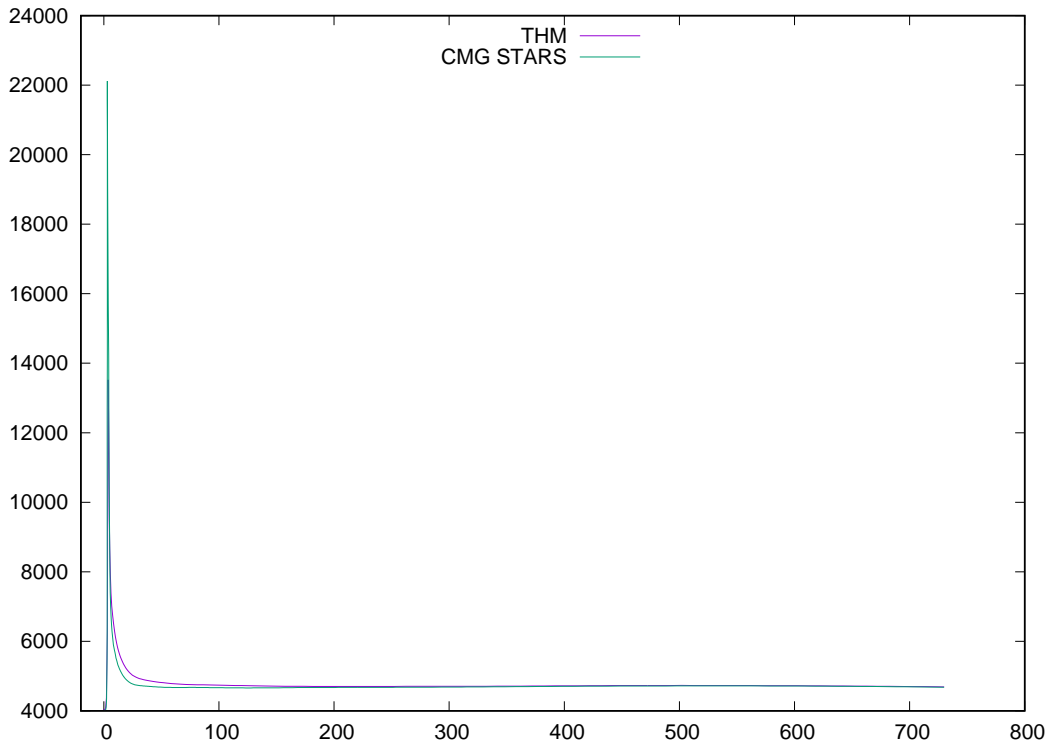


Figure 33: Example 3, NCG: injection well, bottom hole pressure (psi)

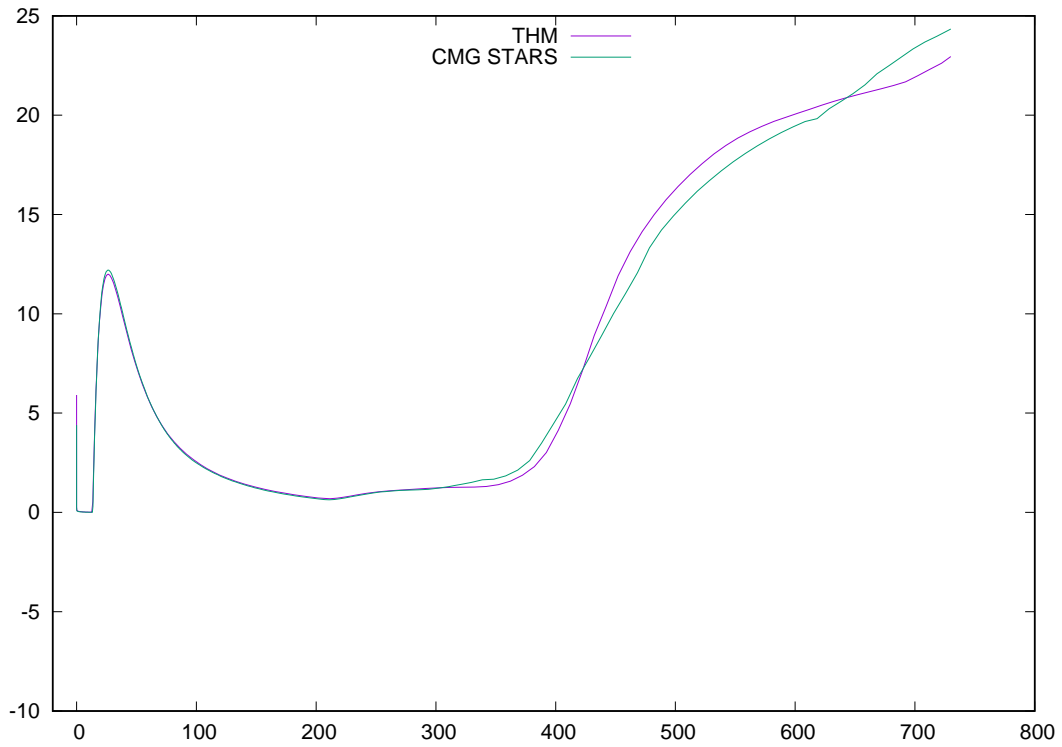


Figure 34: Example 3, NCG: water production rate (bbl/day), first production well

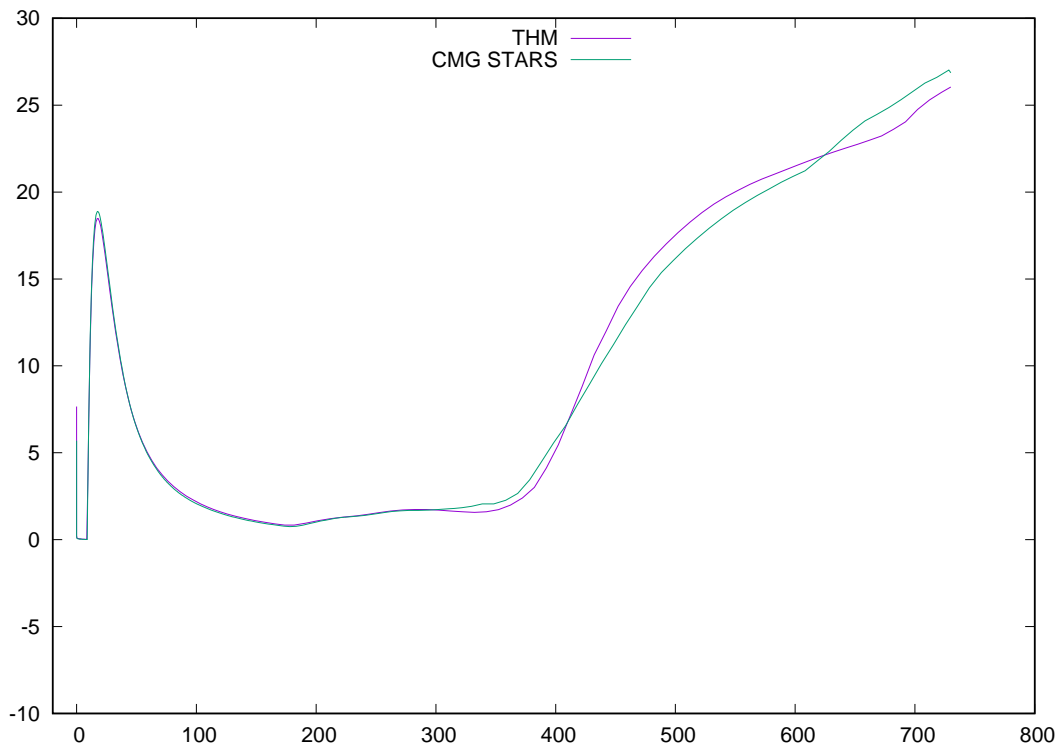


Figure 35: Example 3, NCG: water production rate (bbl/day), second production well

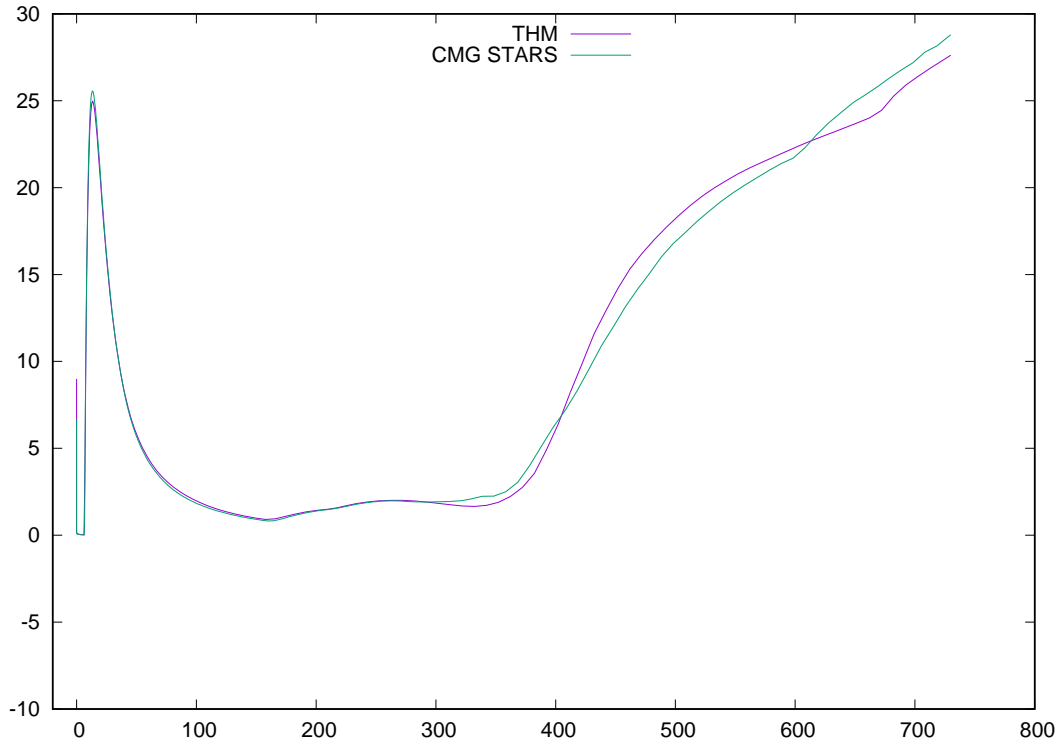


Figure 36: Example 3, NCG: water production rate (bbl/day), third production well

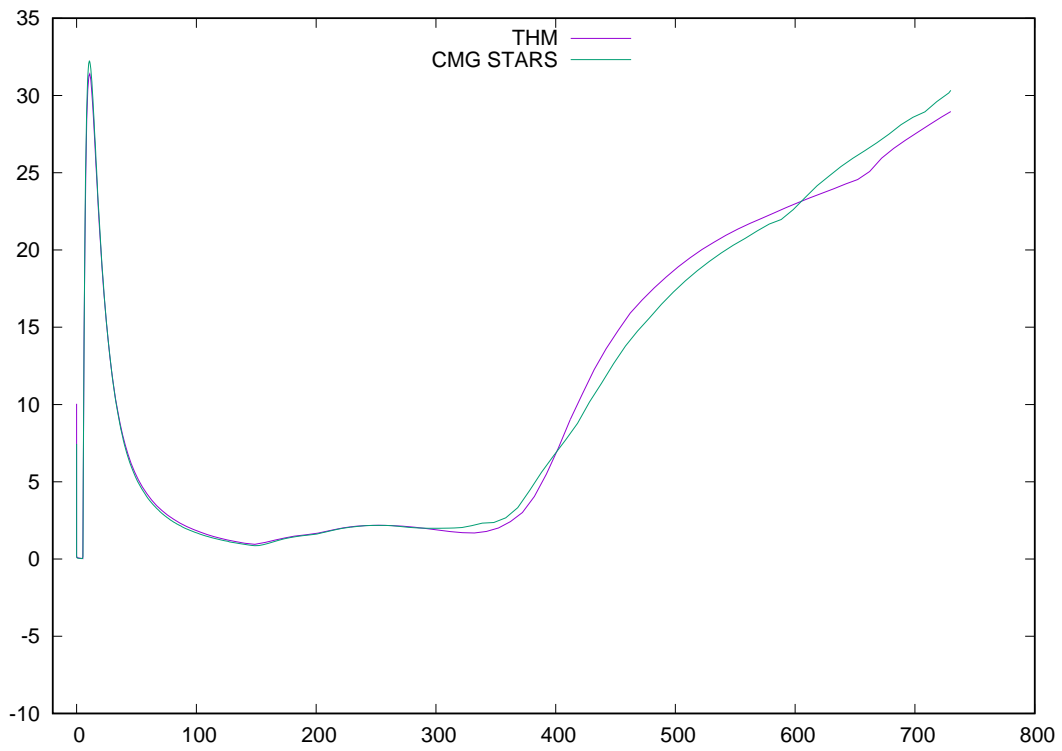


Figure 37: Example 3, NCG: water production rate (bbl/day), fourth production well

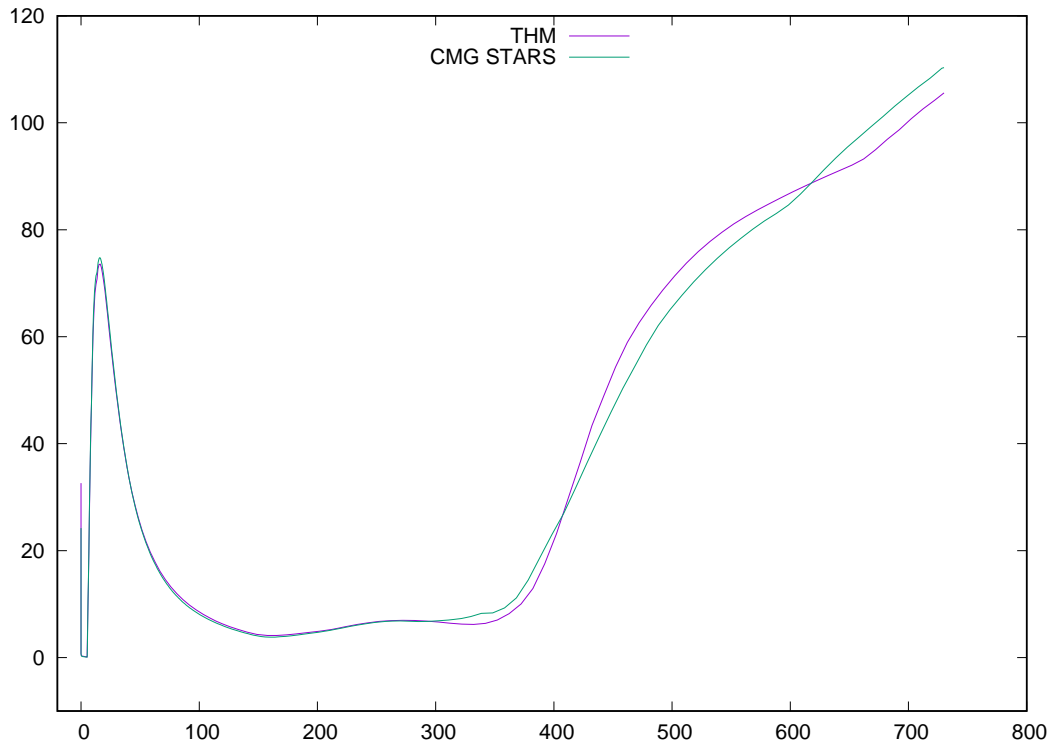


Figure 38: Example 3, NCG: total water production rate (bbl/day)

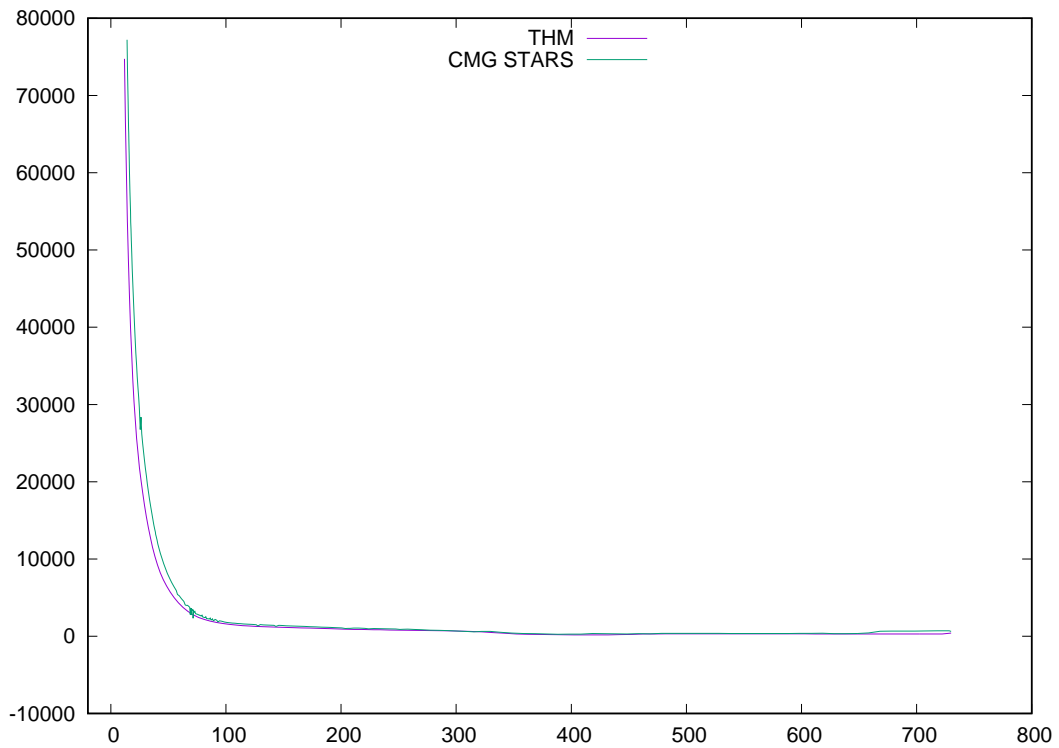


Figure 39: Example 3, NCG: gas production rate (ft^3/day), first production well

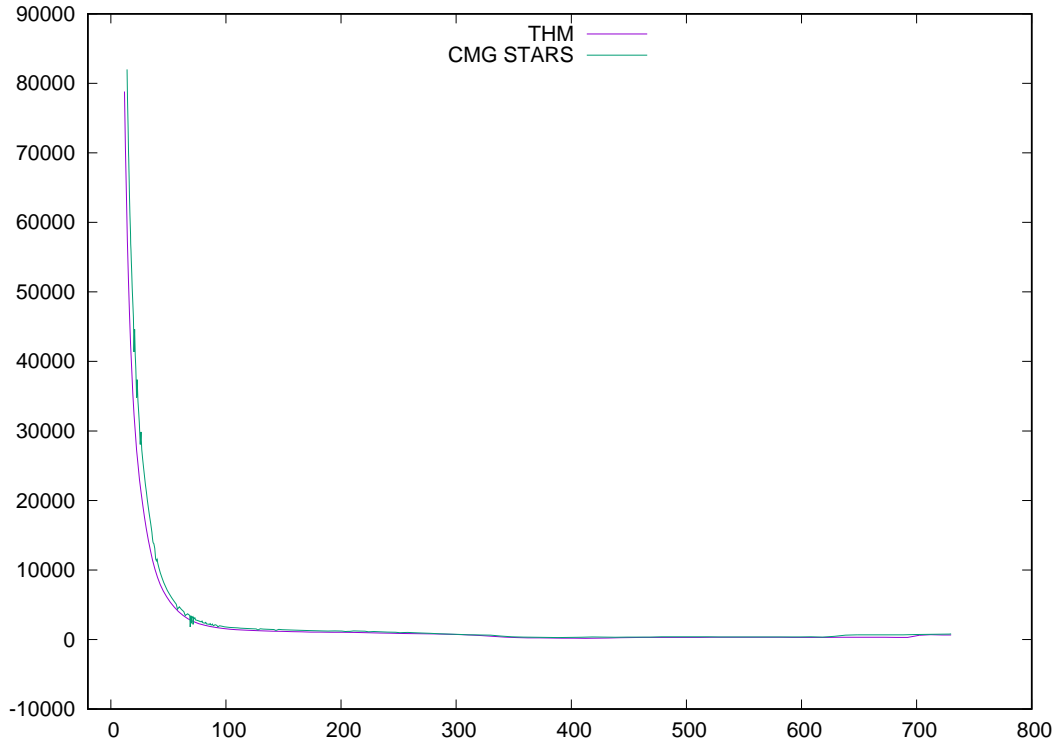


Figure 40: Example 3, NCG: gas production rate (ft^3/day), second production well

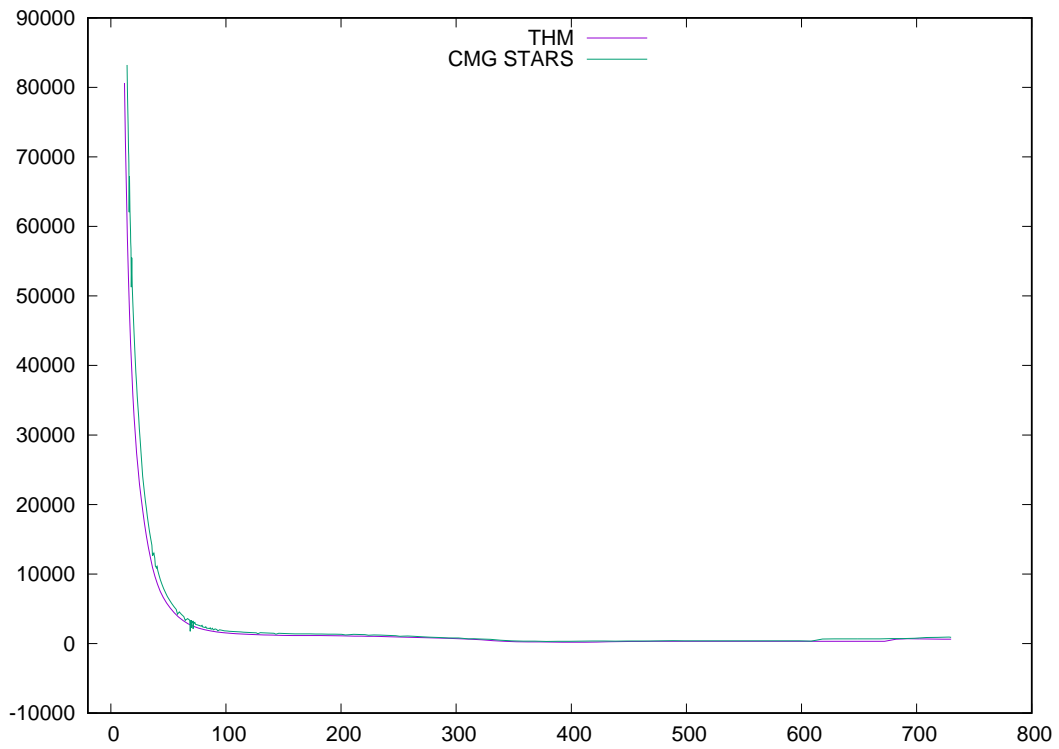


Figure 41: Example 3, NCG: gas production rate (ft^3/day), third production well

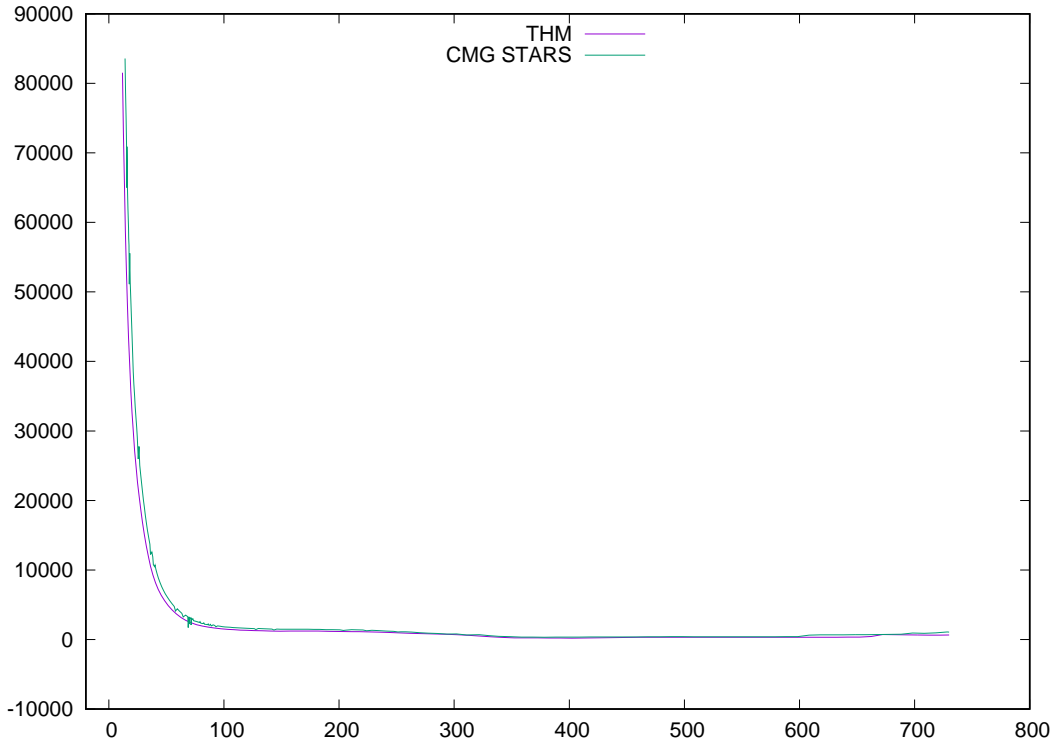


Figure 42: Example 3, NCG: gas production rate (ft^3/day), forth production well

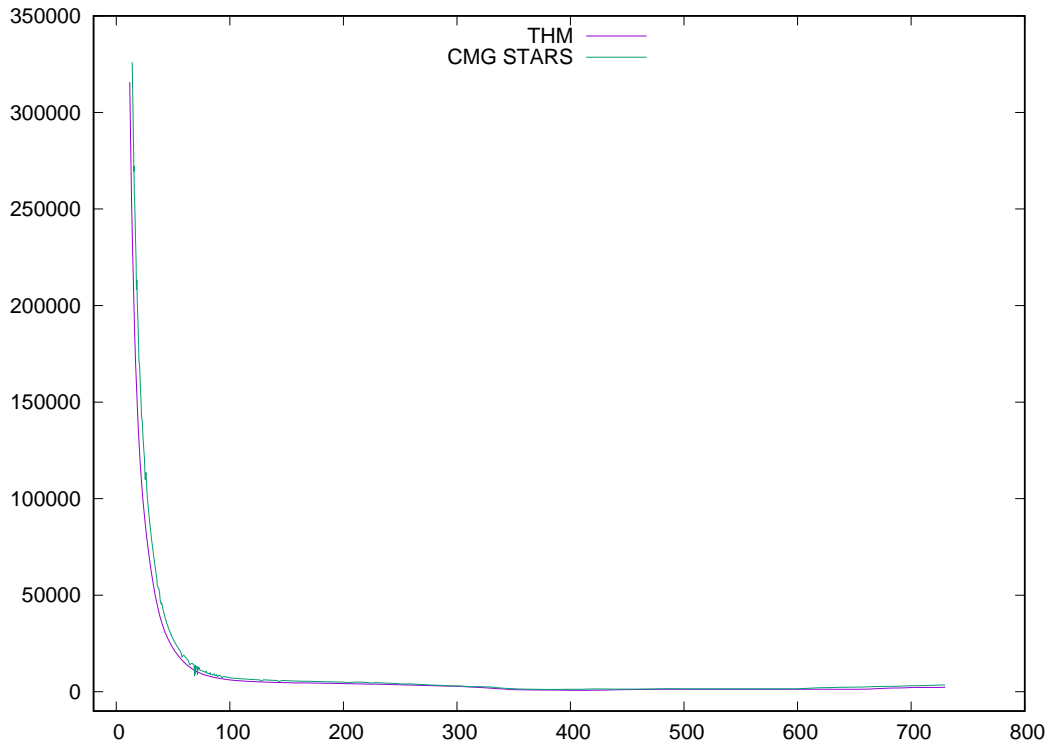


Figure 43: Example 3, NCG: total gas production rate (ft^3/day)

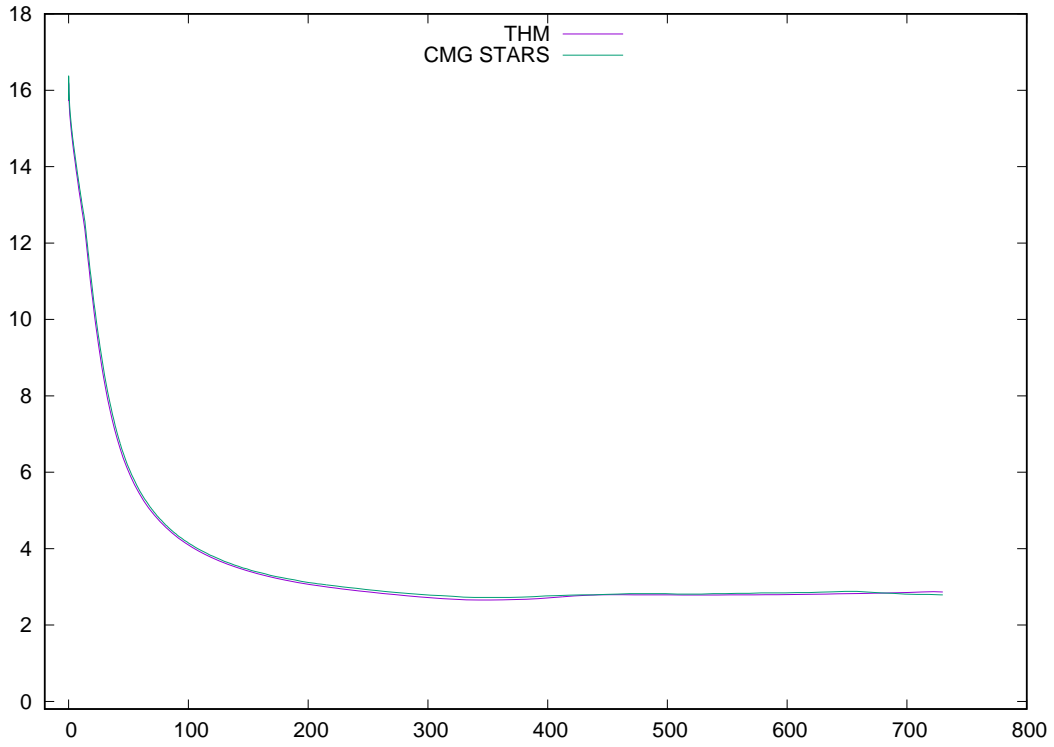


Figure 44: Example 3, NCG: oil production rate (bbl/day), first production well

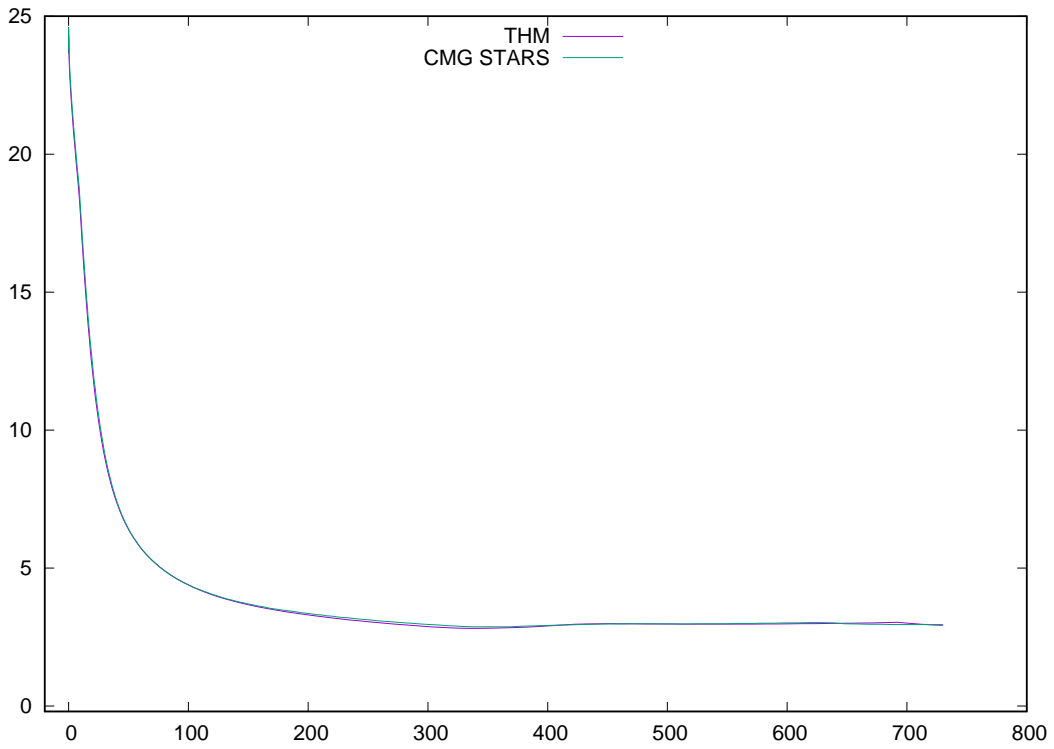


Figure 45: Example 3, NCG: oil production rate (bbl/day), second production well

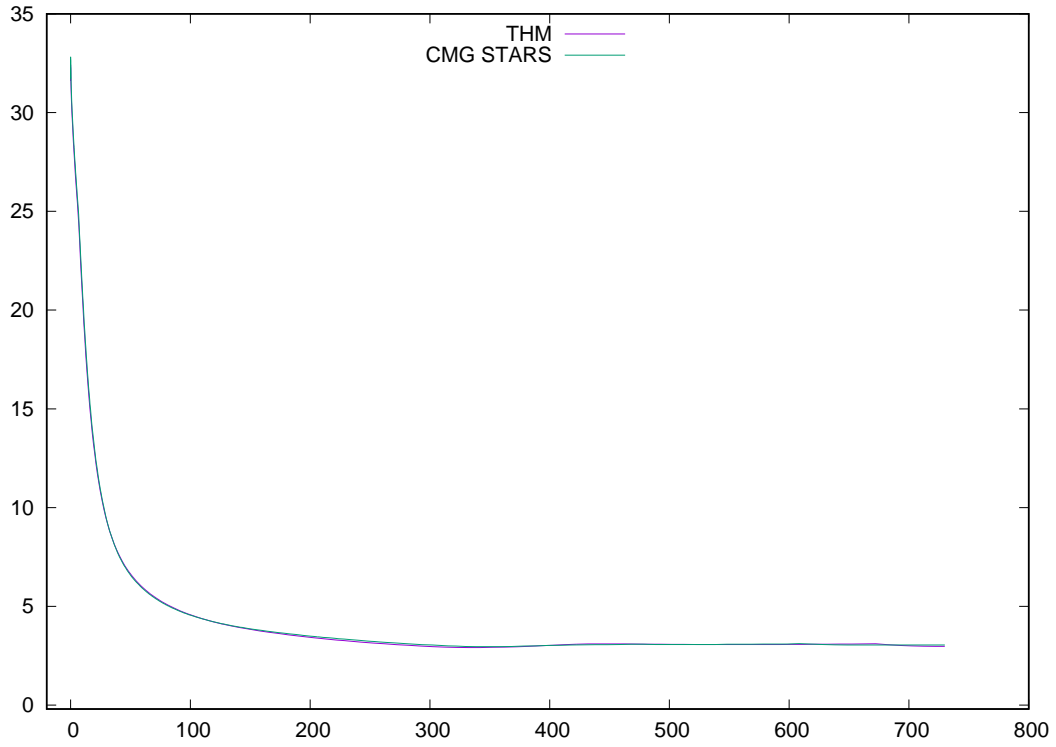


Figure 46: Example 3, NCG: oil production rate (bbl/day), third production well

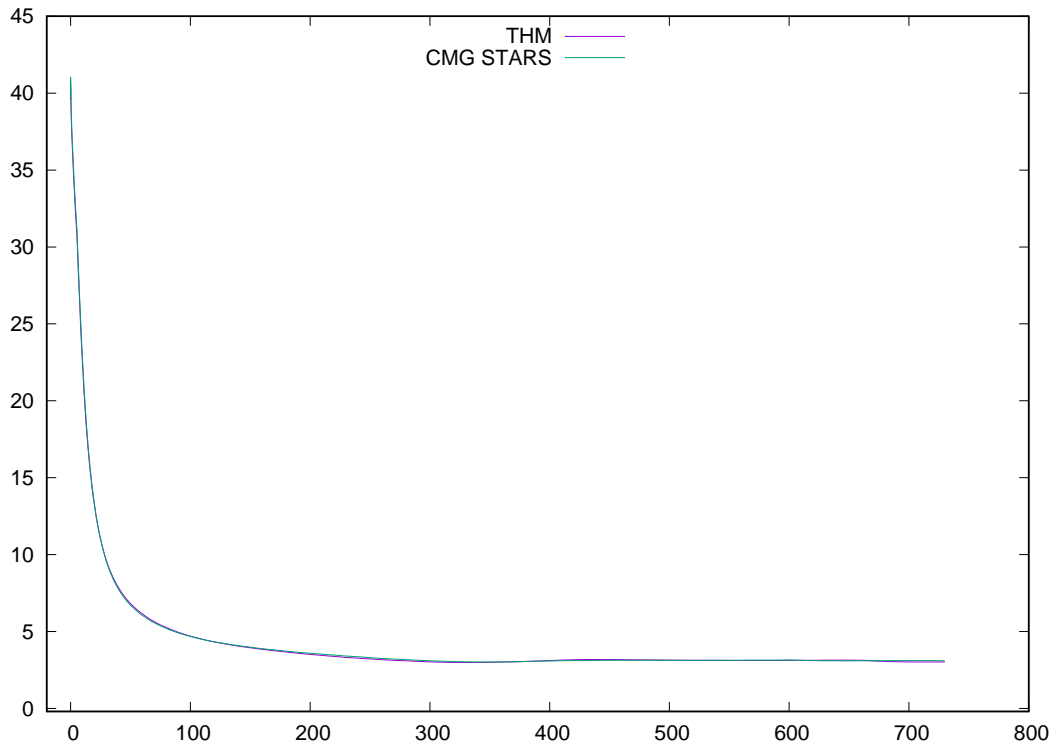


Figure 47: Example 3, NCG: oil production rate (bbl/day), fourth production well

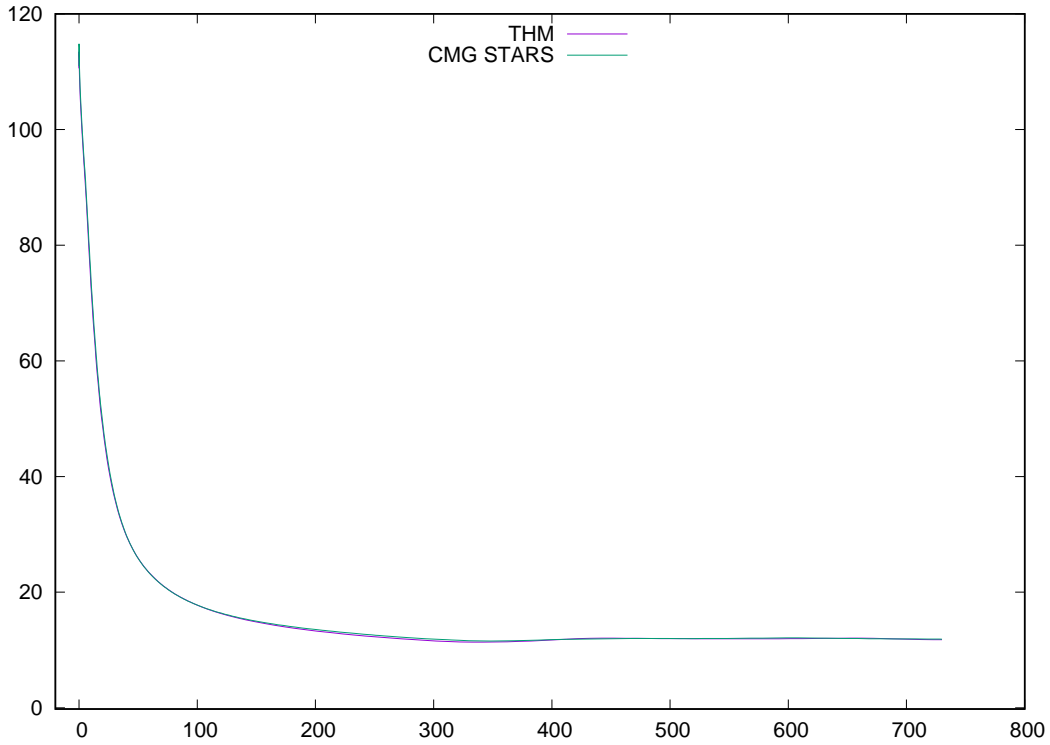


Figure 48: Example 3, NCG: total oil production rate (bbl/day)

4.2 Well Controls

The water (steam) injection rate, water production and oil production rates, bottom hole pressure for each well are reported. All rates are surface rates, and flash calculations are required to convert reservoir rates to surface rates. The injection rate is measured as cold water equivalent. As we mentioned, the well modeling is the most complicated, and we will change well operation constraints to test our simulator.

If there is no special statement, the non-linear method is the standard Newton method with a tolerance $1e-6$ and maximal iterations of 10, the linear solver is BICGSTAB with a tolerance $1e-4$ and maximal iterations of 100, and the preconditioner is CPR-FPF method. All wells use implicit numerical methods, though the explicit method has been implemented.

4.2.1 Fixed Bottom Hole Pressure

Example 4 The injection well operates at 1500 psi. The steam quality is 0, and its temperature is 450 F. Two production wells operates are 17 psi. The simulation period is 365 days. Figure 49, 50, and 51 show the water injection rate, total water production and total oil production. The rates are surface rate. All results are compared with CMG STARS. From these figures, we can see that our results match CMG STARS.

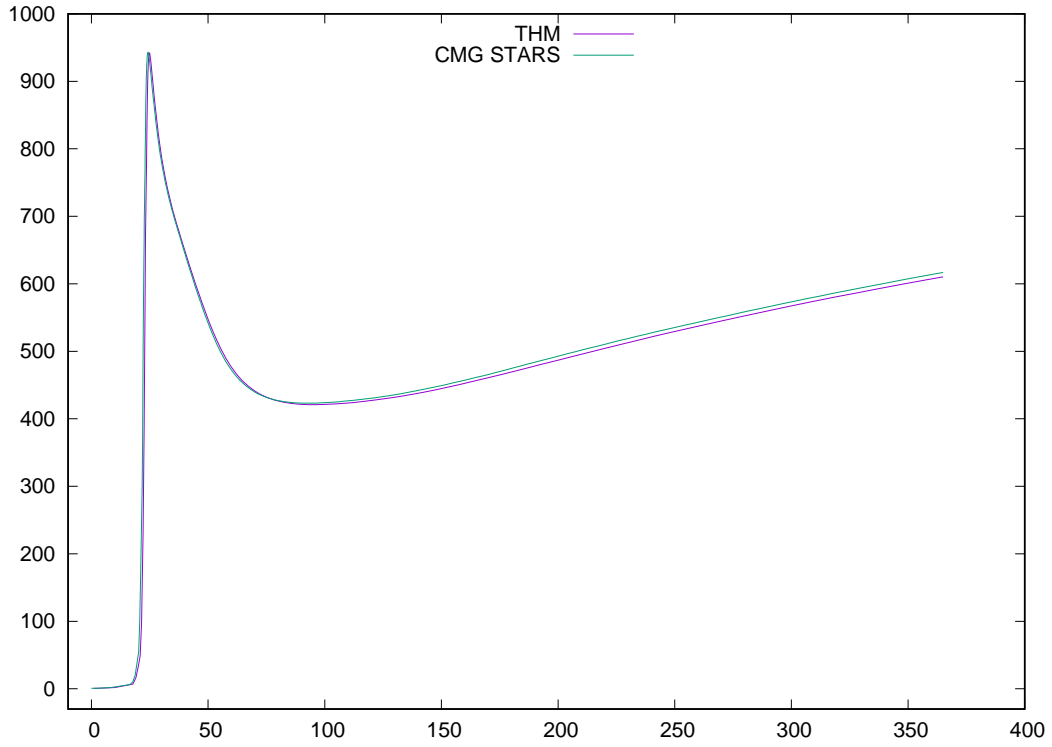


Figure 49: Example 4, fixed bottom hole pressure: water injection rate (bbl/day)

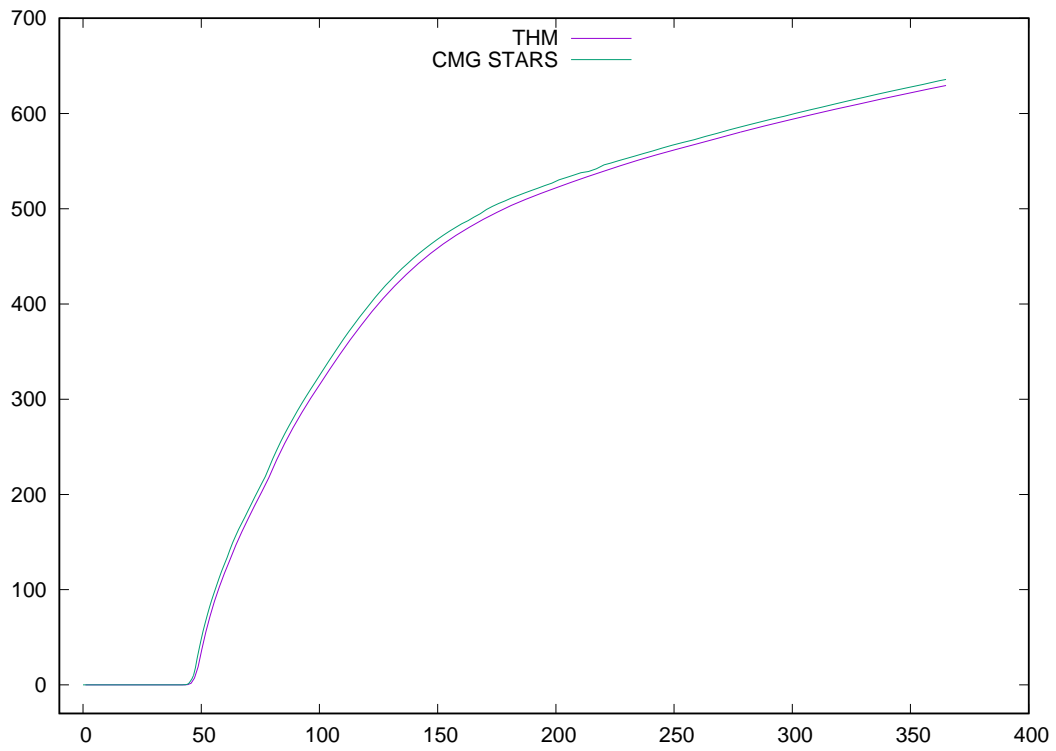


Figure 50: Example 4, fixed bottom hole pressure: water production rate (bbl/day)

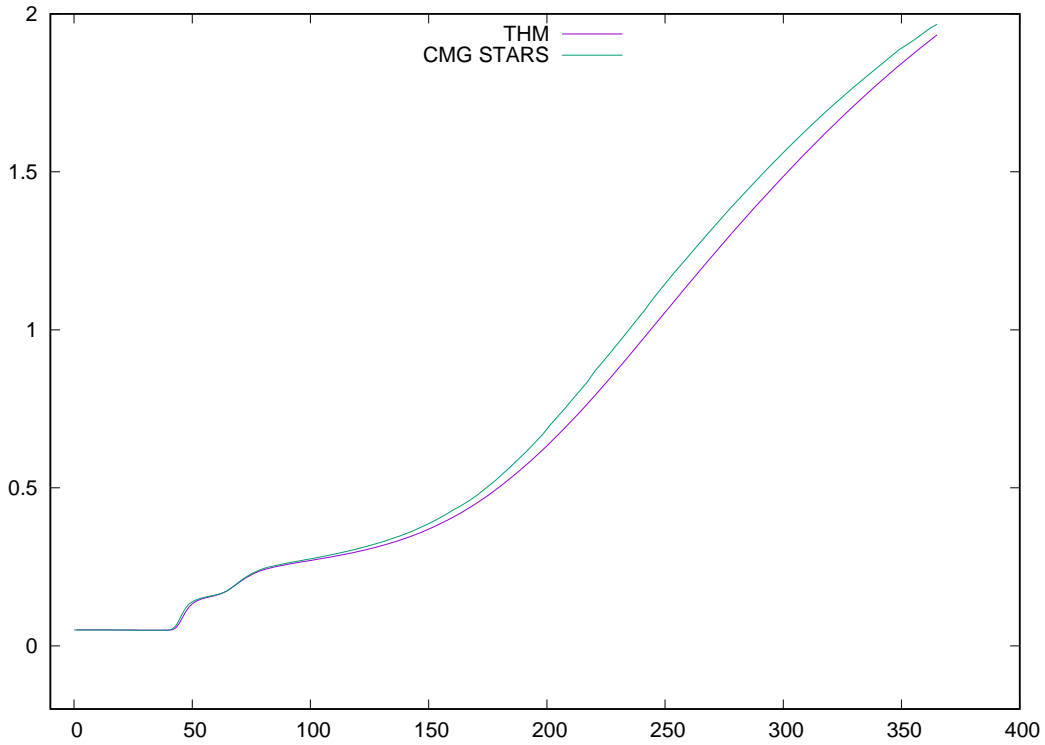


Figure 51: Example 4, fixed bottom hole pressure: oil production rate (bbl/day)

4.2.2 Fixed Rate

Example 5 The injection well operates at 300 bbl/day, and the production wells operates at 17 psi. The simulation period is 365 days. Figure 52, 53, and 54 are bottom hole pressure for injection well, total water production and total oil production. All results are compared with CMG STARS.

When fixed rate constraint is applied to a well, its rate is known, but its bottom hole pressure is unknown, which should be obtained by Newton methods. Figure 52 represents the bottom hole pressure of the injection well, from which we can see that our results match CMG STARS exactly. It means the methods and the implementation are correct. Figure 53 is the total water production rate, which also match CMG STARS exactly. Figure 54 is the total oil production rate (bbl/day). The results match CMG STARS exactly in the first 100 days, and after that, there is slight difference. The reason is that each simulator has its own numerical settings and automatical numerical tunings. For example, the density, bottom hole pressure update and mobility for wells in CMG STARS have many parameters to control, and CMG has automatical bottom hole pressure update algorithms depending on time step and pressure changes, whose details are unknown to us.

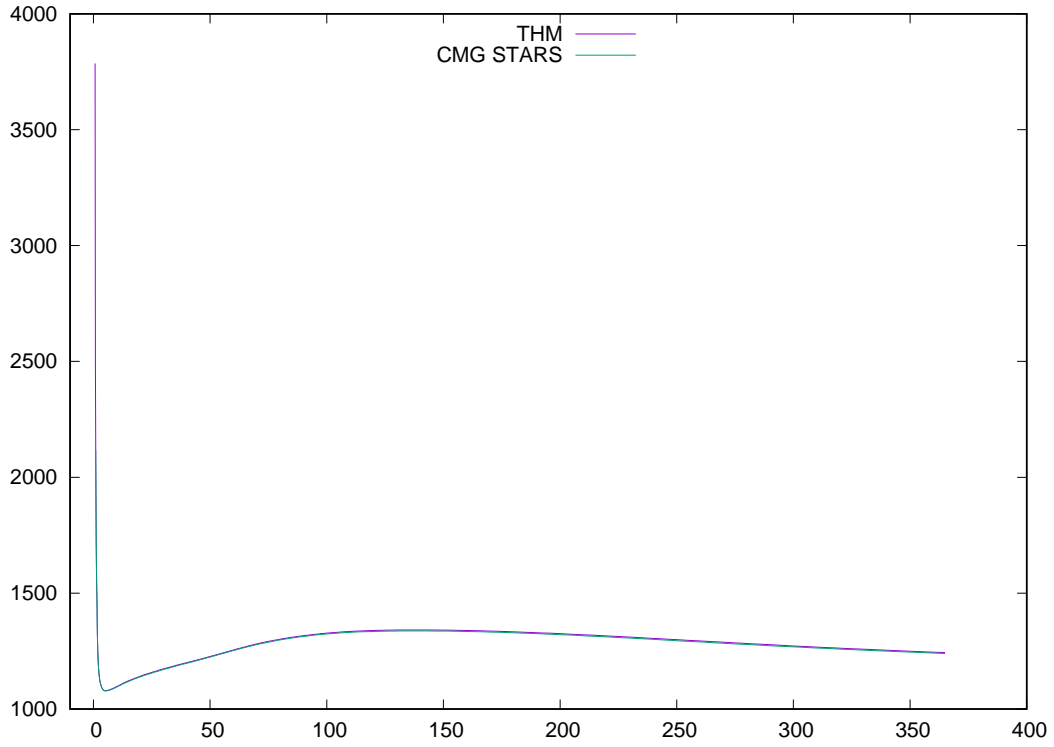


Figure 52: Example 5, fixed rate: injection well, bottom hole pressure (psi)

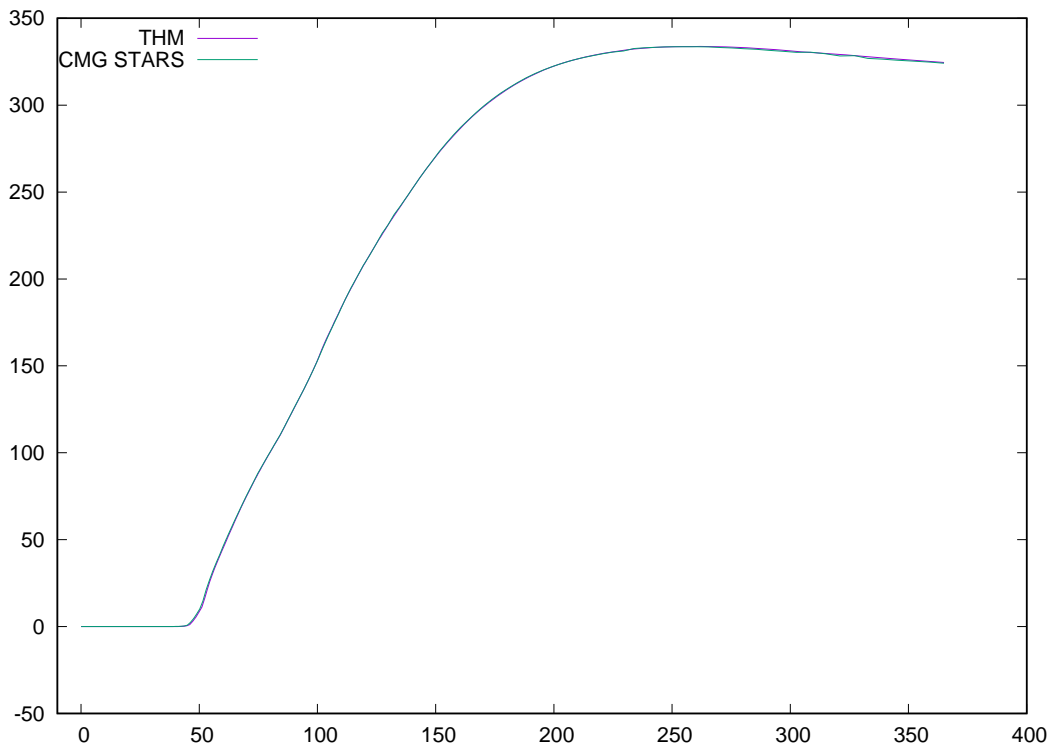


Figure 53: Example 5, fixed rate: water production rate (bbl/day)

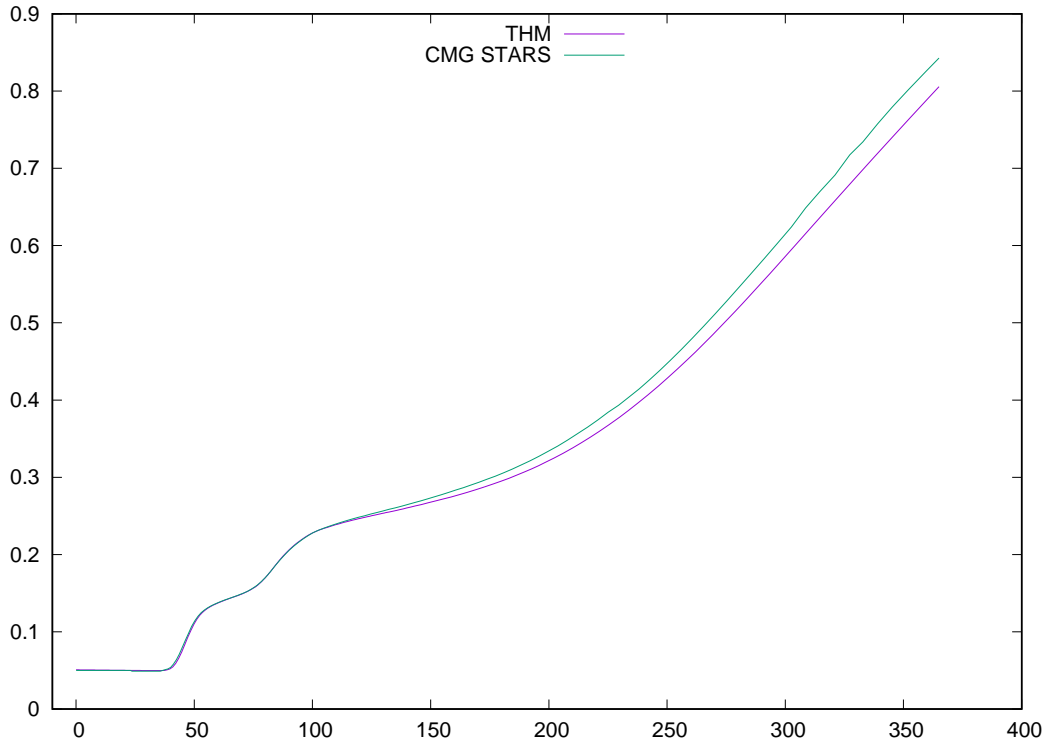


Figure 54: Example 5, fixed rate: oil production rate (bbl/day)

4.2.3 Rate and Pressure Constraints

A well may have many operation constraints, such as maximal injection rate with maximal bottom hole pressure for injection well, maximal oil production rate with minimal bottom hole pressure for production well, and maximal liquid rate with minimal bottom hole pressure for production well.

Example 6 The injection well has a maximal injection rate of 200 bbl/day and a maximal bottom hole pressure of 1500 psi. The steam has a steam quality of 0.3 and temperature of 450 F. The first production well has a maximal liquid rate of 0.5 bbl/day and a minimal bottom hole pressure of 17 psi. The second production well has a maximal oil rate of 0.4 bbl/day and a minimal bottom hole pressure of 17 psi. The simulation period is 365 days. The bottom hole pressures for each well, water rates and oil rates for each well are presented from Figure 55 to Figure 65. All results are compared with CMG STARS.

Figure 55, 58 and 59 show the bottom hole pressure for injection well and production wells. The results for production wells match well. Our Newton method shows good convergence but CMG STARS shows severe convergence issues. From Figure 60 to Figure 65, we can see that the water rate and oil rate for each well, total water rate and total oil rate match CMG STARS well.

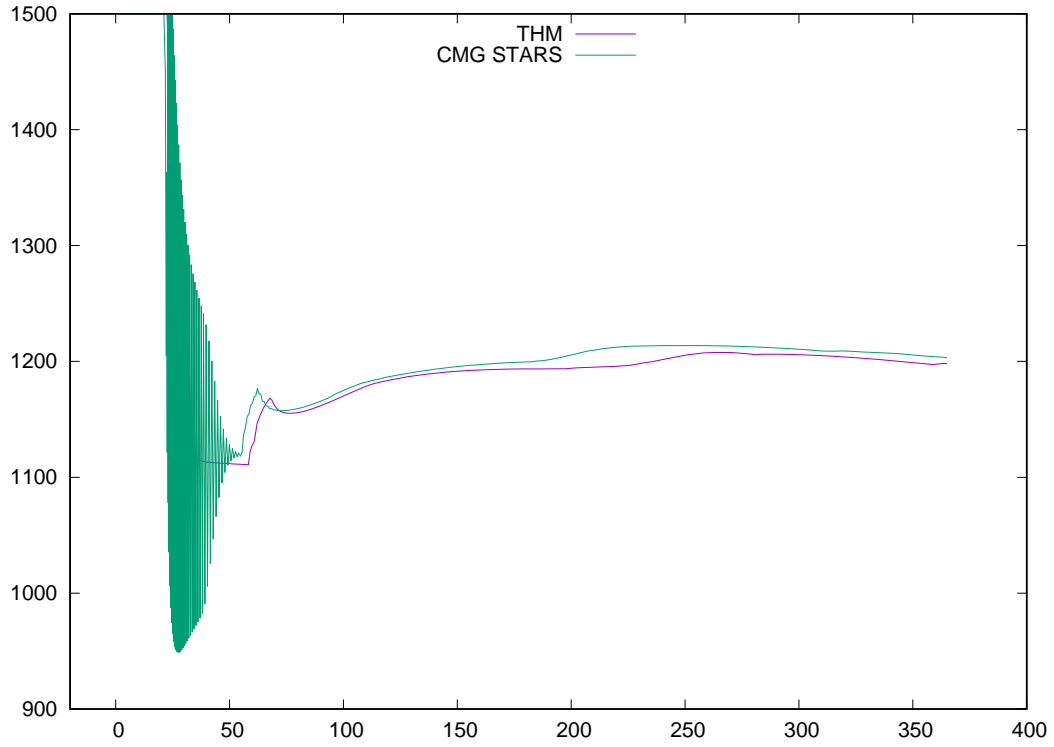


Figure 55: Example 6, rate and pressure control: injection well, bottom hole pressure (psi)

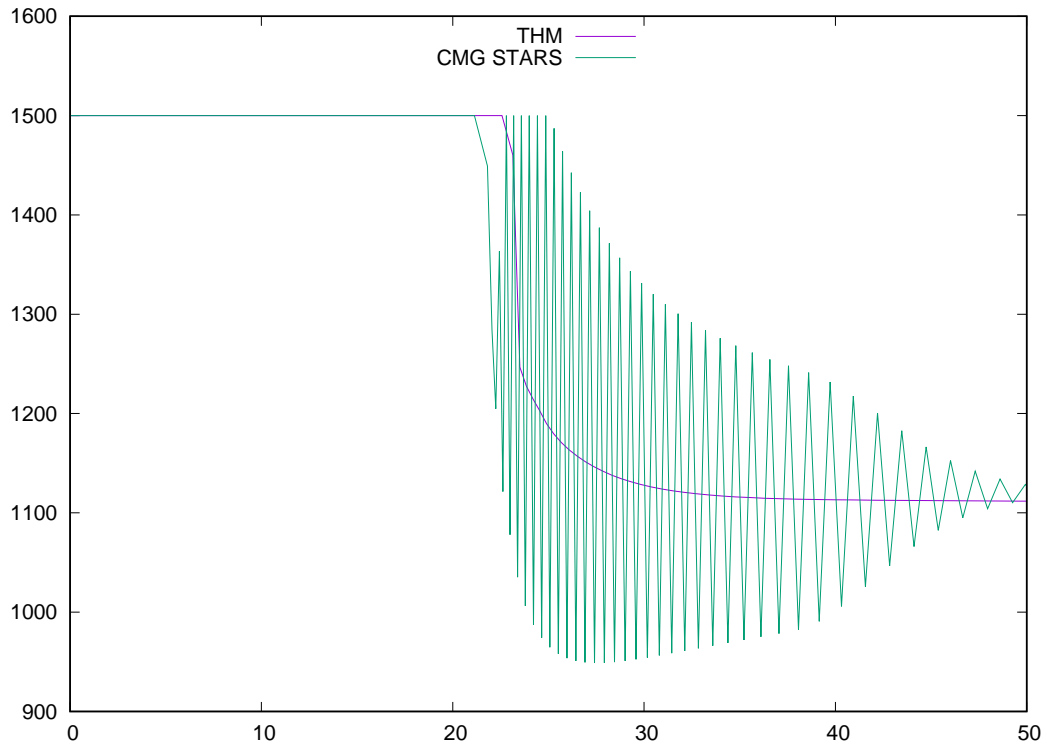


Figure 56: Example 6, rate and pressure control: injection well, bottom hole pressure (psi), first 50 days

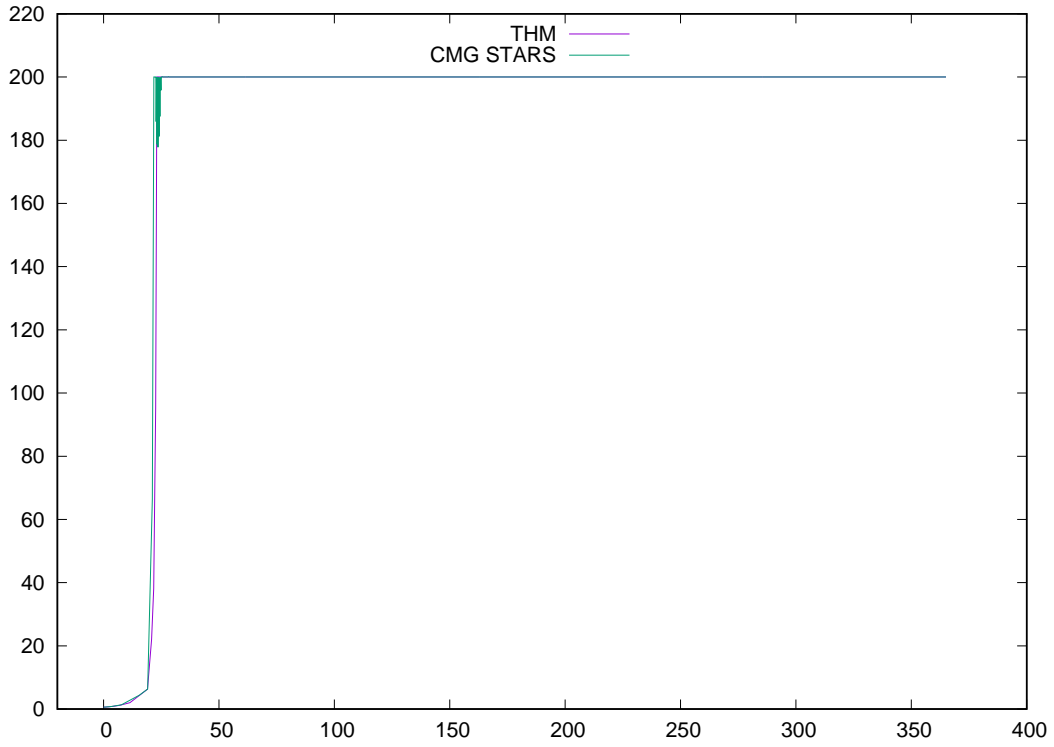


Figure 57: Example 6, rate and pressure control: water injection rate (bbl/day)

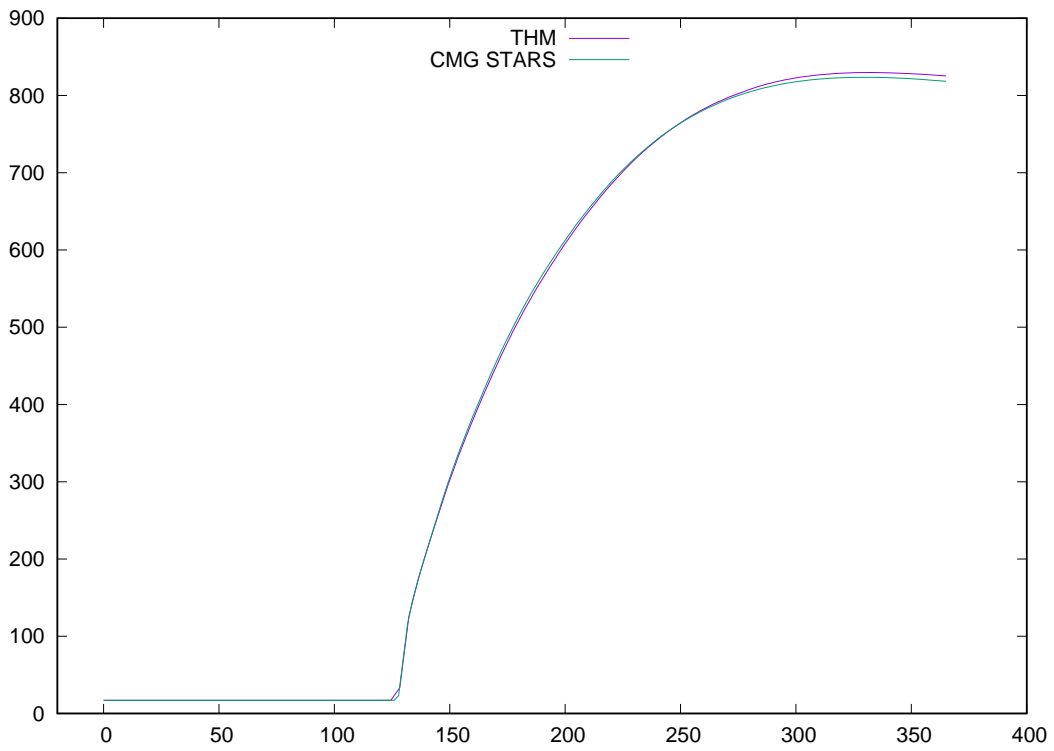


Figure 58: Example 6, rate and pressure control: first production well, bottom hole pressure (psi)

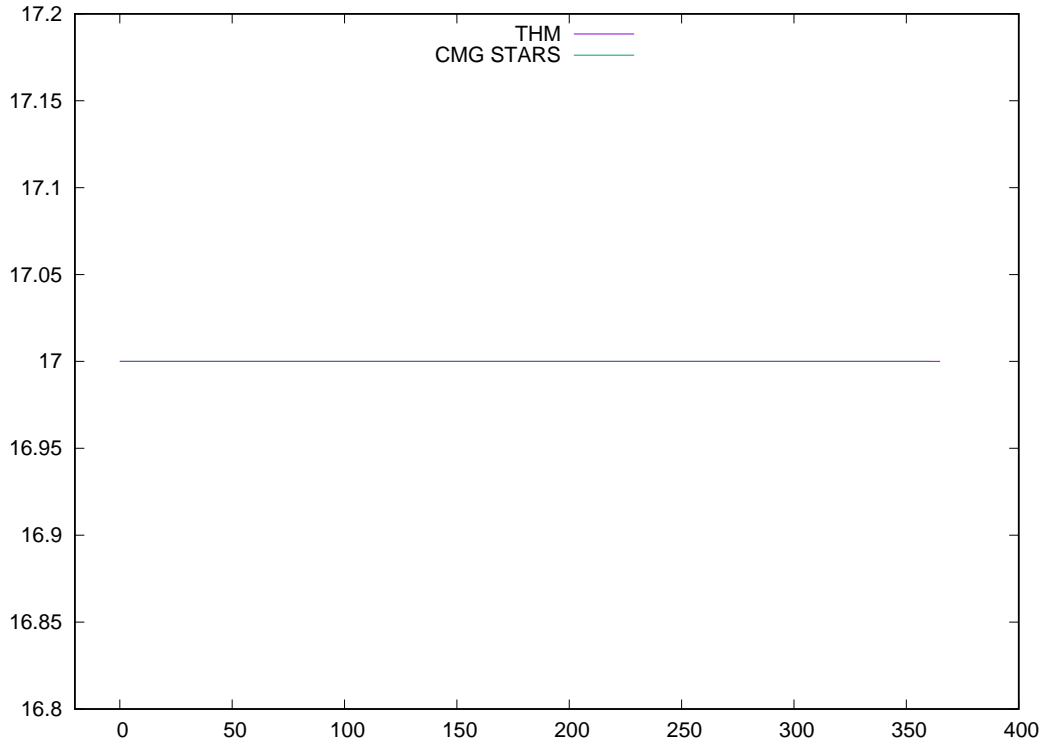


Figure 59: Example 6, rate and pressure control: second production well, bottom hole pressure (psi)

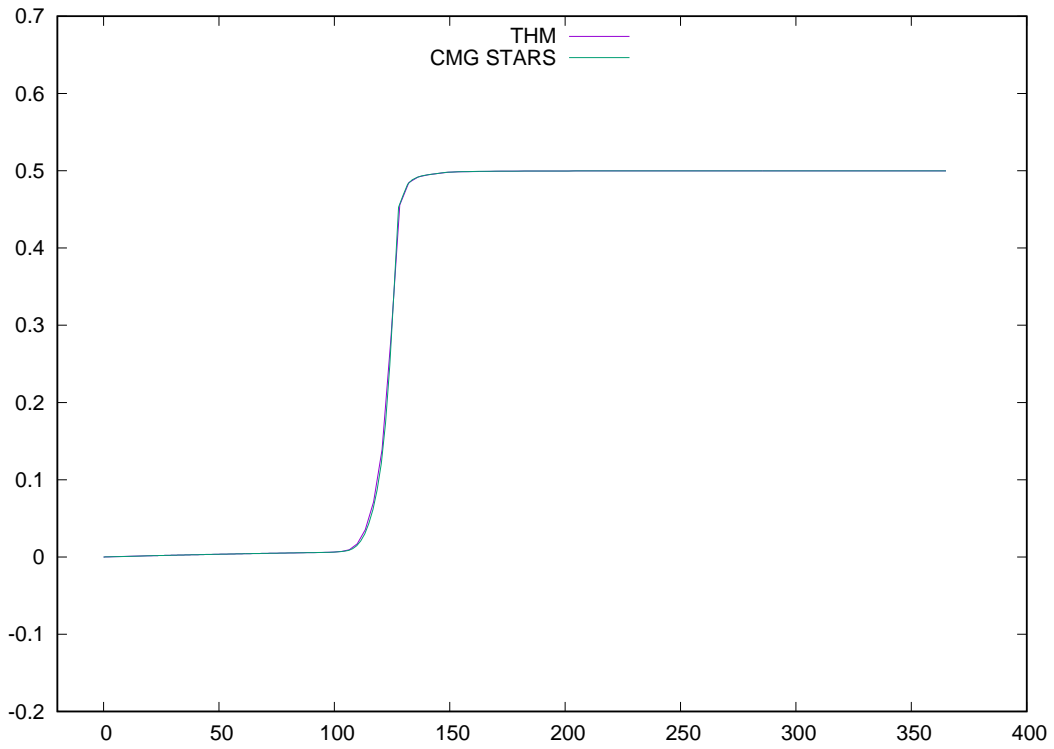


Figure 60: Example 6, rate and pressure control: water production rate (bbl/day), first production well

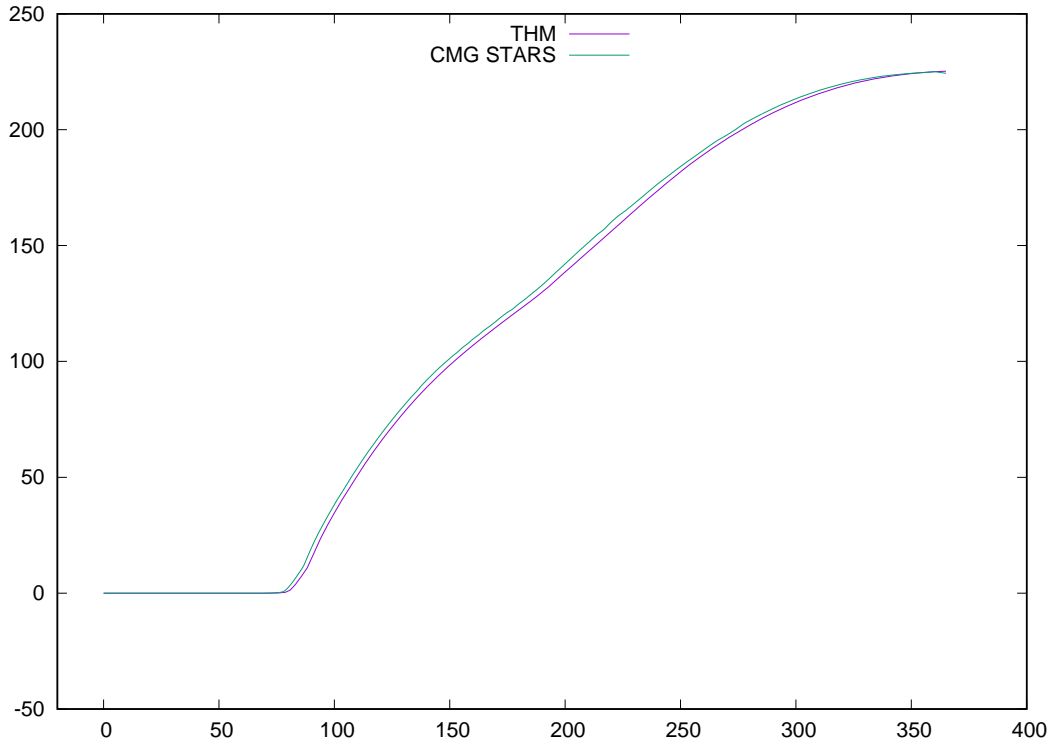


Figure 61: Example 6, rate and pressure control: water production rate (bbl/day), second production well

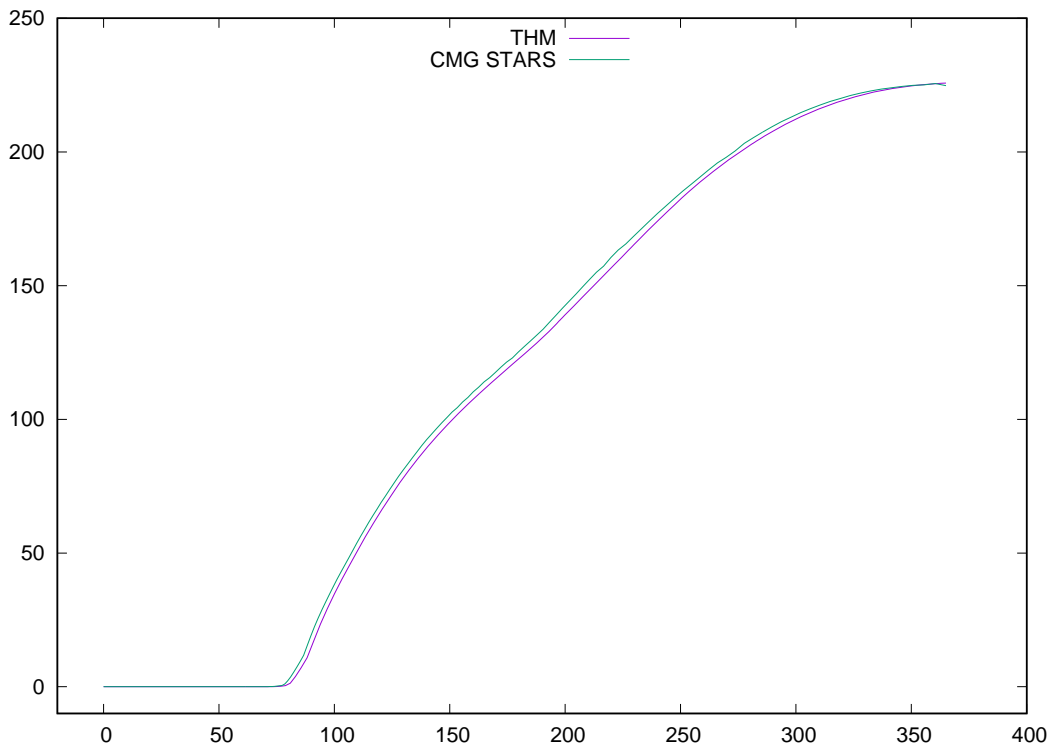


Figure 62: Example 6, rate and pressure control: total water production rate (bbl/day)

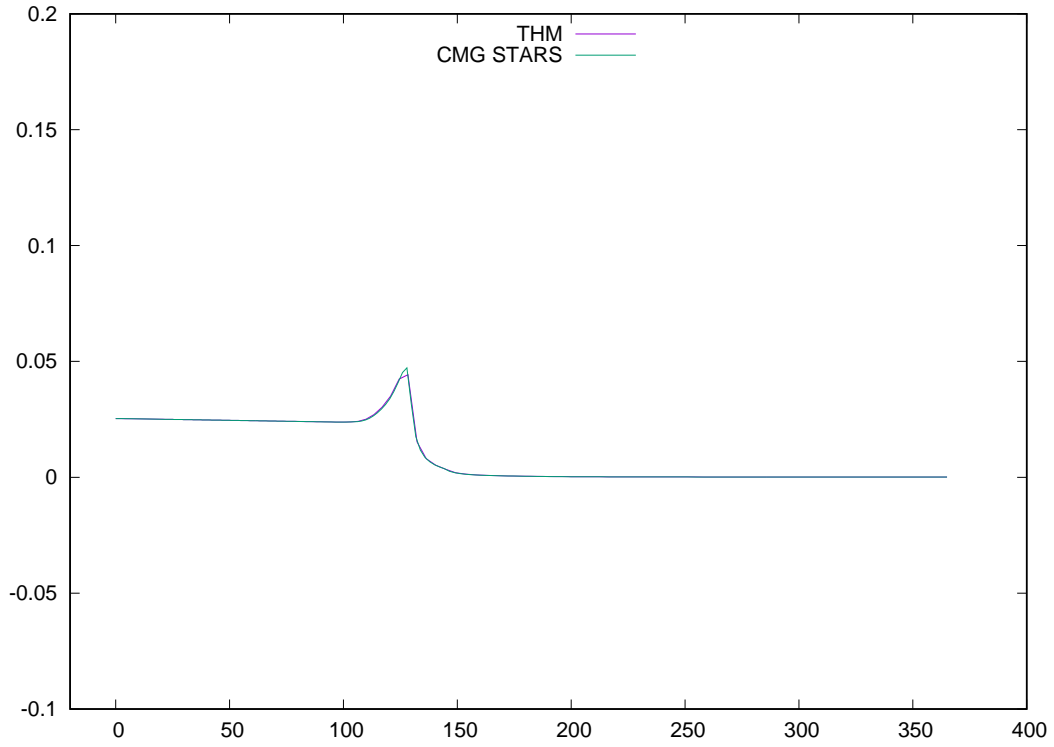


Figure 63: Example 6, rate and pressure control: oil production rate (bbl/day), first production well

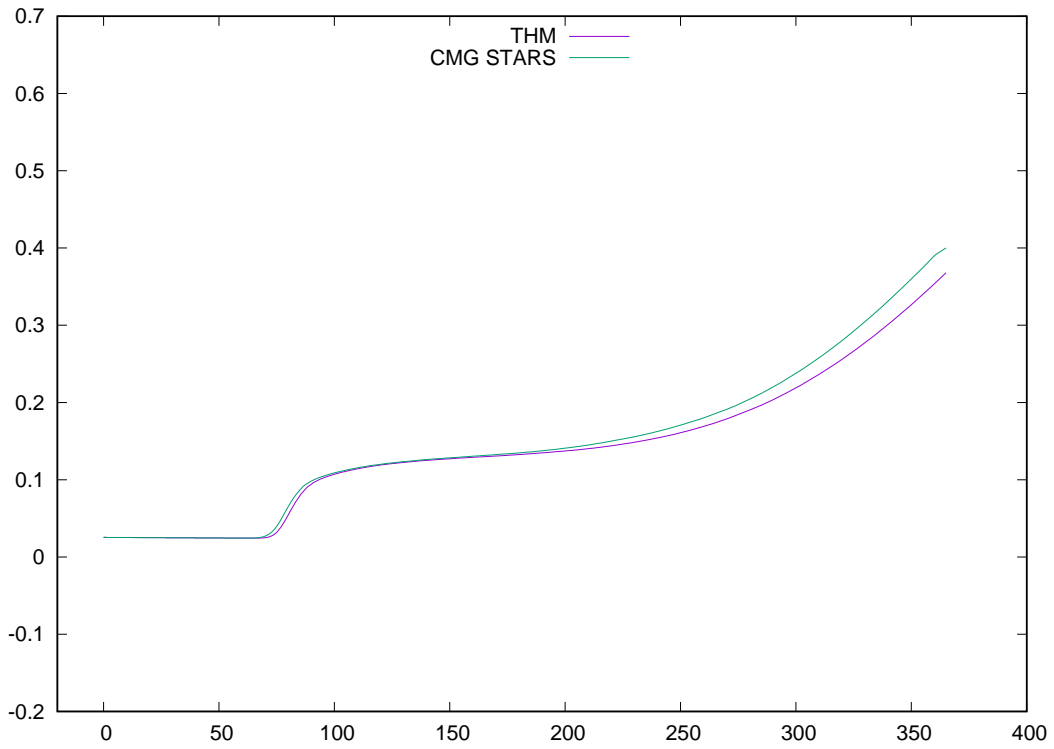


Figure 64: Example 6, rate and pressure control: oil production rate (bbl/day), second production well

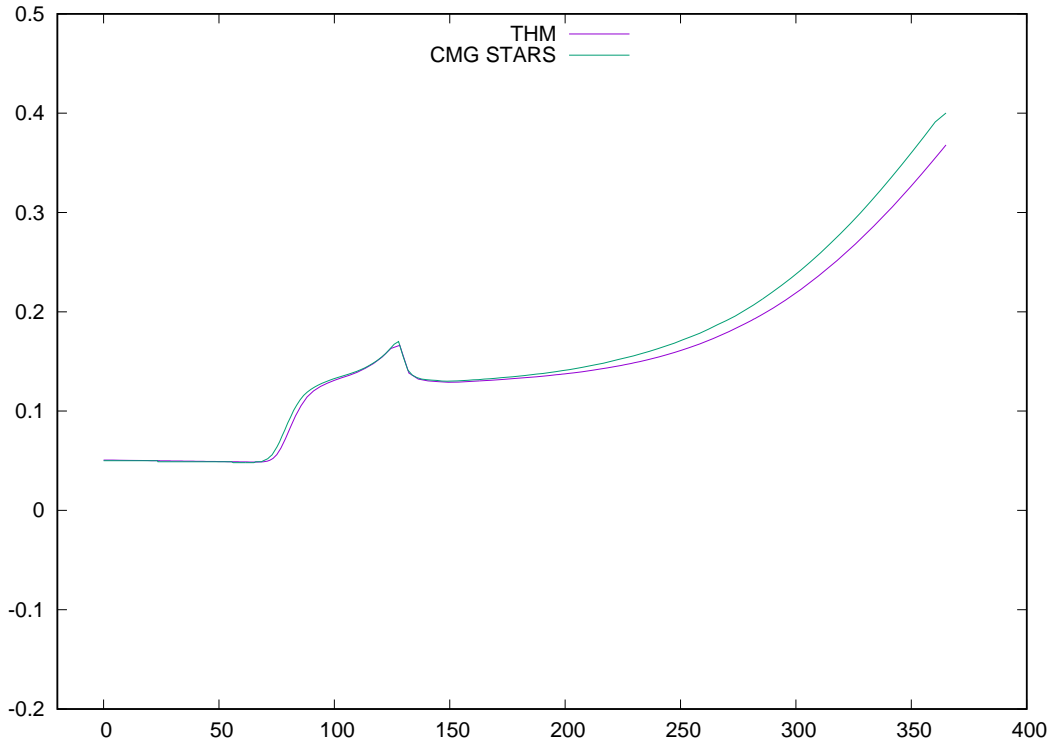


Figure 65: Example 6, rate and pressure control: total oil production rate (bbl/day)

4.2.4 Constant Heat Transfer Model

Example 7 In this example, the injection well operates at a fixed steam injection rate of 100 bbl/day, and the steam quality is 0 at a temperature of 450 F. Each production well operates at fixed bottom hole pressure of 17 psi. Constant heat transfers to each perforation at a rate of $1e6$ Btu/day. The simulation period is 365 days. Figure 66 to Figure 69 show simulated results and they are compared with CMG STARS.

Figure 66 is the bottom hole pressure and compared with CMG STARS. We can see that the match is exact. For injection rate shown by Figure 67, our convergence is smoother than CMG STARS. The water and oil production rates match very well as shown in Figure 69 and Figure 68.

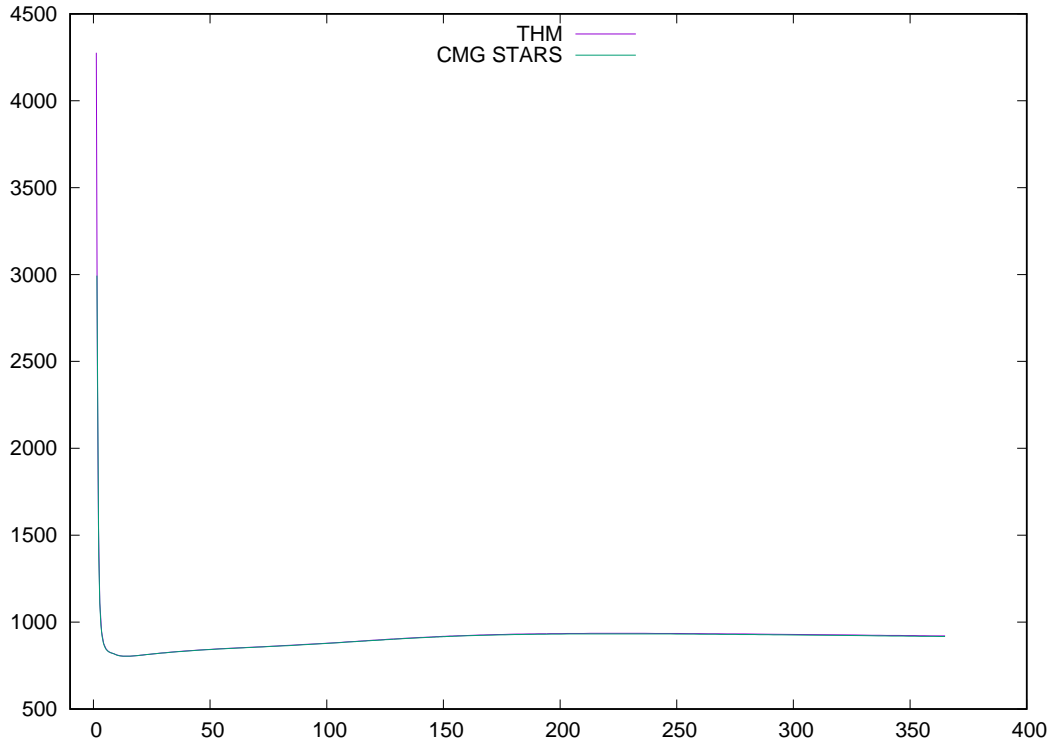


Figure 66: Example 7, constant heat transfer model: injection well, bottom hole pressure (psi)

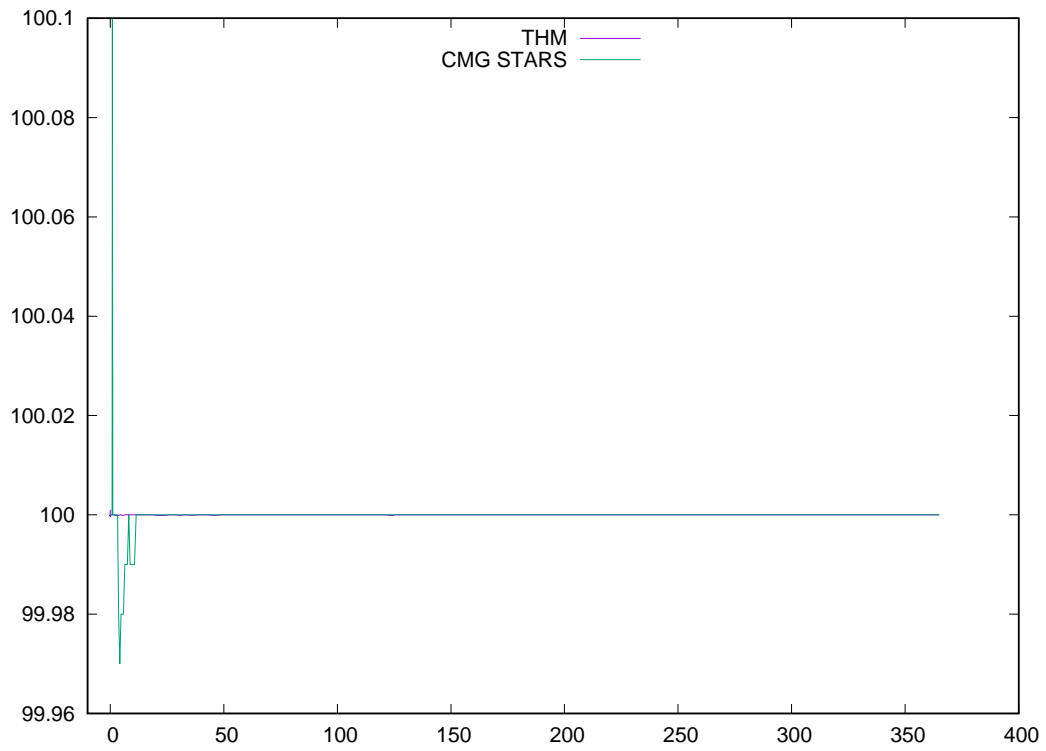


Figure 67: Example 7, constant heat transfer model: water injection rate (bbl/day)

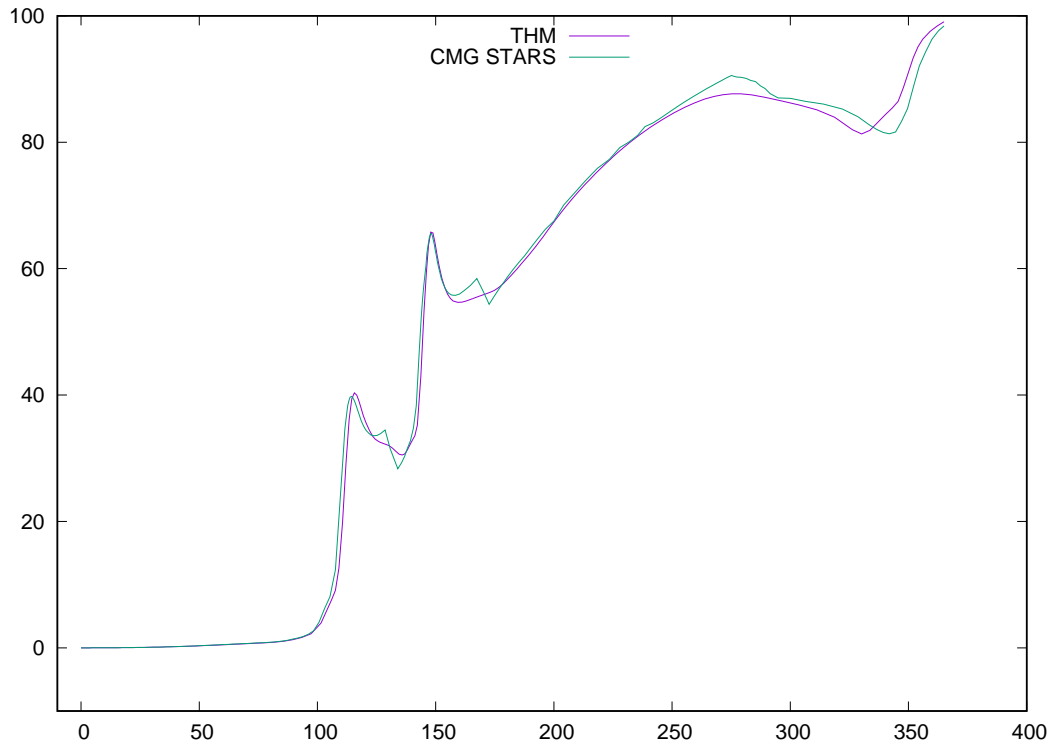


Figure 68: Example 7, constant heat transfer model: water production rate (bbl/day)

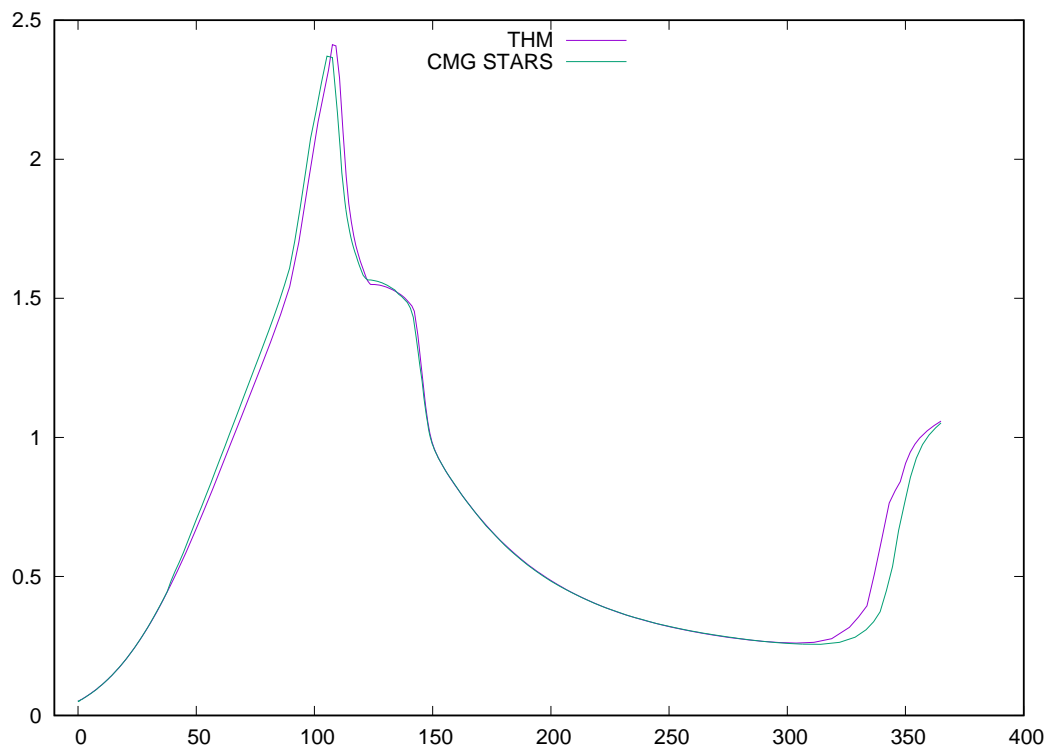


Figure 69: Example 7, constant heat transfer model: oil production rate (bbl/day)

4.2.5 Convective Heat Transfer Model

Example 8 Here the injection rate is 50 bbl/day, and production wells have fixed bottom hole pressure. Each perforation of production wells have a `uhtc` of $4e4$ btu/day-F and a temperature setpoint (`tmpset`) of 500 F. Again the simulation period is 365 days. All results are compared with CMG STARS. Figure 70, 71, 72 and 73 are injection well bottom hole pressure, injection surface rate, water production surface rate and oil production surface rate. From these figures, we can see the match between our simulator and CMG STARS is excellent.

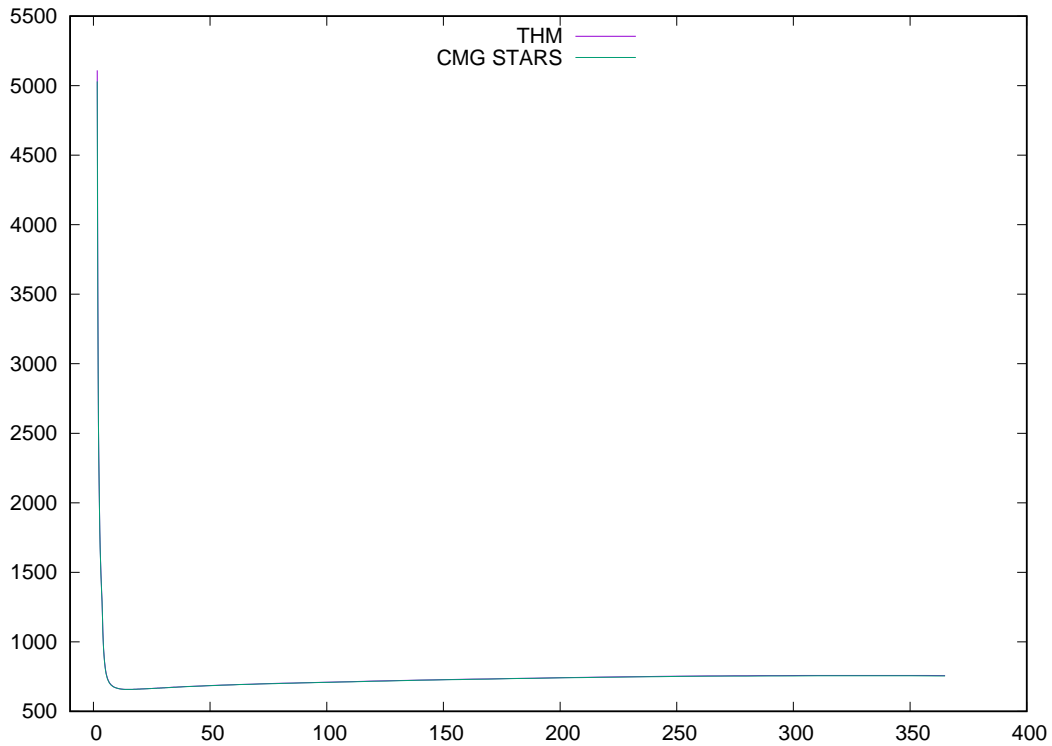


Figure 70: Example 8, convective heat transfer model: injection well, bottom hole pressure (psi)

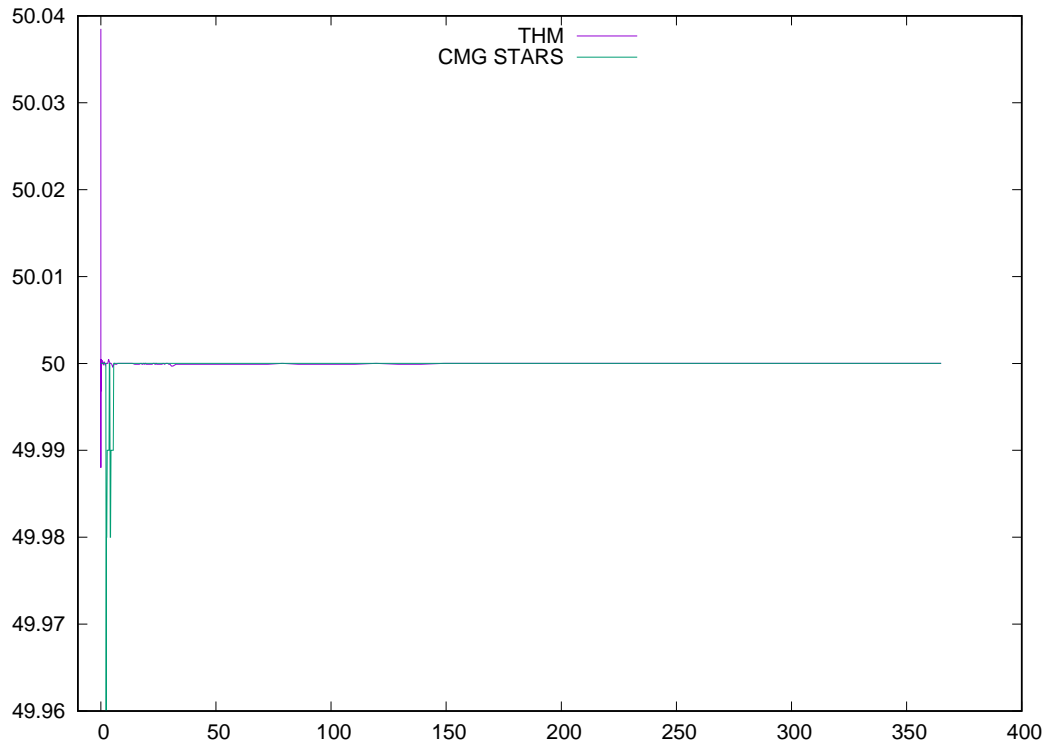


Figure 71: Example 8, convective heat transfer model: water injection rate (bbl/day)

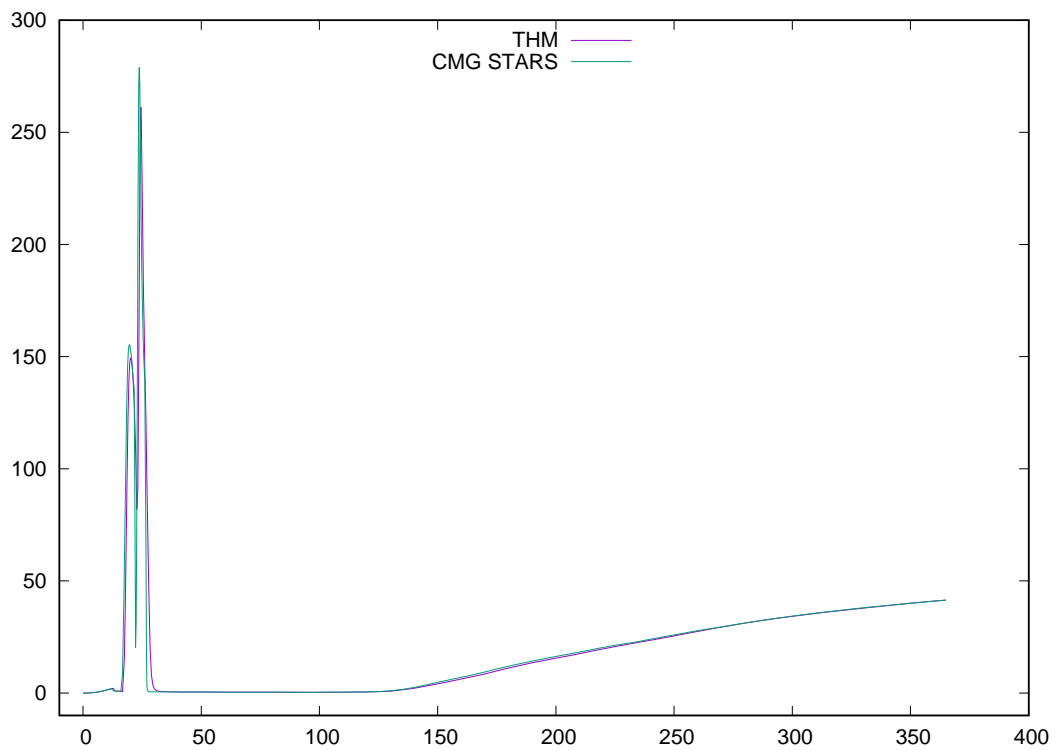


Figure 72: Example 8, convective heat transfer model: water production rate (bbl/day)

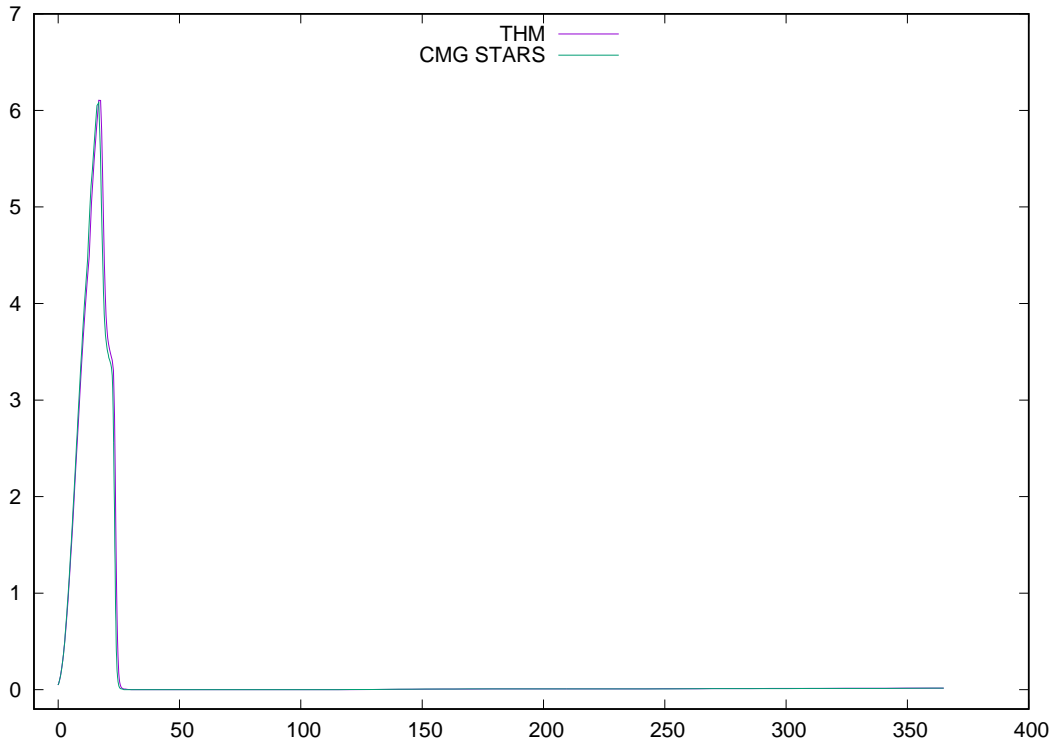


Figure 73: Example 8, convective heat transfer model: oil production rate (bbl/day)

4.2.6 Heater Well

Example 9 The injection well operates at a fixed water rate 150 bbl/day. The injected water has a steam quality of 0.3 and temperature of 450 F. The production wells operate at fixed bottom hole pressure of 17 psi. The first production well uses temperature model at 600 F, and the second production well uses rate model with heat rate 3.4e6 Btu/day. The simulation period is 365 days. Figure 74, 76, 77, and 78 present bottom hole pressure of injection well, injection rate, total water production rate and total oil production rate. All results are compared with CMG STARS.

Figure 74 and 76 show the bottom hole pressure and injection rate, from which we can see the match is good except the first 20 days. CMG STARS shows convergence issue while our simulator is more robust. The total water and oil production rates have good match, which are demonstrated by Figure 77 and Figure 78, respectively.

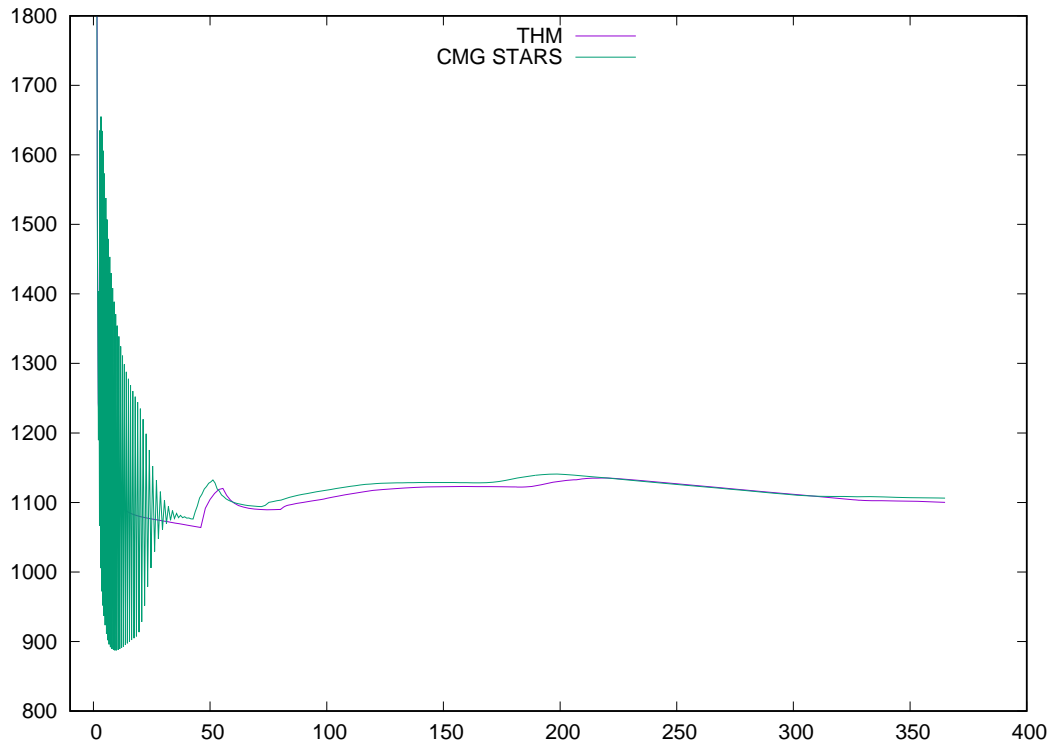


Figure 74: Example 9, heater well: injection well, bottom hole pressure (psi)

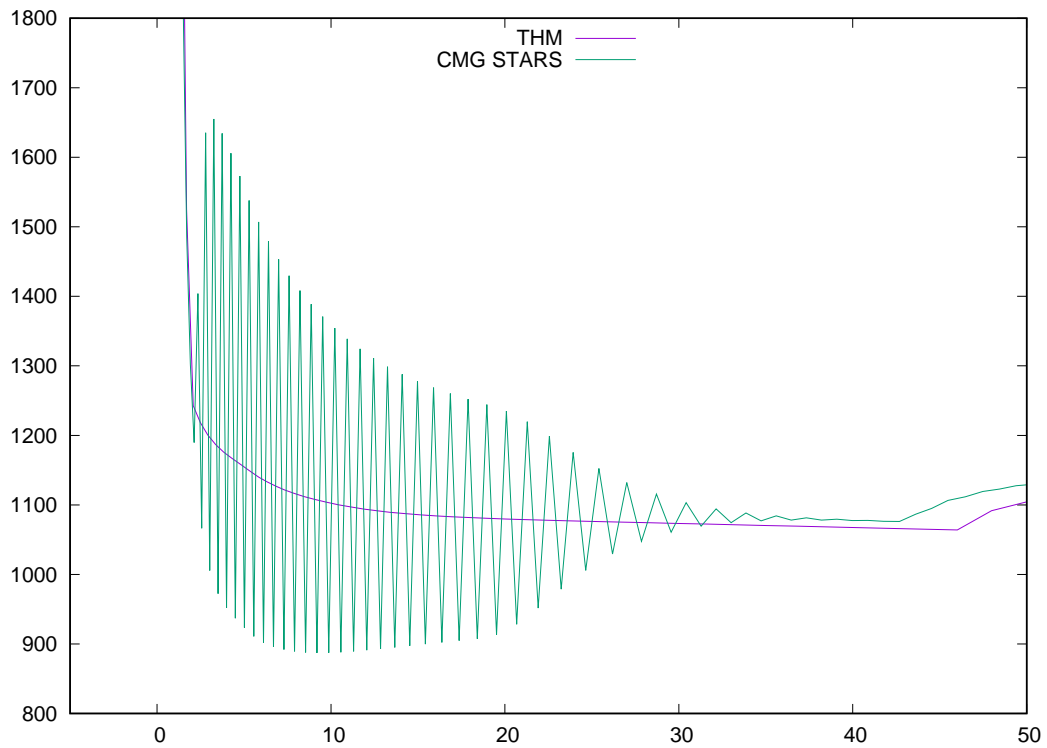


Figure 75: Example 9, heater well: injection well, bottom hole pressure (psi), first 50 days

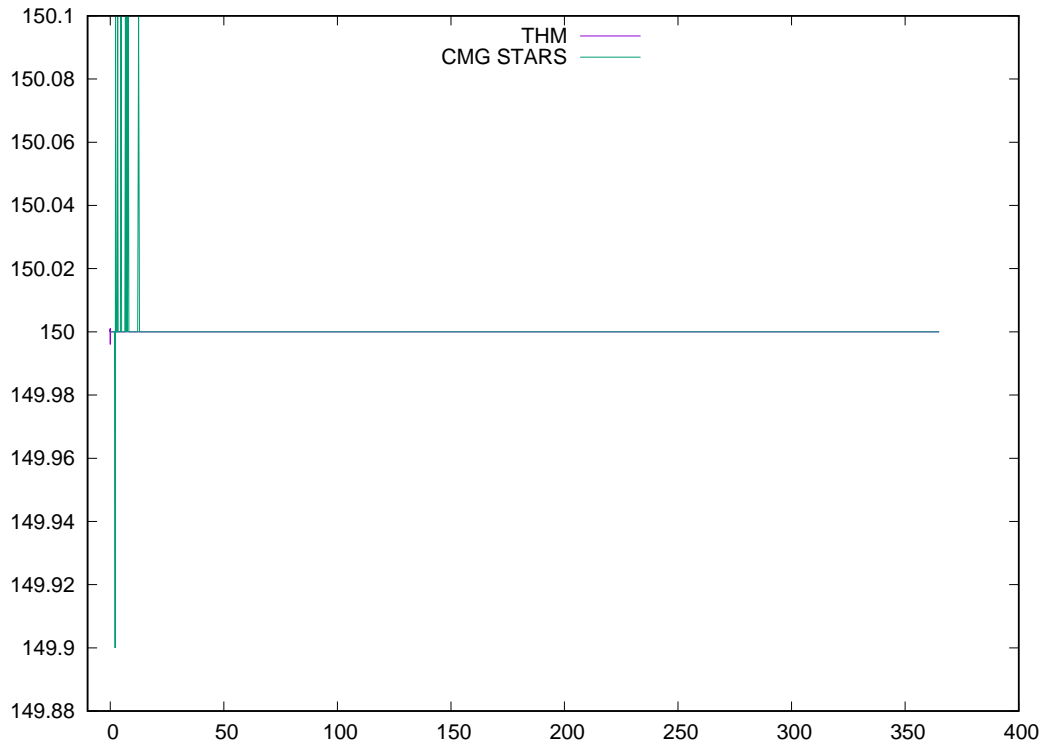


Figure 76: Example 9, heater well: water injection rate (bbl/day)

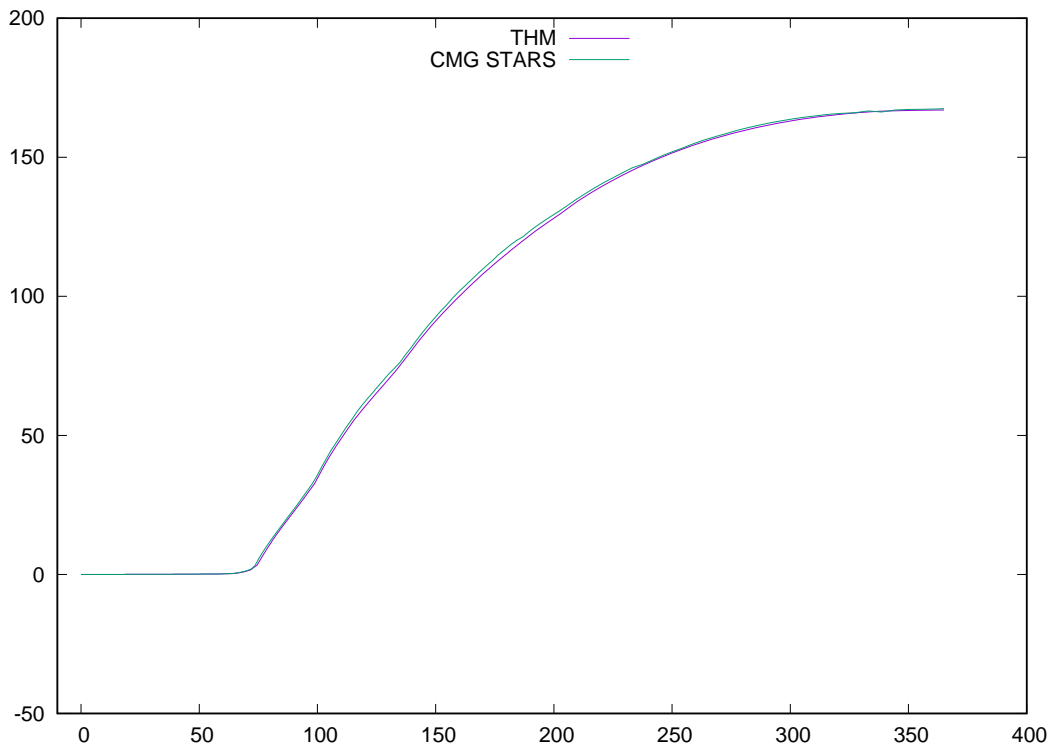


Figure 77: Example 9, heater well: water production rate (bbl/day)

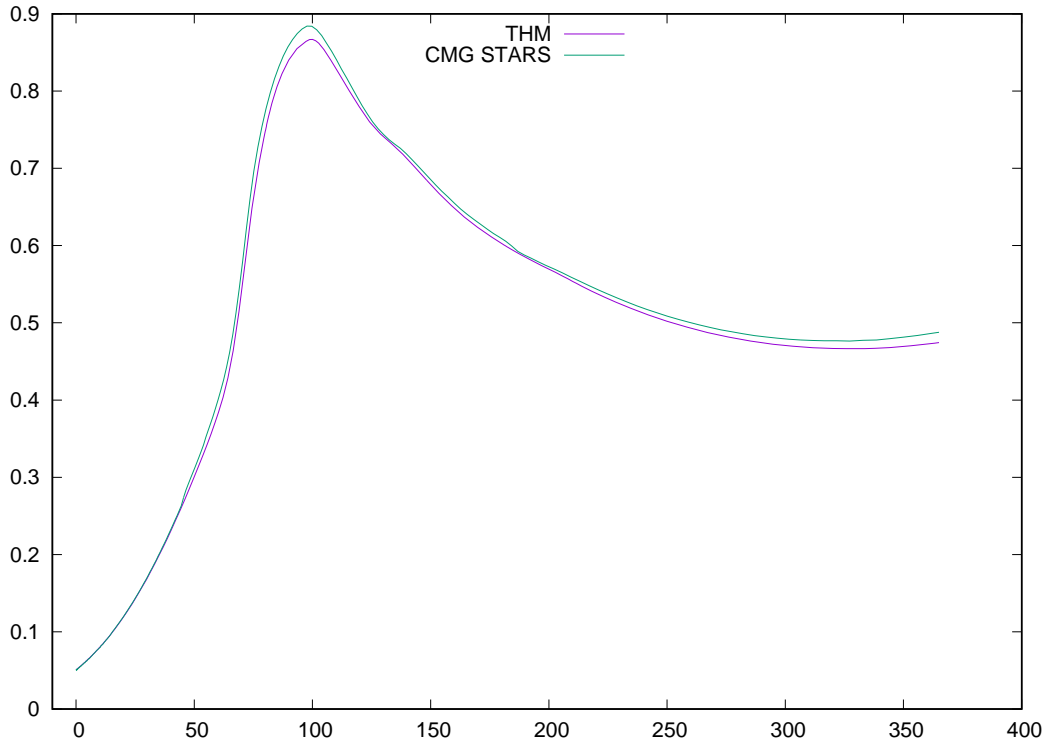


Figure 78: Example 9, heater well: oil production rate (bbl/day)

4.2.7 Heater Constraints

The heater controls can be applied simultaneously in one thermal model. They can be applied to different wells, and for a well, it may use a combination of constant heater, convective heater, and heater well model.

Example 10 The injection well operates at maximal injection rate of 300 bbl/day water and maximal bottom hole pressure of 5,000 psi. Its steam quality is 0.5. The first production well operates at minimal bottom hole pressure of 17 psi and maximal liquid rate of 5 bbl/day. The temperature heater model is applied with a specify temperature of 600 F. The second production well operates at minimal bottom hole pressure of 17 psi and maximal oil rate of 4 bbl/day. The dual rate/temperature model is applied with a specify heat rate of 3.4e6 Btu/day and a specify temperature of 611. Constant heat transfer model is applied to each perforation at a constant heat rate of 1e6 Btu/day. The convective heat transfer model is also applied to each perforation at 4e4 Btu/day-F and a temperature setpoint of 500. Results are shown from Figure 79 to Figure 89. Bottom hole pressure, water rate and oil rate of each well are compared with CMG STARS.

All results match CMG STARS well. For injection well, Figure 79 shows CMG has convergence issues while our simulator and numerical methods are more stable.

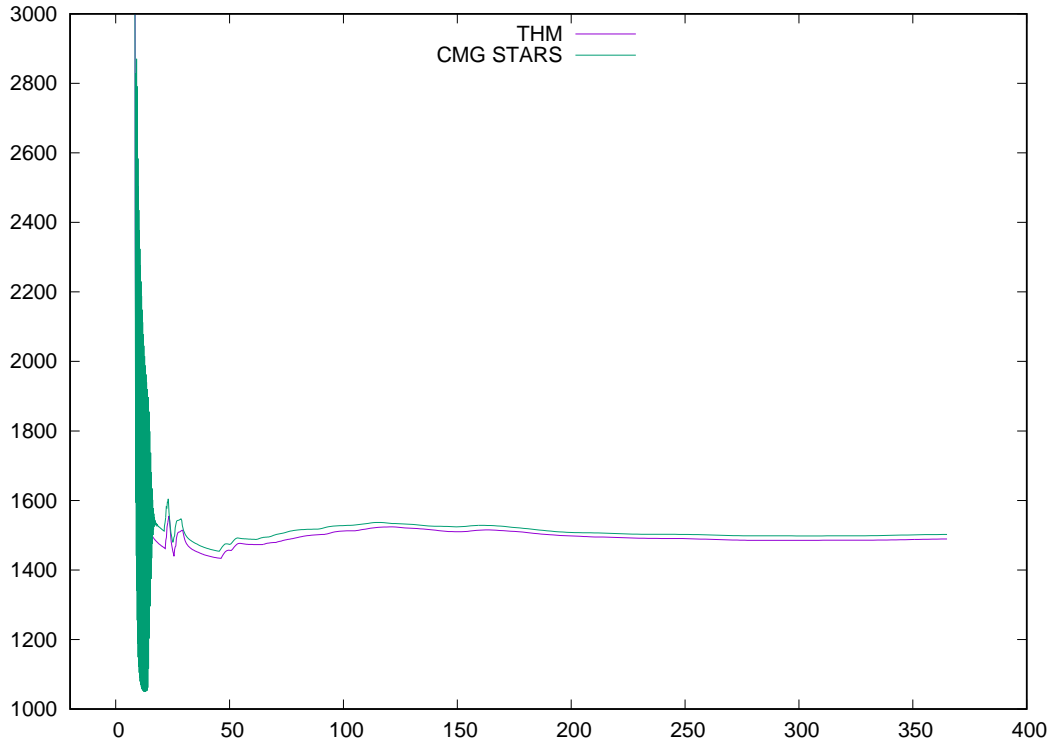


Figure 79: Example 10, combination of multiple heat models: injection well, bottom hole pressure (psi)

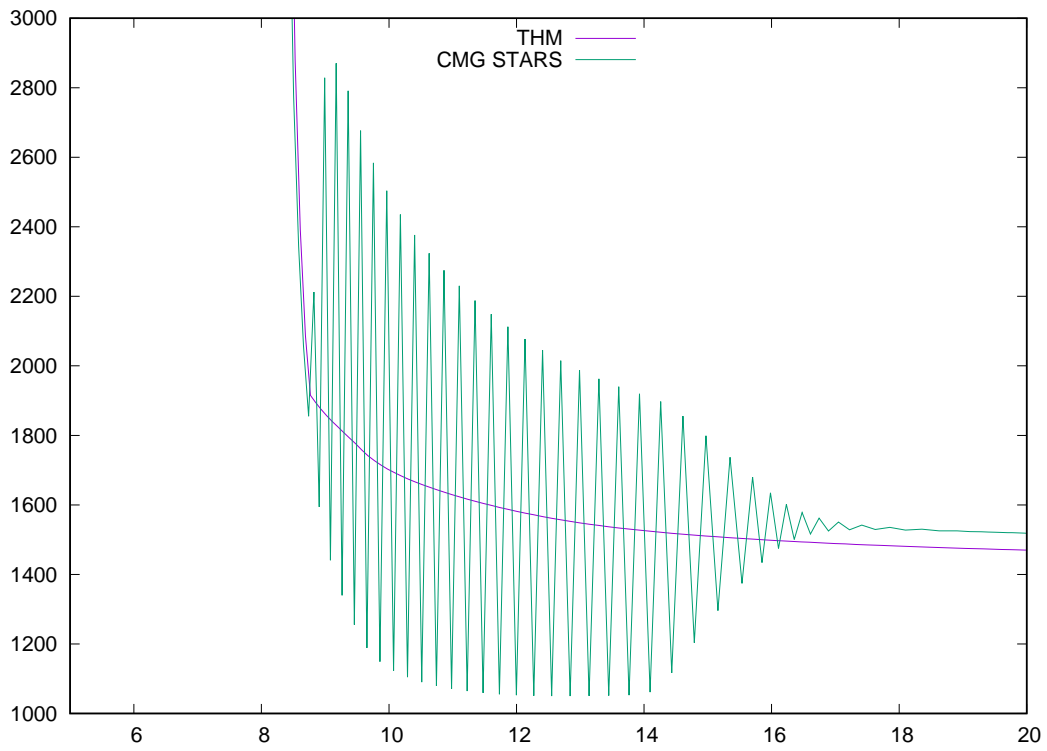


Figure 80: Example 10, combination of multiple heat models: injection well, bottom hole pressure (psi), first 20 days

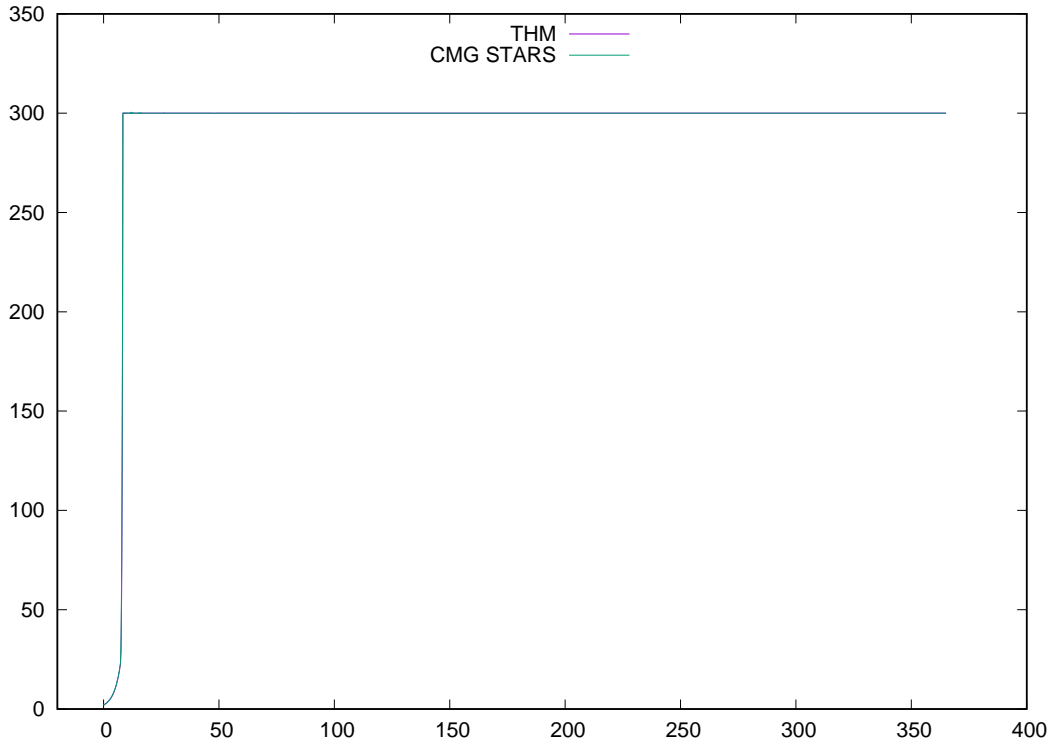


Figure 81: Example 10, combination of multiple heat models: total water injection rate (bbl/day)

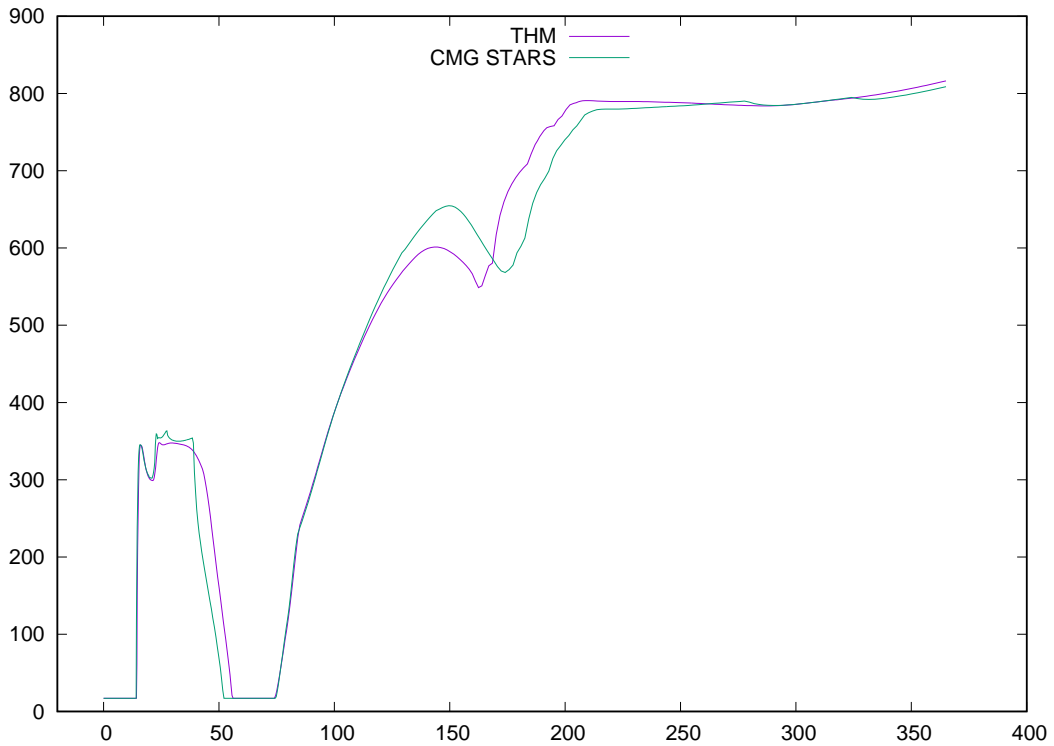


Figure 82: Example 10, combination of multiple heat models: first production well, bottom hole pressure (psi)

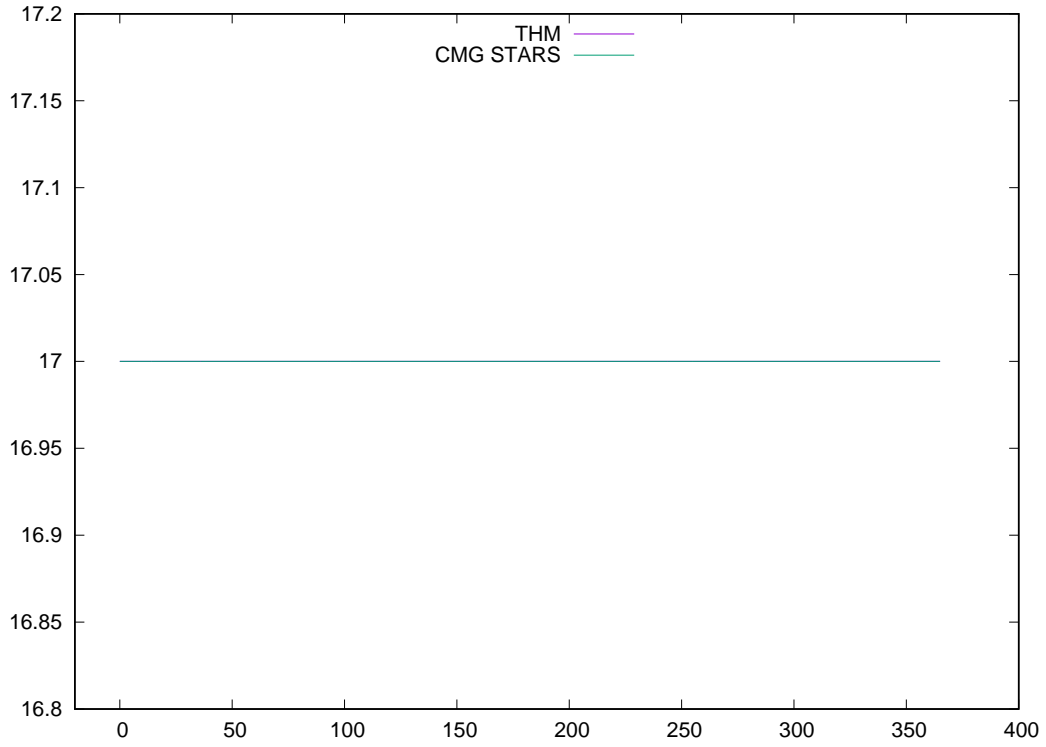


Figure 83: Example 10, combination of multiple heat models: second production well, bottom hole pressure (psi)

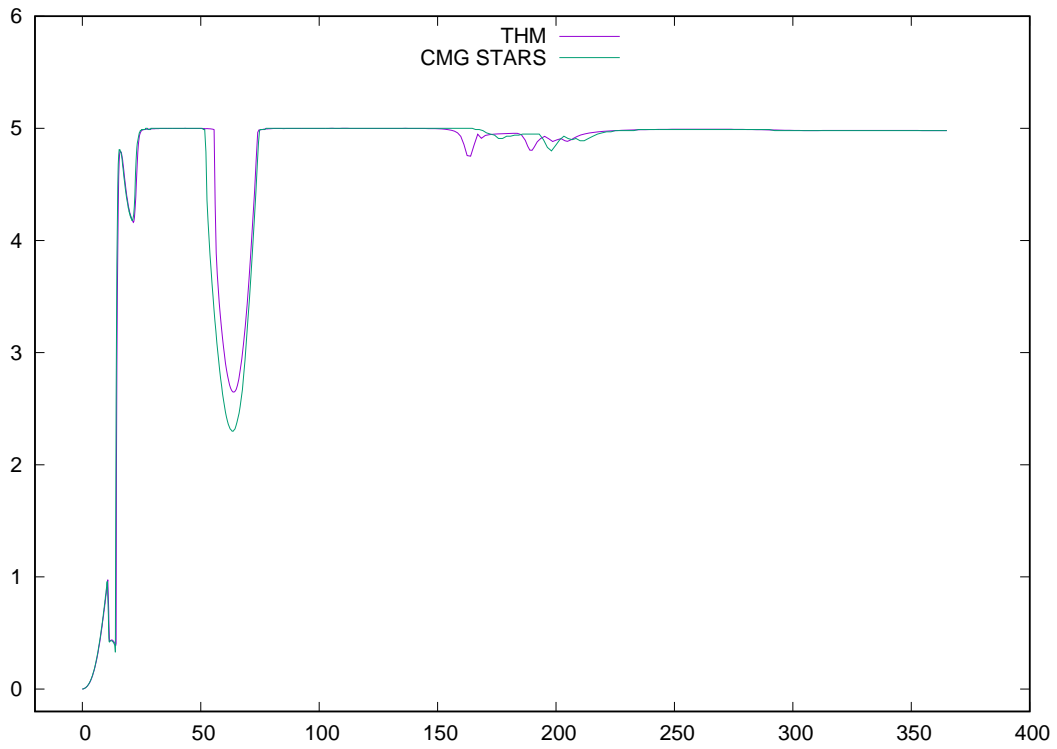


Figure 84: Example 10, combination of multiple heat models: water production rate (bbl/day), first production well

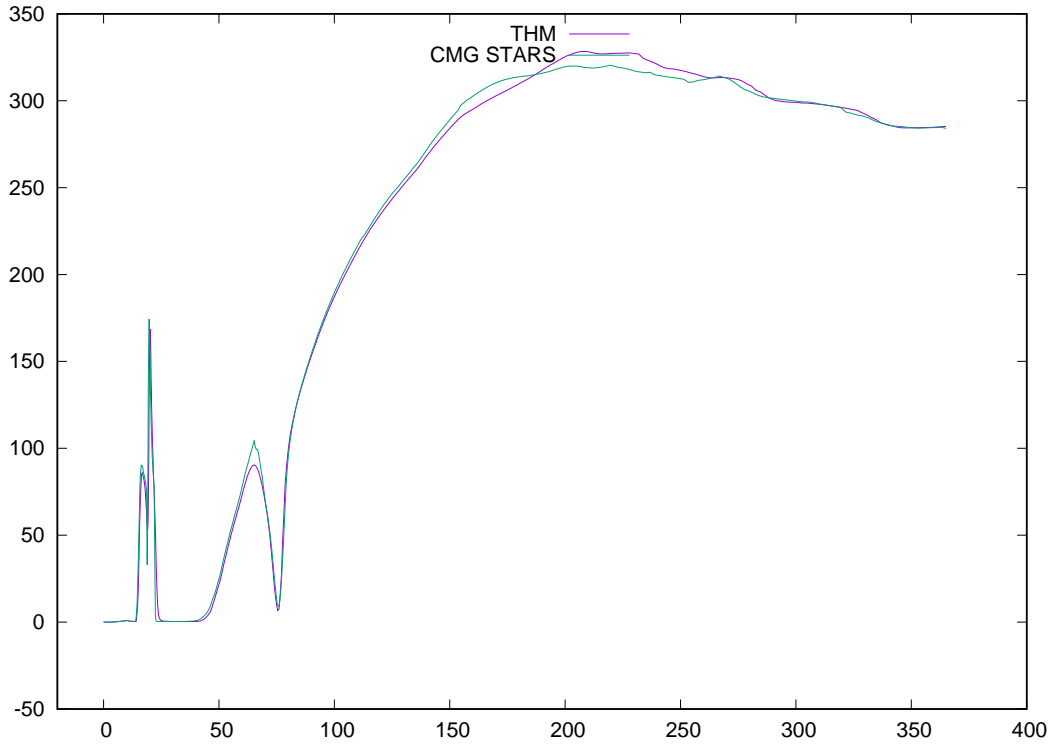


Figure 85: Example 10, combination of multiple heat models: water production rate (bbl/day), second production well

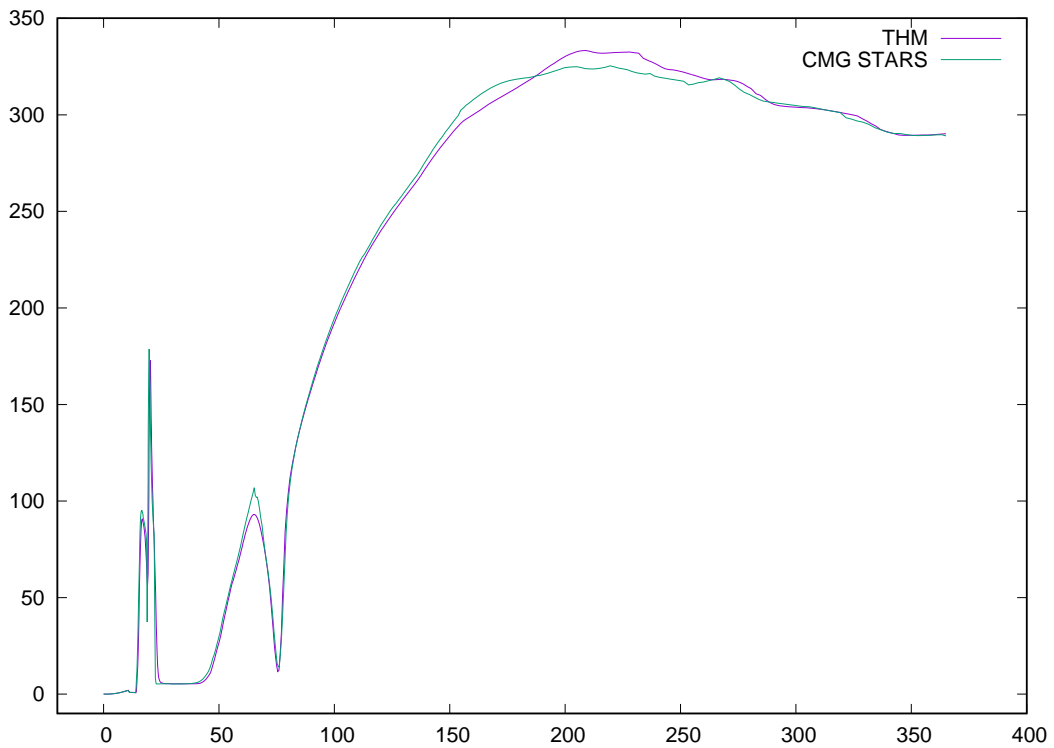


Figure 86: Example 10, combination of multiple heat models: total water production rate (bbl/day)

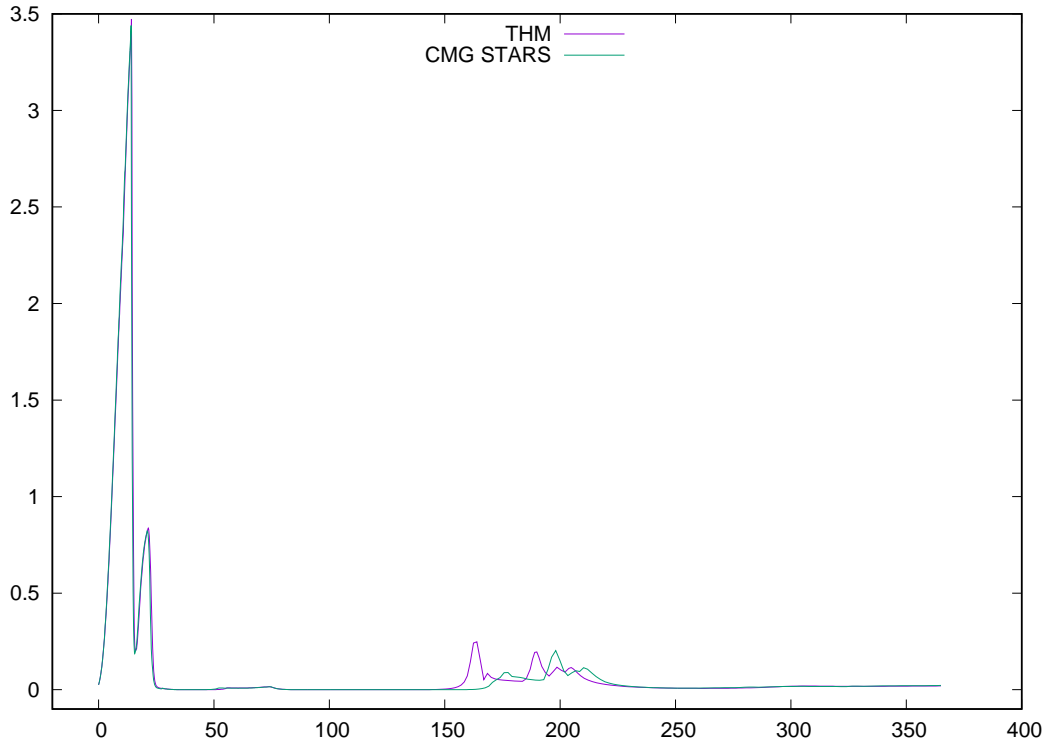


Figure 87: Example 10, combination of multiple heat models: oil production rate (bbl/day), first production well

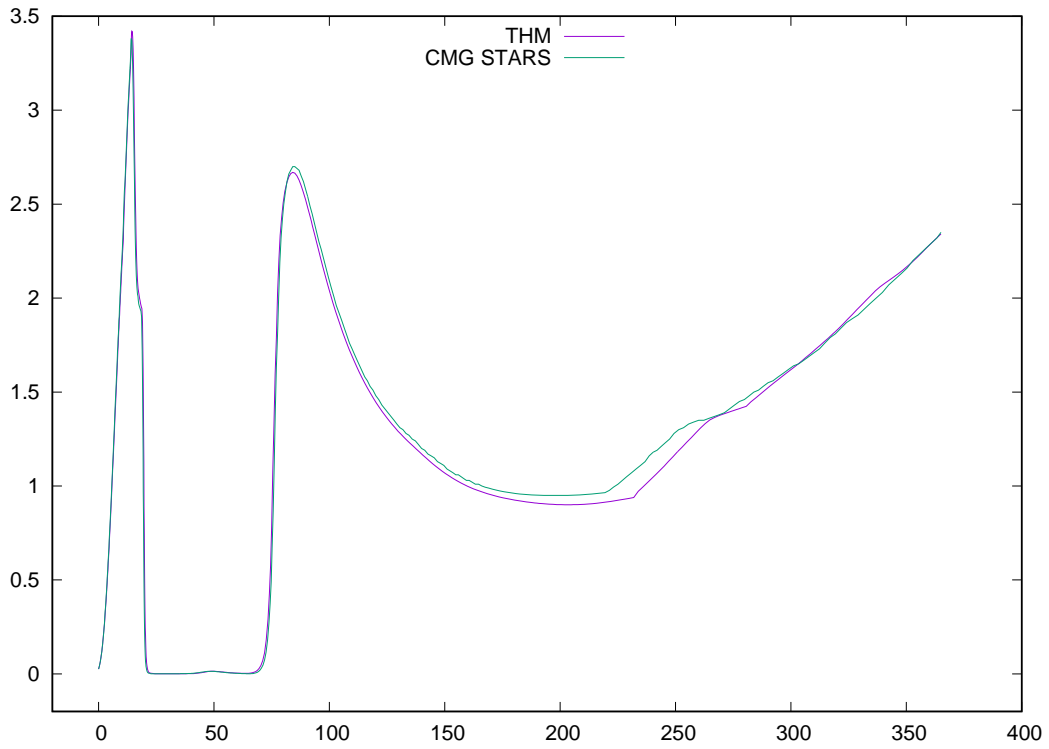


Figure 88: Example 10, combination of multiple heat models: oil production rate (bbl/day), second production well

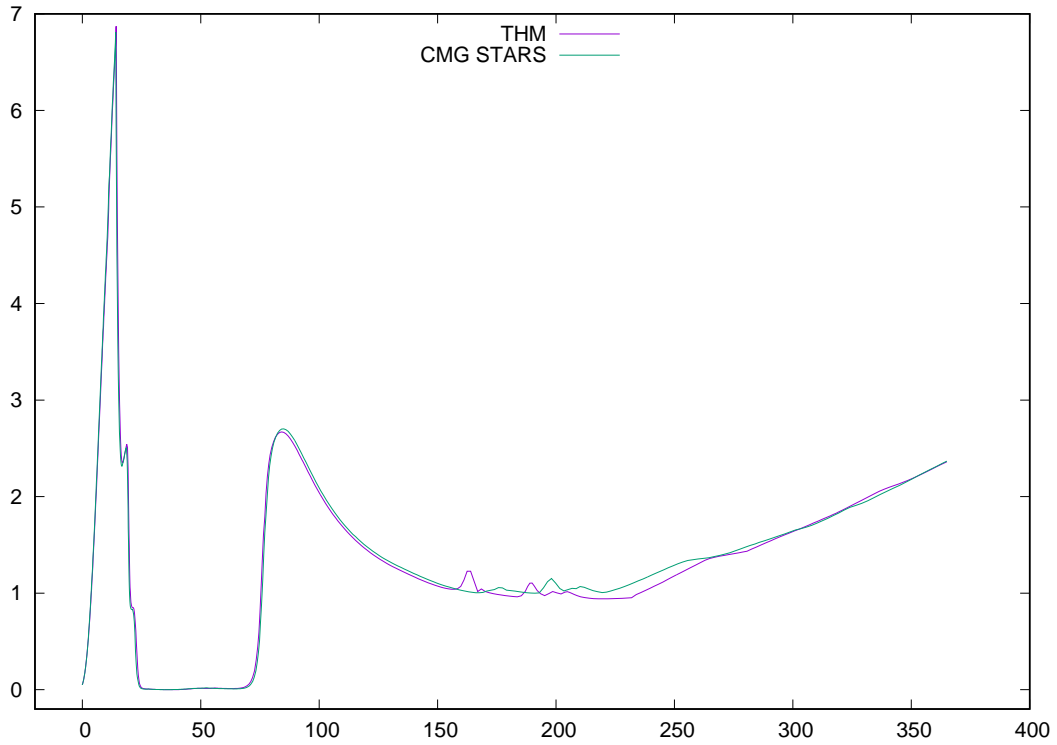


Figure 89: Example 10, combination of multiple heat models: total oil production rate (bbl/day)

4.2.8 Subcool Control

Example 11 The injection well operates at fixed injection rate of 100 bbl/day. Both production wells operate at fixed bottom hole pressure of 17 psi. The steamtrap temperature differences are 20 F and 30 F respectively. Bottom hole pressure of each well is presented, and total water and oil production rates are also presented, from Figure 90 to Figure 94.

Figure 90 is bottom hole pressure of injection well, and our results match CMG STARS exactly. Figure 91 and Figure 92 show that the steamtrap works, as steam is injected into reservoir to heat reservoir and fluid, their temperature increases. The steamtrap works by increasing the wellbore pressure to prevent live steam production. The water and oil production also match CMG STARS well.

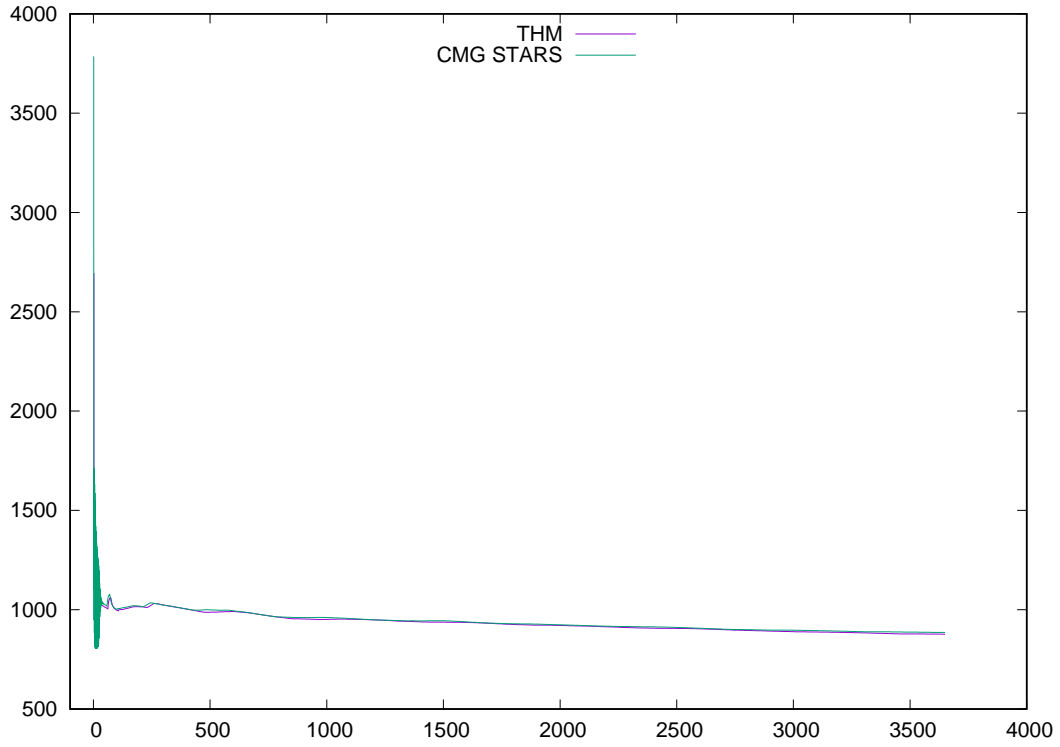


Figure 90: Example 11, subcool (steam trap): injection well, bottom hole pressure (psi)

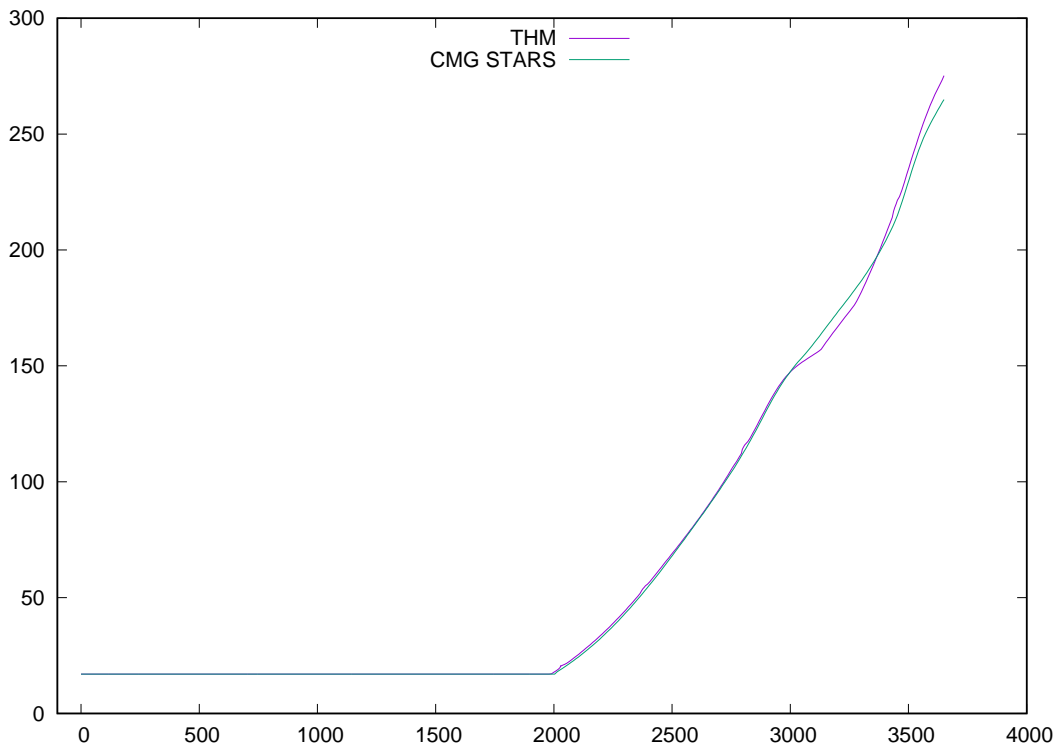


Figure 91: Example 11, subcool (steam trap): first production well, bottom hole pressure (psi)

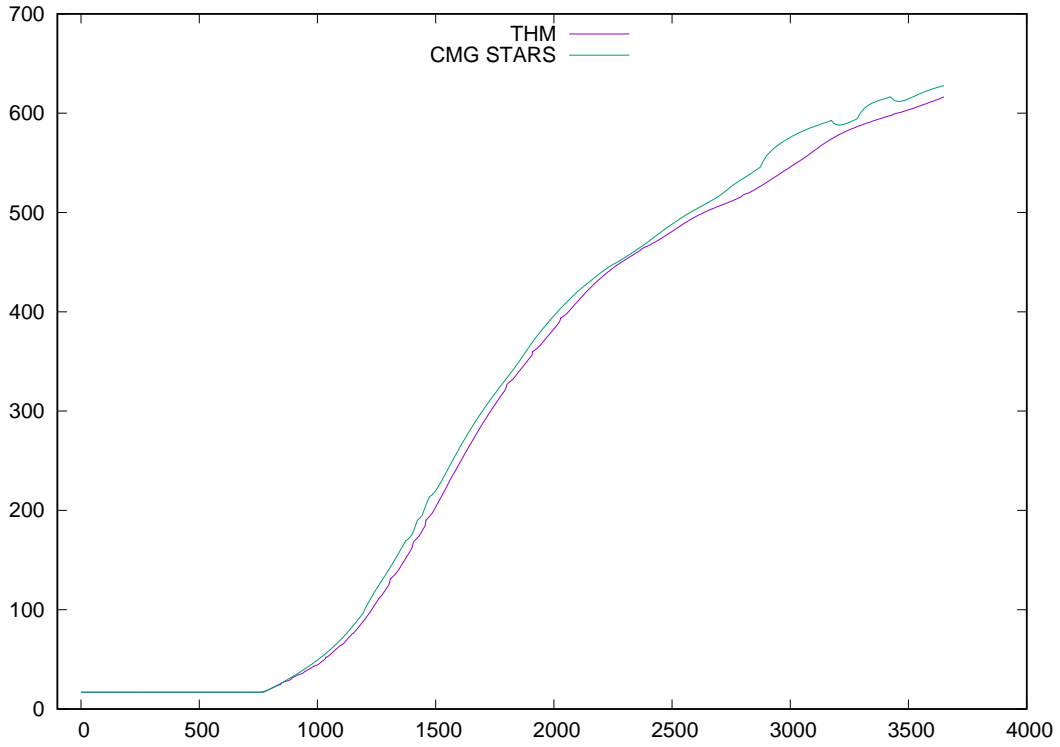


Figure 92: Example 11, subcool (steam trap): second production well, bottom hole pressure (psi)

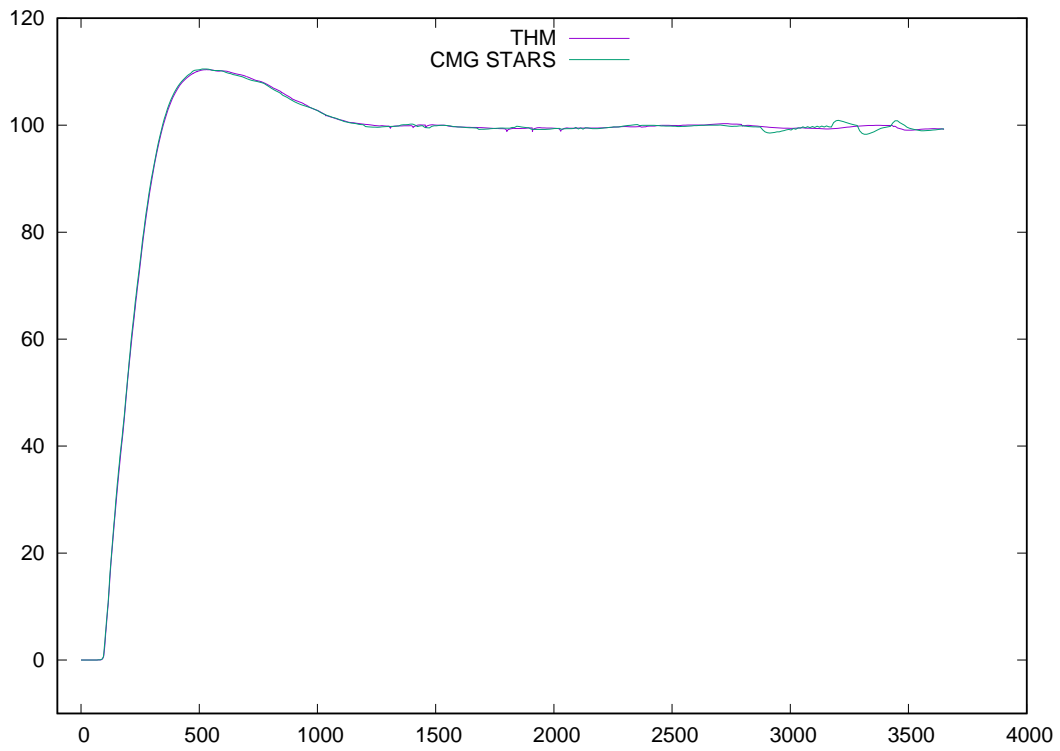


Figure 93: Example 11, subcool (steam trap): water production rate (bbl/day)

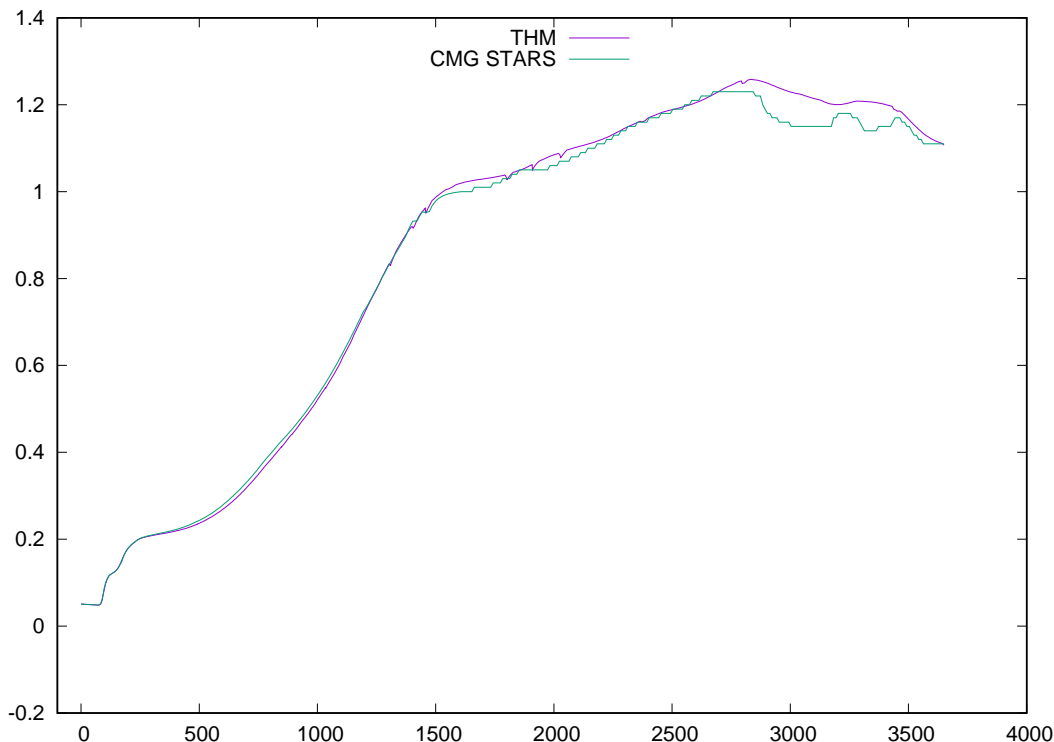


Figure 94: Example 11, subcool (steam trap): oil production rate (bbl/day)

4.3 Numerical Performance

Example 12 This example tests a SAGD model with 25 well pairs, which includes one water component, one heavy component, one light component and two inert gas components, and their properties are the same as Example 3. The grid dimension is $100 \times 100 \times 6$ and grid size is $10ft \times 10ft \times 1ft$. The simulation time is 200 days and the maximal time step is 10 days. The Newton tolerance is $1e-3$ and its maximal iterations are 15. The linear solver is BICGSTAB, its tolerance is also $1e-3$ and its maximal iterations are 60. GJE is the decoupling method. Table 10 provides the well info. All injectors operate at 3 bbl/day water injection with steam quality of 0.2 and temperature of 450 F. All producers operate at bottom hole pressure of 2000 psi and steam trap temperature difference of 20 F. The equivalent CMG STARS model is simulated. However, after 12 hours run, CMG STARS always has time steps around $1e-4$ day, and it simulates 0.3269 days after 415 time steps, so we have to terminate it. Numerical summaries of our simulator are shown in Table 11. Since the model is small, only one computing node is employed.

Table 11 provides numerical summaries for time steps (and time cut), total Newton iterations, total linear solver iterations, total simulation time, average Newton iterations per time step, average linear iterations per Newton iteration. As expected, when more CPU cores (MPIs) are used, time steps and linear iterations increase. Even through, the results show that our numerical methods are effective, which can solve a time step in less than 4 Newton iterations and solve a linear system in less than 20 iterations. When more CPU cores are used, the simulation time is cut, which shows that parallel computing is a powerful tool for reservoir simulation.

Example 13 This example tests one water component, one heavy component and one light component. SAGD process with 756 well pairs is simulated. The grid has a dimension of $60 \times 220 \times 85$ and size of $20ft \times 10ft \times 1ft$. All wells are horizontal wells along x direction, if the index of y direction of a grid block equals to 3, 7, 11, 15, 19, 23, 27, 31, 35, 39, 43, 47, 51, 55, 59, 63, 67, 71, 75, 79, 83, 87, 91, 95, 99, 103, 107, 111, 115, 119, 123, 127, 131, 135, 139, 143, 147, 151, 155, 159, 163, 167, 171, 175, 179, 183, 187, 191, 195, 199, 203, 207, 211, or 215, and the index of z direction equals to 4, 10, 16, 22, 28, 34, 40, 46, 52, 58, 64, 70, 76, or 82, then an injection well is defined. For example, (1:60, 3, 10) defines an injection well at (3,10) of yz -plane, and its perforations are from 1 to 60. This defines 756 injection wells. A production well is defined two blocks

Injector perforation	Well index	Producer perforation	Well index
1:100 2 3	1e5	1:100 2 6	1e5
1:100 6 3	1e5	1:100 6 6	1e5
1:100 10 3	1e5	1:100 10 6	1e5
1:100 14 3	1e5	1:100 14 6	1e5
1:100 18 3	1e5	1:100 18 6	1e5
1:100 22 3	1e5	1:100 22 6	1e5
1:100 26 3	1e5	1:100 26 6	1e5
1:100 30 3	1e5	1:100 30 6	1e5
1:100 34 3	1e5	1:100 34 6	1e5
1:100 38 3	1e5	1:100 38 6	1e5
1:100 42 3	1e5	1:100 42 6	1e5
1:100 46 3	1e5	1:100 46 6	1e5
1:100 50 3	1e5	1:100 50 6	1e5
1:100 54 3	1e5	1:100 54 6	1e5
1:100 58 3	1e5	1:100 58 6	1e5
1:100 62 3	1e5	1:100 62 6	1e5
1:100 66 3	1e5	1:100 66 6	1e5
1:100 70 3	1e5	1:100 70 6	1e5
1:100 74 3	1e5	1:100 74 6	1e5
1:100 78 3	1e5	1:100 78 6	1e5
1:100 82 3	1e5	1:100 82 6	1e5
1:100 86 3	1e5	1:100 86 6	1e5
1:100 90 3	1e5	1:100 90 6	1e5
1:100 94 3	1e5	1:100 94 6	1e5
1:100 98 3	1e5	1:100 98 6	1e5

Table 10: Well info of Example 12

CPU cores	# Time steps	# Newton	Avg. Newton	# Linear solver	Avg. Linear	Time
4	96(4)	314	3.27	5587	17.80	1420.63
8	100(6)	338	3.38	6157	18.22	816.69
16	101(4)	326	3.23	6215	19.06	558.22

Table 11: Numerical summaries of Example 12

under an injection well. Therefore, 756 well pairs and total 1512 wells are defined in the model. All injection wells operate at 10 bbl/day water injection, with a steam quality of 0.2 and temperature of 450F. All production wells operate at fixed bottom hole pressure of 100 psi. Each perforation of an injection well is heated at rate of 1e5 btu/day. The model file has around 20,000 lines. Their properties are the same as Example 2. The simulation time is 100 days. 8 CPU cores (8 MPIs) are employed. The Newton tolerance is 1e-4 and its maximal iterations are 15. The linear solver is BICGSTAB, its tolerance is also 1e-4 and its maximal iterations are 100.

Table 12 presents numerical results, including preconditioners, decoupling methods, total time steps and time cuts, total Newton iterations, and total linear iteration. Here NA means the combination fails to simulate the model. The results clearly show that a proper decoupling method is critical to the success of linear solver and CPR-type preconditioners. The GJE decoupling and the FRS+GJE decoupling work better than the ABF decoupling.

Example 14 This example tests one water component, one heavy component, one light component and two inert gas components. Their properties are the same as Example 3. The grid and well configurations are the same as Example 13. The simulation time is 100 days. 8 CPU cores (8 MPIs) are employed. The Newton tolerance is 1e-4 and its maximal iterations are 15. The linear solver is BICGSTAB, its tolerance is also 1e-4 and its maximal iterations are 100.

Table 13 presents numerical results, including preconditioners, decoupling methods, total time steps and time cuts, total Newton iterations, and total linear iteration. Again, NA means the combination fails to simulate the model. The linear

Preconditioner	Decoupling	Time steps	# Newton	# Linear solver
CPR-FP	NONE	NA	NA	NA
CPR-FP	FRS	NA	NA	NA
CPR-FP	DRS	NA	NA	NA
CPR-FP	ABF	NA	NA	NA
CPR-FP	GJE	101 (12)	598	8856
CPR-FP	DRS+ABF	NA	NA	NA
CPR-FP	DRS+GJE	95 (10)	559	8090
CPR-FP	FRS+ABF	NA	NA	NA
CPR-FP	FRS+GJE	96 (10)	552	7608
CPR-PF	NONE	NA	NA	NA
CPR-PF	FRS	NA	NA	NA
CPR-PF	DRS	NA	NA	NA
CPR-PF	ABF	125 (15)	738	18680
CPR-PF	GJE	105 (10)	585	11263
CPR-PF	DRS+ABF	103 (9)	563	12642
CPR-PF	DRS+GJE	109 (11)	636	12947
CPR-PF	FRS+ABF	NA	NA	NA
CPR-PF	FRS+GJE	109 (12)	640	13050
CPR-FPF	NONE	NA	NA	NA
CPR-FPF	FRS	NA	NA	NA
CPR-FPF	DRS	NA	NA	NA
CPR-FPF	ABF	NA	NA	NA
CPR-FPF	GJE	97 (10)	566	7887
CPR-FPF	DRS+ABF	NA	NA	NA
CPR-FPF	DRS+GJE	97 (10)	566	7813
CPR-FPF	FRS+ABF	NA	NA	NA
CPR-FPF	FRS+GJE	97 (10)	559	7666

Table 12: Numerical summary of Example 13

systems from this example are much larger than those from previous example, and they are more difficult to solve. The results show that all ABF decoupling and FRS+ABF methods fail.

Example 15 This example tests one water component, one heavy component and one light component. SAGD process with 7406 well pairs (14812 wells, 7406 injectors and 7406 producers) is simulated. The grid has a dimension of $60 \times 2200 \times 85$, 11 million grid blocks, and size of $20ft \times 10ft \times 2ft$. All wells are horizontal wells along x direction. All injection wells operate at 5 bbl/day water injection, with a steam quality of 0.2 and temperature of 450F. All production wells operate at fixed bottom hole pressure of 300 psi. All wells are modelled by implicit method. The model file has around 185,000 lines. Their properties are the same as Example 2. The simulation time is 100 time steps due to system running time limit. The initial time step is $1e-6$ days. 10 nodes and 200 CPU cores (200 MPIs) are employed on Niagara, Compute Canada. The Newton tolerance is $1e-3$ and its maximal iterations are 15. The linear solver is BICGSTAB, its tolerance is also $1e-4$ and its maximal iterations are 100. The maximal changes in a time step for pressure, saturation, molar fraction and temperature are 500 psi, 0.1, 0.1 and 15 F.

Table 14 shows that all tests pass. The Newton method converges in around three iterations, while linear solver converges in four to five iterations in average. For a specific preconditioner, the FRS+GJE decoupling method is always better than the GJE method.

Example 16 This example tests one water component, one heavy component and one light component. SAGD process with 15106 well pairs (30212 wells, 15106 injectors and 15106 producers) is simulated. The grid has a dimension of $60 \times 4400 \times 85$ and size of $20ft \times 10ft \times 4ft$. All wells are horizontal wells along x direction. All injection wells operate at 5 bbl/day water injection, with a steam quality of 0.2 and temperature of 450F. All production wells operate at fixed bottom hole pressure of 300 psi. All wells are modelled by implicit method. The model file has around 377,000 lines. Their properties are the same as Example 2. The simulation time is 100 time steps due to system running time limit. The initial time step is $1e-6$ days.

Preconditioner	Decoupling	Time steps	# Newton	# Linear solver
CPR-FP	NONE	NA	NA	NA
CPR-FP	FRS	NA	NA	NA
CPR-FP	DRS	NA	NA	NA
CPR-FP	ABF	NA	NA	NA
CPR-FP	GJE	133 (17)	588	8625
CPR-FP	DRS+ABF	NA	NA	NA
CPR-FP	DRS+GJE	141 (15)	771	17780
CPR-FP	FRS+ABF	NA	NA	NA
CPR-FP	FRS+GJE	137 (15)	750	17656
CPR-PF	NONE	NA	NA	NA
CPR-PF	FRS	NA	NA	NA
CPR-PF	DRS	NA	NA	NA
CPR-PF	ABF	NA	NA	NA
CPR-PF	GJE	153 (10)	729	20324
CPR-PF	DRS+ABF	NA	NA	NA
CPR-PF	DRS+GJE	158 (14)	780	22515
CPR-PF	FRS+ABF	NA	NA	NA
CPR-PF	FRS+GJE	144(10)	593	3380
CPR-FPF	NONE	NA	NA	NA
CPR-FPF	FRS	NA	NA	NA
CPR-FPF	DRS	NA	NA	NA
CPR-FPF	ABF	NA	NA	NA
CPR-FPF	GJE	145 (17)	805	18441
CPR-FPF	DRS+ABF	NA	NA	NA
CPR-FPF	DRS+GJE	NA	NA	NA
CPR-FPF	FRS+ABF	NA	NA	NA
CPR-FPF	FRS+GJE	142 (15)	803	18461

Table 13: Numerical summary of Example 14

Preconditioner	Decoupling	Time steps	# Newton	# Linear solver
CPR-FP	GJE	100	284	1245
CPR-FP	FRS+GJE	100	267	1194
CPR-PF	GJE	100	299	1540
CPR-PF	FRS+GJE	100	282	1183
CPR-FPF	GJE	100	308	1801
CPR-FPF	FRS+GJE	100	298	1255

Table 14: Numerical summary of Example 15

20 nodes and 400 CPU cores (400 MPIs) are employed on Niagara, Compute Canada. The Newton tolerance is $1e-3$ and its maximal iterations are 15. The linear solver is BICGSTAB, its tolerance is also $1e-3$ and its maximal iterations are 100. The maximal changes in a time step for pressure, saturation, molar fraction and temperature are 500 psi, 0.1, 0.1 and 15 F.

Table 15 shows the numerical summary for SAGD simulation with 15106 well pairs. All tests pass except one (CPR-FPF + GJE) due to an internal error. Again, the table shows that the Newton method and linear solver are efficient. The FRS+GJE decoupling method works much better than the GJE decoupling method.

4.4 Scalability

The parallel computers from Compute Canada are employed. The Niagara supercomputer consists of 1500 nodes, and each node has 40 Intel Skylake cores at 2.4GHz, for a total of 60,000 cores. Each node has 202 GB (188 GiB) RAM, and EDR Infiniband network is used to communicate. The Cedar supercomputer has a hybrid architecture, which uses Intel E5-2683 v4 "Broadwell" at 2.1Ghz, E5-2650 v4 at 2.2GHz, Intel E7-4809 v4 "Broadwell" at 2.1Ghz, and Intel Platinum 8160F "Skylake"

Preconditioner	Decoupling	Time steps	# Newton	# Linear solver
CPR-FP	GJE	100	334	1954
CPR-FP	FRS+GJE	100	291	897
CPR-PF	GJE	100	310	1389
CPR-PF	FRS+GJE	100	293	1195
CPR-FPF	GJE	97 (failed)	279	1439
CPR-FPF	FRS+GJE	100	269	571

Table 15: Numerical summary of Example 16

at 2.1Ghz. It has a total of 58,416 CPU cores for computation, and 584 GPU devices.

Example 17 This example studies a large thermal model with a grid dimension of $360 \times 400 \times 1600$, 230 million grid blocks. 12 nodes are employed using the Niagara supercomputer, and up to 192 CPU cores are used. The Newton method is applied with a tolerance of $1e-6$ and maximal iterations of 10. The linear solver is BICGSTAB with a tolerance of $1e-5$ and maximal iterations of 100. The preconditioner is the CPR-FPF method. Table 16 presents running time and memory used. Figure 95 shows the scalability.

Table 16 shows that huge amount of memory is required, which is not possible for desktop computers. The running time and Figure 95 show the simulator, linear solver and preconditioner have good scalability. The solver and preconditioner can solve linear systems with billions of unknowns.

CPU cores	Total time (s)	Solver time (s)	Overall speedup	Memory (GB)
24	2448.78	927.92	1.00 (100%)	1,945.92
48	1094.55	380.40	2.24 (112%)	1,959.28
96	545.20	194.81	4.49 (112%)	1,970.83
192	291.88	107.32	8.38 (105%)	1,994.25

Table 16: Summary of Example 17

Example 18 This example studies a large thermal model with a grid dimension of $360 \times 2000 \times 1600$, 1.2 billion grid blocks. 120 nodes are employed using the Cedar supercomputer, and up to 960 CPU cores are used. The Newton method is applied with a tolerance of $1e-10$ and maximal iterations of 10. The linear system has 6 billion unknowns, and the linear solver BICGSTAB is applied, which uses a tolerance of $1e-10$ and maximal iterations of 100. The preconditioner is the CPR-FPF method. Table 17 presents running time and memory used. Figure 96 shows the scalability.

Table 17 and Figure 96 show the simulator, linear solver and preconditioner have excellent scalability. The simulator can handle large-scale models, and the linear solver and preconditioner can solve linear systems with billions of unknowns.

CPU cores	Total time (s)	Solver time (s)	Overall speedup	Memory (GB)
240	1802.24	934.92	1.00 (100%)	9,839
480	897.69	455.47	2.00 (100%)	9,906
960	474.29	227.89	3.80 (95.0%)	9,996

Table 17: Summary of Example 18

Example 19 This example studies a large thermal model with a grid dimension of $1080 \times 2000 \times 1600$, 3.46 billion grid blocks and the resulted linear systems have 17.3 billion unknowns. 360 nodes are employed using the Cedar supercomputer. The Newton method is applied with a tolerance of $1e-10$ and maximal iterations of 10. The linear solver is BICGSTAB with a tolerance of $1e-10$ and maximal iterations of 100. The preconditioner is the CPR-FPF method with GJE decoupling. Table 18 presents running time and memory used.

Table 18 show the simulator, linear solver and preconditioner have excellent scalability. This example proves that our thermal simulator can handle extreme large-scale models. If more computing resource is available, larger model can be

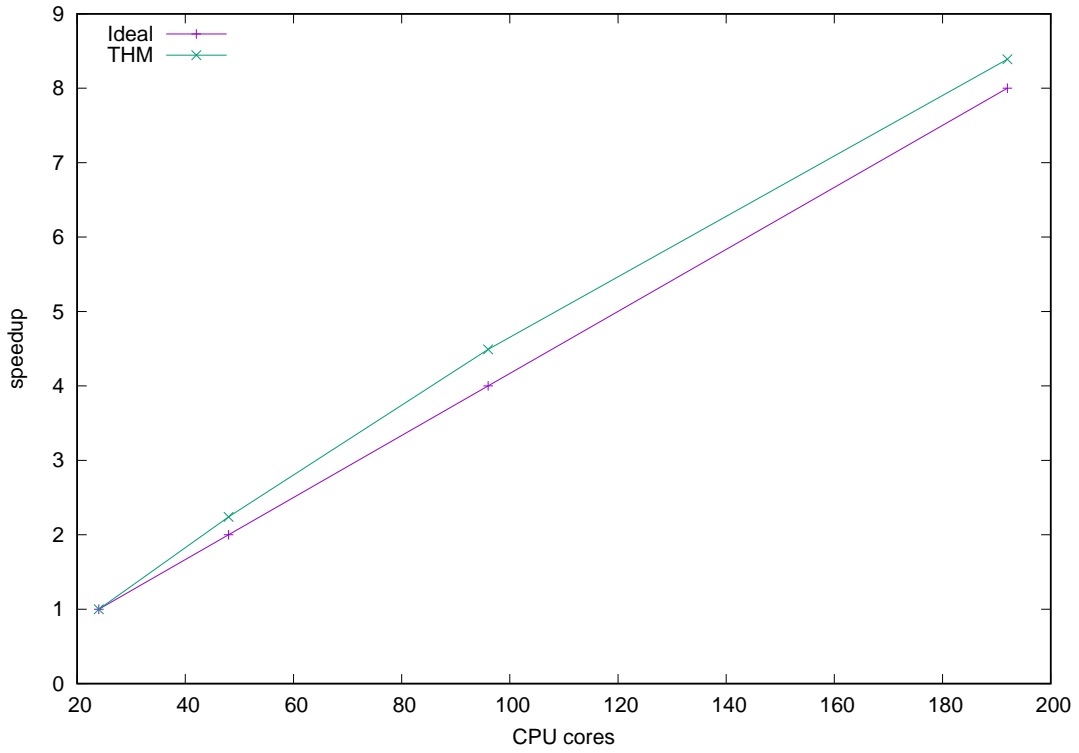


Figure 95: Example 17: scalability curve

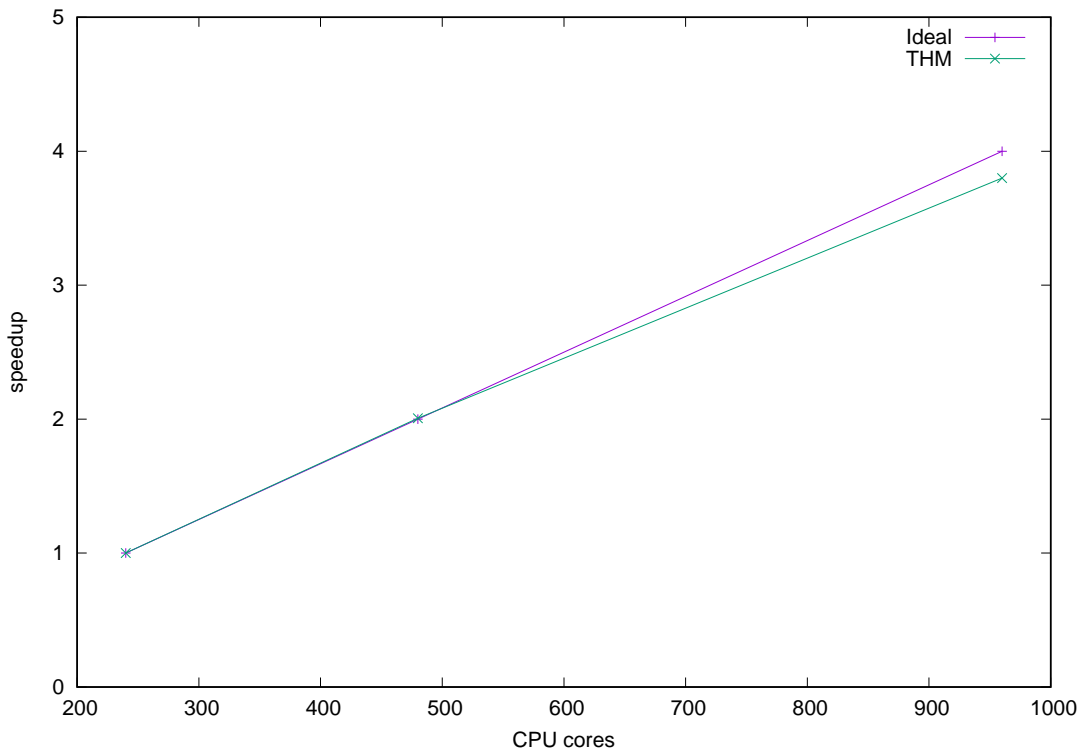


Figure 96: Example 18: scalability curve

simulated. Our linear solver and preconditioner can solve linear systems with dozens of billions of unknowns. In ideal case, when the size of MPIs doubles, the simulation time should be cut by half and the ideal speedup should be 2. This example shows a speedup of 1.65 and an efficiency of 82.5%, and we believe the reason is that when more CPU cores are used in one node, these processors compete memory and computing, which reduces the effective memory communication bandwidth. Therefore, the speedup is reduced.

CPU cores	Total time (s)	Solver time (s)	Overall speedup	Memory (GB)
2880 (360 X 8)	1247.74	996.76	1.00 (100%)	30,101.46
5760 (360 X 16)	757.70	578.32	1.65 (82.5%)	33,490.12

Table 18: Summary of Example 19

4.5 Scalability on Another Supercomputer

A Cray XC30 supercomputer deployed is employed. Each computation node contains two 2.7 GHz, 12-core Intel E5-2697 v2 CPUs, and 64 GB of memory is shared between the two processors. The memory bandwidth is around 103 Gb/s. The memory access is non-uniform access (NUMA): each processor owns a single NUMA region of 32 GB. Accessing its own region has a lower latency than accessing the other NUMA region. Also, these 24 cores compete the memory channels. The Aries interconnect connects all computation nodes in a Dragonfly topology.

Example 20 This example studies a large thermal model with a grid dimension of $1440 \times 2000 \times 1600$, 4.6 billion grid blocks and the resulted linear systems have 23 billion unknowns. 1024 nodes are employed. The Newton method is applied with a tolerance of $1e-4$ and maximal iterations of 10. The linear solver is BICGSTAB with a tolerance of $1e-3$ and maximal iterations of 100. The preconditioner is the CPR-FPF method with GJE decoupling. Table 19 presents running time and memory used and Figure 97 shows the scalability.

Table 19 shows overall time, linear solver time, linear solver speedup, overall speedup and total memory. When 4096 and 6144 cores are used, the scalabilities are 1.89 and 2.7, respectively, while the best scalabilities should be 2 and 3. In this case, the parallel efficiencies are 94% and 90%, which are good for parallel numerical simulations. However, this example shows linear solver has better speedup and parallel efficiency. If special optimization techniques are applied, such as multi-level load balancing that consider the architecture of the system and multi-layer communications, the communication volume and latency will be reduced and scalability can be improved. When 12288 cores are employed, each node run 12 cores and 12 MPIs, and each processor uses its 6 cores. In this case, memory access may be an important issue, which may reduce the effective memory bandwidth of each MPI and increase computation time.

CPU cores	Total time (s)	Solver time (s)	Solver speedup	Overall speedup	Memory (GB)
2048	793.68	594.70	1.00 (100%)	1.00 (100%)	43,090.70
4096	419.45	305.93	1.94 (97.0%)	1.89 (94%)	41,542.27
6144	293.85	213.48	2.78 (92.7%)	2.70 (90%)	45,118.68
12288	168.97	118.23	5.03 (83.0%)	4.70 (78%)	44,063.20

Table 19: Summary of Example 20

Example 21 This example studies a large thermal model with a grid dimension of 9.2 billion grid blocks and the resulted linear systems have 46 billion unknowns. 2048 nodes are employed. The Newton method is applied with a tolerance of $1e-4$ and maximal iterations of 10. The linear solver is BICGSTAB with a tolerance of $1e-3$ and maximal iterations of 100. The preconditioner is the CPR-FPF method with GJE decoupling. Table 20 presents running time and memory used, and Figure 98 shows the scalability (overall speedup) curve.

Example 22 This example studies a large thermal model with a grid dimension of 20 billion grid blocks using 4096 nodes and the resulted linear systems have 100 billion unknowns. The Newton method is applied with a tolerance of $1e-4$ and maximal iterations of 10. The linear solver is BICGSTAB with a tolerance of $1e-3$ and maximal iterations of 100. The preconditioner is the CPR-FPF method with GJE decoupling. Table 21 presents running time and memory used, and Figure 99 is the scalability.

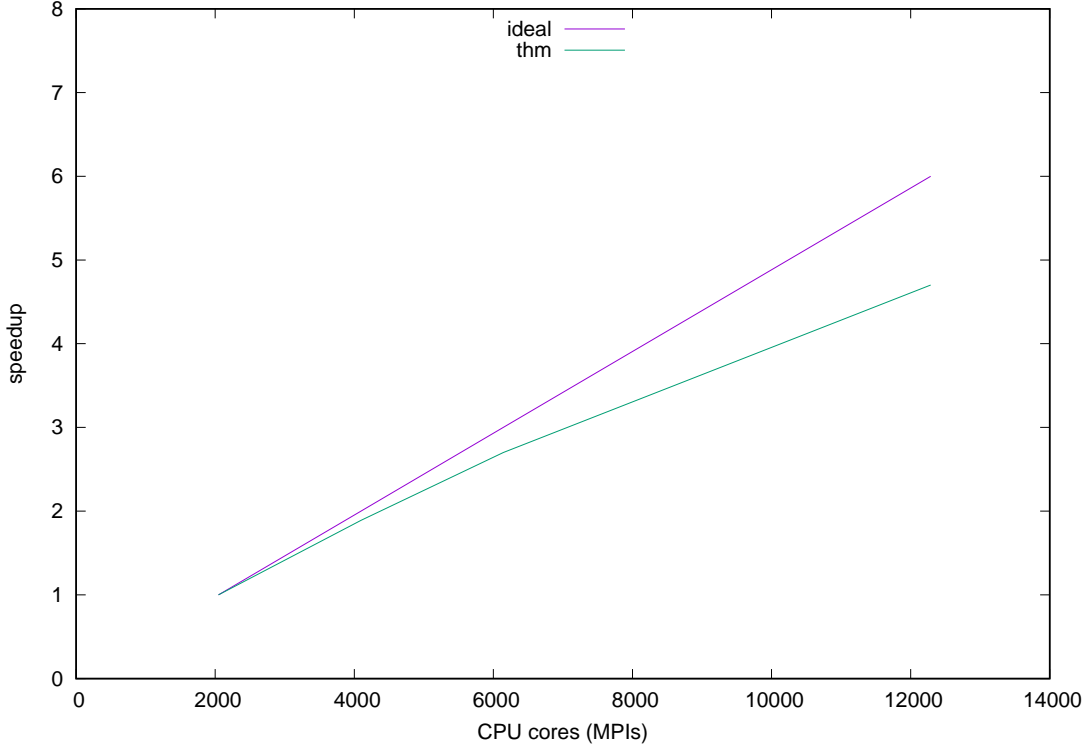


Figure 97: Example 20: scalability curve

CPU cores	Total time (s)	Solver time (s)	Solver speedup	Overall speedup	Memory (GB)
4096	804.68	600.54	1.00 (100%)	1.00 (100%)	83,970.30
8192	434.8	314.37	1.91 (95.5%)	1.85 (92.5%)	86,522.03
12288	300.83	216.14	2.77 (92.0%)	2.67 (89.0%)	92,951.34
24576	174.59	118.70	5.05 (84.2%)	4.60 (76.66%)	90,880.31

Table 20: Summary of Example 21

CPU cores	Total time (s)	Solver time (s)	Solver speedup	Overall speedup	Memory (GB)
8192	886.10	656.64	1.00 (100%)	1.00 (100%)	182,530.13
16384	476.95	341.02	1.92 (96.0%)	1.85 (92.5%)	184,450.12
24576	332.46	236.71	2.77 (92.3%)	2.66 (88.6%)	206,267.72

Table 21: Summary of Example 22

Example 21 and Example 22 show similar results. The overall scalability is good but the linear solver has better scalability. The memory consumption is proportional to grid blocks, which means if more computation resource is available, larger models can be studied. Since the thermal reservoir simulator has good scalability, the same model can be run faster if using more computation nodes. These examples indicate that our thermal simulator can handle giant thermal models. Meantime, we have observed that when more cores of a processor are employed, the scalability tends to reduce, which could be caused by memory bandwidth, network or algorithms, and there is room to investigate and to improve its performance.

4.6 Scalability of Simplified Models

In standard thermal simulations, various properties should be stored, such as porosity, density of each phase, viscosity, enthalpy, internal energy, saturations, temperature, and molar fractions. The memory consumption is huge, which makes hard to benchmark larger models unless a larger supercomputer is available, such as Summit from Oak Ridge National Laboratory and Blue Waters from the National Center for Supercomputing Applications (NCSA) at the University of Illinois

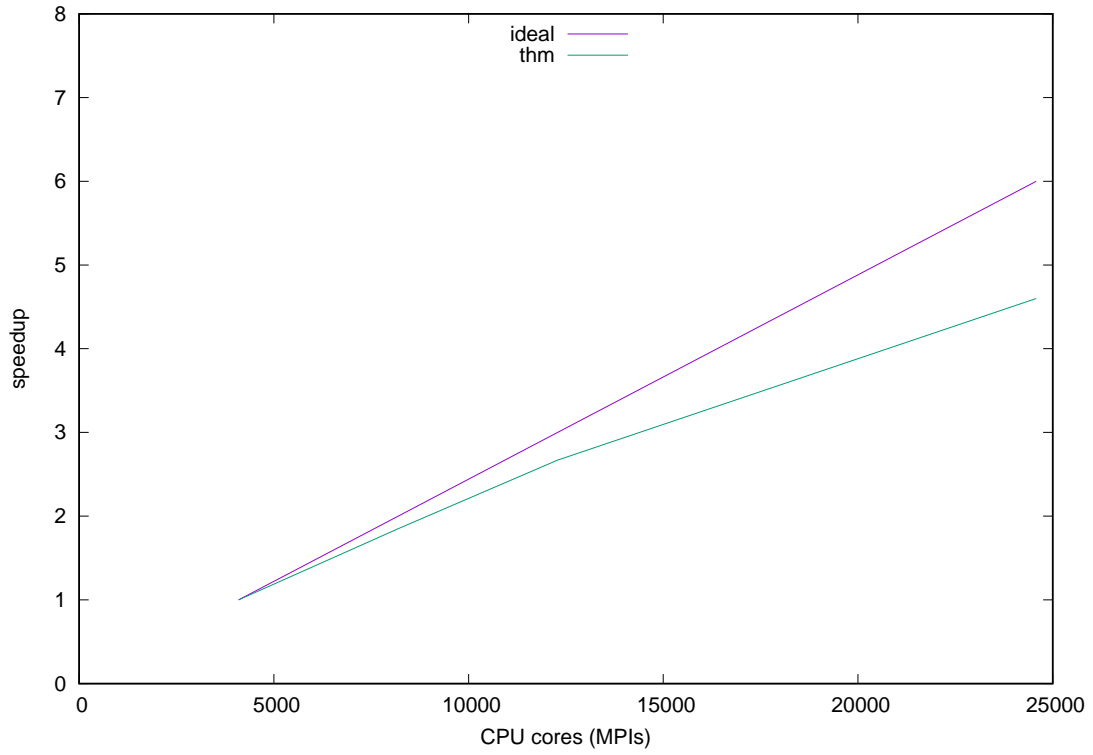


Figure 98: Example 21: scalability curve

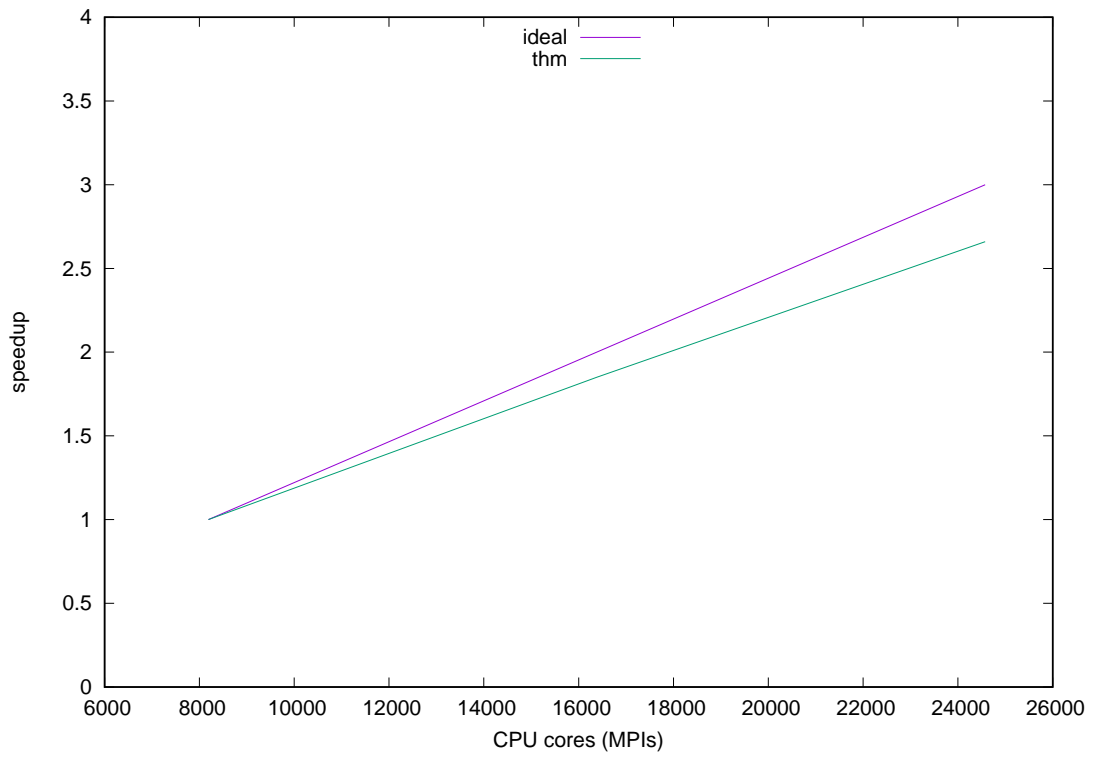


Figure 99: Example 22: scalability curve

at Urbana-Champaign. Here simplified models are designed to benchmark model with more grid blocks. However, grid generation, grid load balancing, data management, distributed matrix and vector, linear solver and preconditioner are all tested. All simulated problems are run on the Cray XC30 supercomputer.

Example 23 This example studies a simplified problem with a grid dimension of 42.8 billion grid blocks and 1024 nodes are employed. The linear solver is BICGSTAB and the preconditioner is the RAS method. The RAS method has good scalability, since the communications are local, and only one matrix is required, which is not the case as for AMG solver, which may have many coarser matrices. Table 22 presents running time and memory used.

CPU cores	Total time (s)	Solver time (s)	Solver speedup	Overall speedup	Memory (GB)
1024	744.31	381.40	1.00 (100%)	1.00 (100%)	47,869.86
2048	364.30	183.82	2.07 (103.5%)	2.04 (102%)	48,792.74
3072	264.48	137.74	2.76 (92.0%)	2.81 (93.7)	49,591.08
6144	131.82	68.92	5.53 (92.2%)	5.64 (94.0%)	53,875.08
12288	72.61	37.95	10.05 (83.8%)	10.25 (85.0%)	55,398.00
24576	41.65	23.72	16.07 (67.0%)	17.87 (74.0%)	56,178.96

Table 22: Summary of Example 23

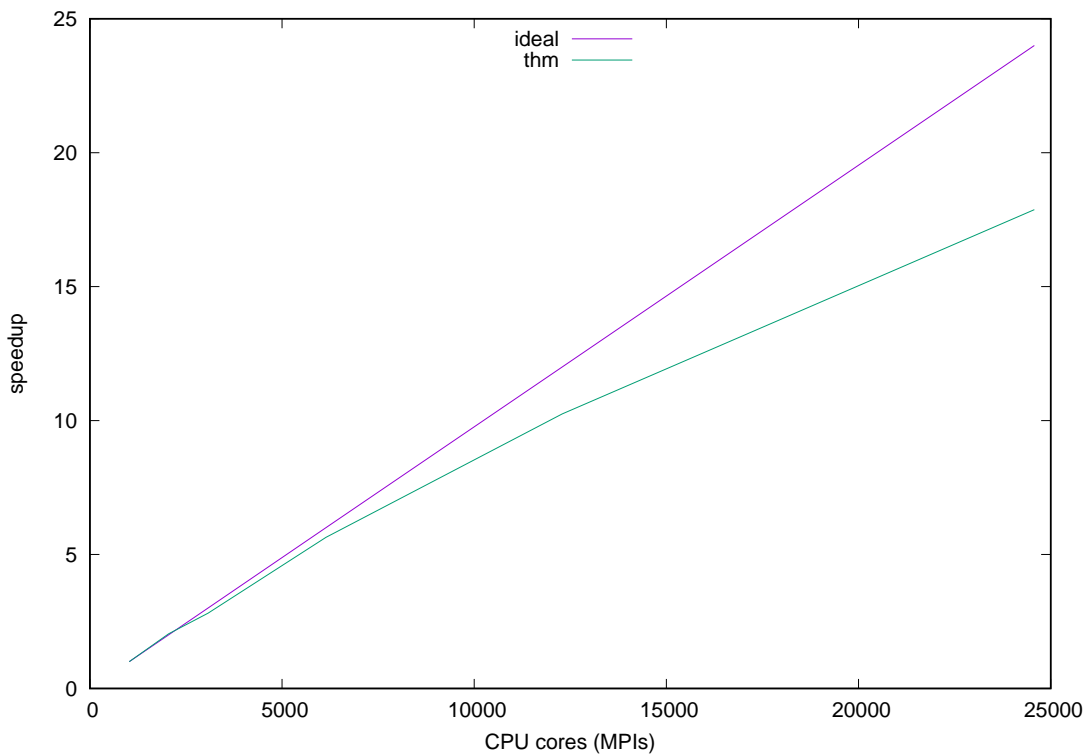


Figure 100: Example 23: scalability curve

Example 24 This example studies a simplified problem with a grid dimension of 216 billion grid blocks and 4096 nodes are employed. The linear solver is BICGSTAB and the preconditioner is the RAS method. Table 23 presents running time and memory used.

CPU cores	Total time (s)	Solver time (s)	Solver speedup	Overall speedup	Memory (GB)
8192	472.64	240.15	1.00 (100%)	1.00 (100%)	252,194.32
16384	249.68	130.52	1.84 (92.0%)	1.89 (94.5%)	255,154.24
24576	169.84	88.58	2.71 (90.4%)	2.78 (92.7%)	258,981.60
49152	96.53	51.97	4.62 (77.0%)	4.89 (81.5%)	269,806.56
98304	55.77	31.89	7.53 (62.8%)	8.47 (70.6%)	289,981.44

Table 23: Summary of Example 24

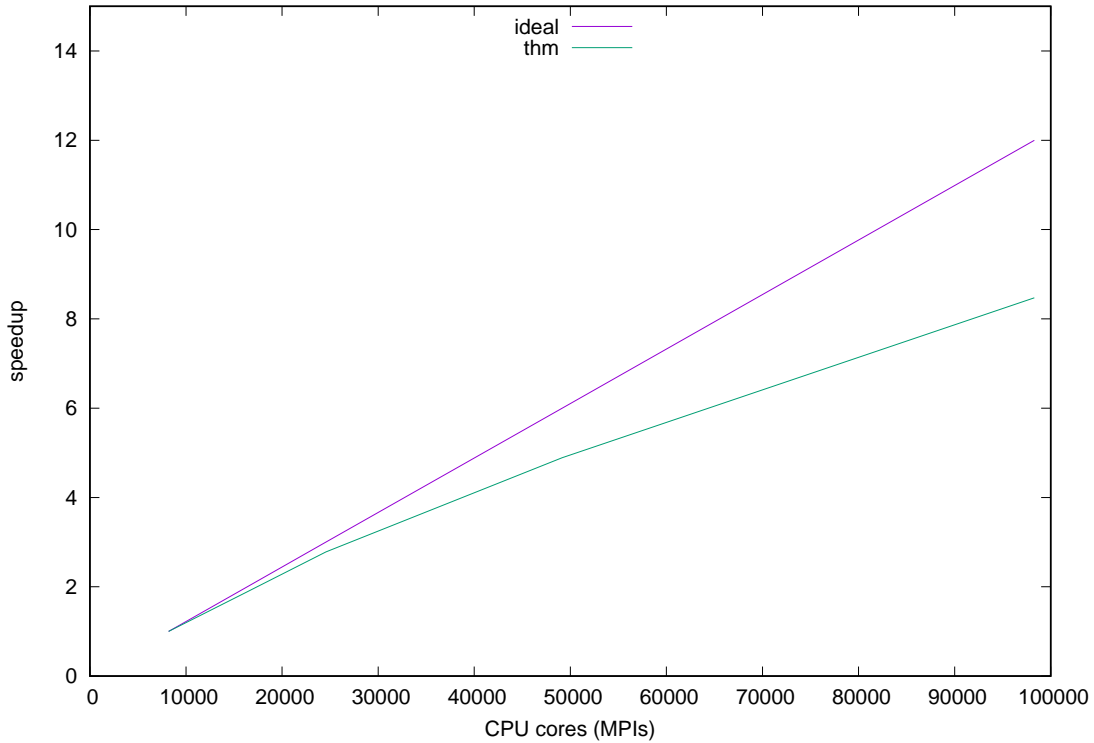


Figure 101: Example 24: scalability curve

5 Conclusions

This paper introduces a parallel thermal simulator on distributed-memory parallel computers, where MPI is employed for communications. The simulator is designed to handle giant models with billions even trillions of grid blocks using hundreds of thousands of CPU cores. Its mathematical models and numerical methods are presented. Numerical experiments are carried out to verify the methods and implementations, which show that our simulator can match commercial software and it has excellent scalability, and it can handle extremely large-scale reservoir models.

Acknowledgements

The support of Department of Chemical and Petroleum Engineering, University of Calgary and Reservoir Simulation Research Group is gratefully acknowledged. The research is partly supported by NSERC/AIEES/Foundation CMG, AITF iCore, IBM Thomas J. Watson Research Center, and the Frank and Sarah Meyer FCMG Collaboration Centre for Visualization and Simulation. The research is also enabled in part by support provided by WestGrid (www.westgrid.ca), SciNet (www.scinethpc.ca) and Compute Canada Calcul Canada (www.computeCanada.ca).

References

- [1] Ruijian He, Bo Yang, Hui Liu, Zhangxin Chen, A New In-Situ Combustion Simulator for Parallel Computers, arXiv: 1811.11992, 2018.
- [2] Peaceman, D. W. Interpretation of well-block pressures in numerical reservoir simulation. *Society of Petroleum Engineers Journal*, 18(03):183–194, 1978.
- [3] T. Al-Shaalan, H. Klie, A. Dogru, and M. Wheeler. Studies of robust two stage preconditioners for the solution of fully implicit multiphase flow problems. In *SPE Reservoir Simulation Symposium. 2009*.
- [4] Tareq Al-Shaalan, Larry S K Fung, and Ali H Dogru. A Scalable Massively Parallel Dual-Porosity Dual-Permeability Simulator for Fractured Reservoirs with Super-K Permeability. In *SPE Annual Technical Conference and Exhibition, 5-8 October, Denver, Colorado, 2003*.
- [5] J Barua and R N Horne. Improving the Performance of Parallel (and Serial) Reservoir Simulators. In *SPE Symposium on Reservoir Simulation, 6-8 February, Houston, Texas, 1989*.
- [6] H. Cao, T. Schlumberger, A. Hamdi, J. Wallis, and H. Yardumian. Parallel scalable unstructured cpr-type linear solver for reservoir simulation. In *SPE Annual Technical Conference and Exhibition. 2005*.
- [7] Mark C H Chien, Hamdi A Tchelepi, Hrant E Yardumian, and Wen H Chen. A Scalable Parallel Multi-Purpose Reservoir Simulator. In *SPE Reservoir Simulation Symposium, 8-11 June, Dallas, Texas, pages 17–30, 1997*.
- [8] K H Coats. In-Situ Combustion Model. *SPE Society of Petroleum Engineers of AIME*, 20:533–554, 1980.
- [9] K H Coats. Reservoir Simulation. In *Petroleum Engineering Handbook*, chapter 48, pages 20–48. 1987.
- [10] Dim Coumou, Stephan Matthäi, Sebastian Geiger, and Thomas Driesner. A parallel FE-FV scheme to solve fluid flow in complex geologic media. *Computers and Geosciences*, 34:1697–1707, 2008.
- [11] R B Crookston, W E Culham, and Wen H Chen. A Numerical Simulation Model for Thermal Recovery Processes. *Society of Petroleum Engineers Journal*, 19:37–58, 1979.
- [12] Ali H Dogru. Megacell Reservoir Simulation. *Journal of Petroleum Technology*, 52, 2000.
- [13] Ali H Dogru, K G Li, H.a. Sunaidi, W.a. Habiballah, Larry S K Fung, N Al-Zamil, D Shin, A E McDonald, and N K Srivastava. A Massively Parallel Reservoir Simulator for Large Scale Reservoir Simulation. In *SPE Reservoir Simulation Symposium, 14-17 February, Houston, Texas, 1999*.
- [14] Ali H Dogru, H A Sunaidi, Larry S K Fung, Walid A Habiballah, Nabil Al-Zamel, and K G Li. A Parallel Reservoir Simulator for Large-Scale Reservoir Simulation. *SPE Reservoir Evaluation & Engineering*, 5:11–23, 2002.
- [15] David a Edwards, Dayal Gunasekera, Jonathan Morris, Gareth Shaw, Kevin Shaw, Paul a Fjerstad, Jitendra Kikani, Jessica Franco, Viet Hoang, and Lisette Quettier. Reservoir Simulation : Keeping Pace with Oilfield Complexity. *Oilfield Review*, 23:4–15, 2012.
- [16] C. Feng, S. Shu, J. Xu, and C. Zhang. A multi-stage preconditioner for the black oil model and its openmp implementation. In *21st International Conference on Domain Decomposition Methods, 2012, France*.
- [17] Larry S K Fung and Ali H Dogru. Efficient multilevel method for local grid refinement for massively parallel reservoir simulation. In *ECMOR VII - 7th European Conference on the Mathematics of Oil Recovery, 2000*.
- [18] Janusz W Grabowski, Paul K Vinsome, Ran C Lin, Alda Behie, and Barry Rubin. A Fully Implicit General Purpose Finite-Difference Thermal Model For In Situ Combustion And Steam. In *SPE Annual Technical Conference and Exhibition, 23-26 September, Las Vegas, Nevada, 1979*.
- [19] X. Hu, W. Liu, G. Qin, J. Xu, and Z. Zhang. Development of a fast auxiliary subspace pre-conditioner for numerical reservoir simulators. In *SPE Reservoir Characterisation and Simulation Conference and Exhibition. 2011*.

- [20] John E Killough. Is Parallel Computing Ready for Reservoir Simulation ? A Critical Analysis of the State of the Art. In *SPE Annual Technical Conference and Exhibition, 3-6 October, Houston, Texas, 1993*.
- [21] H. Liu, K. Wang, and Z. Chen. A family of constrained pressure residual preconditioners for parallel reservoir simulations. *Numerical Linear Algebra with Applications*, 23:120–146, 2016.
- [22] Hui Liu, Kun Wang, Zhangxin Chen, Kirk E. Jordan, Jia Luo, and Hui Deng. A parallel framewrok for reservoir simulators on distributed-memory supercomputers. In *SPE-176045-MS, SPE/IATMI Asia Pacific Oil & Gas Conference and Exhibition, Nusa Dua, Indonesia, 20–22 October, 2015*.
- [23] J A Meijerink, D T Van Daalen, P J Hoogerbrugge, and R J A Zeestraten. Towards a More Effective Parallel Reservoir Simulator. In *SPE Symposium on Reservoir Simulation, 17-20 February, Anaheim, California, 1991*.
- [24] R T Mifflin, J W Watts, and A Weiser. A Fully Coupled, Fully Implicit Reservoir Simulator for Thermal and Other Complex Reservoir Processes. In *SPE Symposium on Reservoir Simulation, 17-20 February, Anaheim, California, 1991*.
- [25] Manish Parashar, John Wheeler, Gary Pope, Kefei Wang, and Peng Wang. A New Generation EOS Compositional Reservoir Simulator: Part II - Framework and Multiprocessing. In *SPE Reservoir Simulation Symposium, 8-11 June, Dallas, Texas, 1997*.
- [26] Barry Rubin and W Buchanan. A General Purpose Thermal Model. *Society of Petroleum Engineers Journal*, 25, 1985.
- [27] Sophie Verdiere, Lisette Quettier, Pierre Samier, and Alan Thompson. Applications of a parallel simulator to industrial test cases. In *SPE Reservoir Simulation Symposium, 14-17 February, Houston, Texas, 1999*.
- [28] J. Wallis, R. Kendall, and T. Little. Constrained residual acceleration of conjugate residual methods. In *SPE Reservoir Simulation Symposium, 1985*.
- [29] Baohua Wang, Shuhong Wu, Qiaoyun Li, Xiaobo Li, Hua Li, Chensong Zhang, and Jinchao Xu. A multilevel preconditioner and its shared memory implementation for new generation reservoir simulator. In *SPE-172988-MS, SPE Large Scale Computing and Big Data Challenges in Reservoir Simulation Conference and Exhibition, 15-17 September, Istanbul, Turkey, 2014*.
- [30] K. Wang, L. Zhang, and Z. Chen. Development of discontinuous galerkin methods and a parallel simulator for reservoir simulation. In *SPE-176168-MS, SPE/IATMI Asia Pacific Oil & Gas Conference and Exhibition, 20-22 October, 2015, Nusa Dua, Bali, Indonesia, 2015*.
- [31] Kun Wang, Hui Liu, and Zhangxin Chen. A scalable parallel black oil simulator on distributed memory parallel computers. *Journal of Computational Physics*, 301:19–34, 2015.
- [32] Kun Wang, Hui Liu, Jia Luo, and Zhangxin Chen. Parallel simulation of full-field polymer flooding. In *The 2nd IEEE International Conference on High Performance and Smart Computing (IEEE HPSC 2016)*.
- [33] Kun Wang, Hui Liu, Jia Luo, and Zhangxin Chen. A multi-continuum multi-phase parallel simulator for large-scale conventional and unconventional reservoirs. *Journal of Natural Gas Science and Engineering*, 33:483–496, 2016.
- [34] Peng Wang, S Balay, K Sepehrnoori, J Wheeler, J Abate, B Smith, and G A Pope. A Fully Implicit Parallel EOS Compositional Simulator for Large Scale Reservoir Simulation. In *SPE Reservoir Simulation Symposium, 14-17 February, Houston, Texas, 1999*.
- [35] Peng Wang, I Yotov, M Wheeler, T Arbogast, C Dawson, M Parashar, and K Sepehrnoori. A New Generation EOS Compositional Reservoir Simulator: Part I - Formulation and Discretization. In *SPE Reservoir Simulation Symposium, 8-11 June, Dallas, Texas, 1997*.
- [36] Yu-shu Wu, Keni Zhang, Chris Ding, Karsten Pruess, Erik Elmroth, and G S Bodvarsson. An efficient parallel-computing method for modeling nonisothermal multiphase flow and multicomponent transport in porous and fractured media. *Advances in Water Resources*, 25:243–261, 2002.
- [37] L. Zhang. A parallel algorithm for adaptive local refinement of tetrahedral meshes using bisection. *Numer. Math.*, 2:65–89, 2009.

- [38] L. Zhang, T. Cui, and H. Liu. A set of symmetric quadrature rules on triangles and tetrahedra. *J. Comput. Math*, pages 89–96, 2009.
- [39] Chen, Z. *Reservoir Simulation: Mathematical Techniques in Oil Recovery*. CBMS-NSF Regional Conference Series in Applied Mathematics. SIAM, 2007.
- [40] CMG. *STARS User’s Guide*. Computer Modelling Group Ltd., 2015.
- [41] Stone, H. L. Estimation of three-phase relative permeability and residual oil data. *Journal of Canadian Petroleum Technology*, 12(4), 1973.
- [42] Delshad, M. and Pope, G. A. Comparison of the three-phase oil relative permeability models. *Transport in Porous Media*, 4(1):59–83, 1989.
- [43] Stone, H. L. Probability model for estimating three-phase relative permeability. *Journal of Petroleum Technology*, 22(02):214–218, 1970.
- [44] Naar, J. and Wygal, R. J. Three-phase imbibition relative permeability. *Society of Petroleum Engineers Journal*, 1(04):254–258, 1961.
- [45] Corey, A. T., Rathjens, C. H., Henderson, J. H., and Wyllie, M. R. J. Three-phase relative permeability. *Journal of Petroleum Technology*, 8(11):63–65, 1956.
- [46] Coats, K. H. In-situ combustion model. *Society of Petroleum Engineers Journal*, 20(06):533–554, 1980.
- [47] Clapeyron, E. Memoir sur la puissance motrice de la chaleur. *Journal de l’cole Royale Polytechnique*, pages 153–190, 1834.
- [48] Redlich, O. and Kwong, J. N. On the thermodynamics of solutions. v. an equation of state. fugacities of gaseous solutions. *Chemical reviews*, 44(1):233–244, 1949.
- [49] Oklany, J. S. F. *An In-situ Combustion Simulator for Enhanced Oil Recovery*. PhD thesis, University of Salford, 1992.
- [50] Abou-Kassem, J. H. and Aziz, K. Handling of phase change in thermal simulators. *Journal of petroleum technology*, 37(09):1661–1663, 1985.
- [51] Crookston, R. B., Culham, W. E., and Chen, W. H. A numerical simulation model for thermal recovery processes. *Society of Petroleum Engineers Journal*, 19(01):37–58, 1979.
- [52] Coats, K. H. Simulation of steamflooding with distillation and solution gas. *Society of Petroleum Engineers Journal*, 16(05):235–247, 1976.
- [53] Hui Liu, Zhangxin Chen, Scalable linear solvers for sparse linear systems from large-scale numerical simulations, arXiv: 1701.05913, 2016.
- [54] Hui Liu, Kun Wang, Bo Yang, Zhangxin Chen, Development of A Platform for Large-scale Reservoir Simulations on Parallel computers, arXiv:1602.05901, 2016.
- [55] Soave, G. Equilibrium constants from a modified redlich-kwong equation of state. *Chemical Engineering Science*, 27(6):1197–1203, 1972.
- [56] Peng, D. Y. and Robinson, D. B. A new two-constant equation of state. *Industrial & Engineering Chemistry Fundamentals*, 15(1):59–64, 1976.
- [57] Xia Bao, Zhangxing Chen, Hui Deng, Yizheng Wei, Hui Liu and Chao Dong, Geomechanical and Thermal Simulation of ES-SAGD Process , SPE-148847, Canadian Unconventional Resources Conference, Alberta, Canada, 15-17 November, 2011.
- [58] Van der Waals, J. D. The equation of state for gases and liquids. *Nobel lectures in Physics*, 1:254–265, 1910.

- [59] Vinsome, Paul K and Westerveld, Joop D, A SIMPLE METHOD FOR PREDICTING CAP AND BASE ROCK HEAT LOSSES IN THERMAL RESERVOIR SIMULATORS, *Journal of Canadian Petroleum Technology*, 19(03), 87–90, 1980.
- [60] S. Lacroix, Y. V. Vassilevski, M. F. Wheeler, Decoupling preconditioners in the implicit parallel accurate reservoir simulator (IPARS), *Numerical Linear Algebra with Applications* 8 (8) (2001) 537–549.
- [61] Jia Luo, Zhangxin Chen, Kun Wang, Hui Deng, Hui Liu, An Efficient and Parallel Scalable Geomechanics Simulator for Reservoir Simulation, SPE-176167-MS, SPE/IATMI Asia Pacific Oil & Gas Conference and Exhibition, Nusa
- [62] R. Bank, T. Chan, The alternate-block-factorization procedure for systems of partial differential equations, *BIT Numerical ...* 4 (29) (1989) 938–954.
- [63] Sebastian Gries, On the Convergence of System-AMG in Reservoir Simulation, SPE-182630-PA, *SPE Journal*, 23(2), 589 - 597, 2018.
- [64] Z. Chen, *Reservoir Simulation Mathematical Techniques in oil recovery*, Society for Industrial and Applied Mathematics, Philadelphia, PA, 2007.
- [65] TB Jonsthovel, TW Stone, Enhanced Discretization for Improved Stability of Thermal Simulation, SPE-183844-MS, SPE Middle East Oil & Gas Show and Conference, 6-9 March, Manama, Kingdom of Bahrain, 2017.
- [66] Chao Dong, An Integrated Multi-Component Reservoir-Wellbore Thermal Model, PhD Thesis, University of Calgary, 2012.
- [67] Chung-Kan Huang, Development of A General Thermal Oil Reservoir Simulator Under A Modularized Framework, PhD Thesis, University of Utah, 2009.